Title

Giant vesicles as cell-mimetic vessels: Induced cellular variation and confinement on a cyanobacterial circadian clock

Author

Li, Alexander Zhan Tu

Publication Date

2023

UNIVERSITY OF CALIFORNIA, MERCED

Giant vesicles as cell-mimetic vessels: Induced cellular variation and confinement on a cyanobacterial circadian clock

A dissertation submitted in partial satisfaction of the requirements
for the degree Doctor of Philosophy

in

Bioengineering

by

Alexander Zhan Tu Li

<u>Committee in charge:</u>

Professor Victor Muñoz, Chair

Professor Andy LiWang

Professor Joel Spencer

Professor Anand Bala Subramaniam

2023

The Dissertation of Alexander Zhan Tu Li is approved, and it is acceptable in quality and form for publication on microfilm and electronically:

Chair

University of California, Merced

2023

Table of Contents

Table of Figures

List of Tables

Funding and Contributions

Grants:

This work in this dissertation was made possible by funding from:

The National Science Foundation through NSF CAREER DMR-1848573, NSF CBET-1512686, NSF-CREST: Center for Cellular and Biomolecular Machines at UC Merced (NSF-HRD-1547848 and NSF-HRD-2112675).

The data in this work was collected, in part, with a confocal microscope acquired through the National Science Foundation MRI Award Number DMR-1625733.

Funding awards:

I would like to acknowledge funding awards that have supported me and my research throughout my doctoral studies from:

Graduate Dean's Dissertation Spring 2023

CCBM Fellowship: Fall 2019 & Spring 2022

Bioengineering Summer Fellowship 2019-2022

Carbon Neutrality Initiative Fellowship 2020

Global Food Initiative Fellowship/Ambassador 2018-2019

Acknowledgments

During the pursuit of my doctoral studies, I have gained much knowledge passed down by those whom I have had the honor to talk to, listen to, and share ideas with. Through this long, arduous, but fulfilling journey, I have come to learn much about critically evaluating arguments, discerning scientific reports and data, developing independent opinions, and what is needed to be able to tackle difficult tasks. But most of all, I have come to learn much about myself, my thoughts, and the processes needed to properly utilize them. There is also much I have gained in the ability to communicate both in scientific contexts and many other areas. This has never been as clear as it is now, as I look from the end of this journey, where I can now look forward in life with confidence. And throughout this journey, there have been many to whom I owe much to, that have been instrumental in this path to a PhD in many ways, especially when many times the path appeared to falter.

First, I would like to acknowledge Professor Anand Bala Subramaniam, my PhD advisor, for your guidance and mentorship from the very beginning of this journey. For the numerous talks and discussions that we have shared that have shaped my development during my studies here. And for all the time and dedication you have given, far beyond the realm of expectation, towards my development as a researcher. I know much of what I have gained as result of your efforts will continue to be of great benefit beyond my PhD.

I would then like to acknowledge my committee members, whom each have had a significant impact on my journey:

Professor Andy LiWang, thank you for the warm and open welcome you have always given me for your lab group. For the invitations to discussions in your lab meetings and connecting me with members of your lab group and others in the clocks field. For giving me the opportunity to learn and apply techniques for expressing and purifying clock proteins. It has given me both the context and excitement needed to continue on my path.

Professor Joel Spencer, thank you for your support and guidance when I was at one of my lowest points. It may not have appeared like it then, but it did have a profound impact and gave me the strength to continue on. I also want to thank you for all the friendly and enjoyable conversations we have had scattered throughout.

Professor Victor Muñoz, thank you for your unique and interesting questions, which have always kept me on my toes and pushed me to actively seek knowledge outside of the immediate boundaries of my research.

I would also like to give a big thanks to my fellow lab members: First my senior lab members, Joseph Pazzi and Melissa Xu, from whom I have learned so much during the time when I was least knowledgeable, and for the hospitality that you have given me. Your actions have helped shape my own mentorship methods and hospitality that I hope I have managed to pass on to the proceeding members that have joined the lab. I would like to thank Vaishnavi Girish, whom I have always enjoyed engaging with in discussions, arguments, bouncing ideas, and as a close friend in many courses. I also would like to thank the newer members of our lab. Alexis Cooper, thank you for being someone that has always brought the lab together, from organizing social activities to providing support to everyone in difficult times. Also, for being a continued source for slang that I can no longer keep track of. To the newest members of our lab, Vignesha Vijayananda and Nimra Khurram, I thank you for the wonderful friendship that we have developed and for all the fun times together. I am glad I had a chance to mentor both of you, and I will always be happy to answer any questions you have in the future.

I would also like to thank my collaborators from the LiWang lab, Joel Heisler and Supratim Dey, who have given me much guidance and mentorship on the expression and purification of clock proteins, and for all the knowledge they have shared with me.

I would like to also thank many of my close friends that have supported me throughout my journey. Adolfo thank you for supporting my start to this journey in the very beginning and for all the great times we have had together. TJ and Dylan, I am very happy we have stayed close friends even despite the distance. I enjoy the chances to hang out and spend time with you guys and I hope we will continue to do so. And to Kevin, Lyndi, Andy, and RJ, I am glad we still stay in touch and have the occasion chance to spend time together. I also would like to thank Dishanka, whom I have met only recently, but have had a lot of meaningful and interesting discussions in that time.

I would like to extend a heartfelt acknowledgment to my family: To my dad, my mom, my brother, Ben, and my grandma. I want to thank them for their support and understanding during my journey, despite my often-extended absences during this time. I hold them in my heart at all times, and their support has been an extremely important part of the journey.

Finally, I wish to show my deepest appreciation for my wife Vaishnavi Girish, whom I met during this long journey, and whom I am forever glad that she was by my side during this time. I have received an incredible amount of love and joy from someone I consider to be the most caring person I have ever known. Having you by my side is the single best thing that has happened to me in this journey, and you are undoubtedly the biggest influence that allowed me to get to where I am today.

Curriculum Vitae

Alexander Z.T. Li

Alexander.ztli@gmail.com

Education

University of California, Merced

- **PhD., Bioengineering** **Spring 2023**
    - **GPA:** 3.64
    - **Advisor:** Anand Subramaniam, Ph.D.

- **B.S., Mechanical Engineering** | ABET-accredited BSME Program **May 2016**
    - **University of Hong Kong** (Exchange) **Spring 2013**
    - **Tohoku University** (Research Exchange) **Spring 2012**

Presentations & Publications

Research Presentations

- **2023 Center for Circadian Biology (CCB)** **Poster Presentation**
- **2023 Biophysical Society: Annual Meeting** **Poster Presentation**
- **2021 American Chemical Society: National Meeting** **Oral Presentation**
- **2019 UC Bioengineering Symposium** **Oral Presentation**
- **2018 American Chemical Society: National Meeting** **Poster Presentation**

Publications

- **Li, A**; LiWang, A; Subramaniam, A.B. Intracellular variation and membrane binding hampers circadian clock fidelity: An approach using cell-mimetic giant vesicles. (Preparing for submission)

- Girish, V.; Pazzi, J.; **Li, A.**; Subramaniam, A. B. Fabrics of Diverse Chemistries Promote the Formation of Giant Vesicles from Phospholipids and Amphiphilic Block Copolymers. Langmuir 2019, 35, 9264–9273.

- **Li***, J. Pazzi*, M. Xu, A.B. Subramaniam. Cellulose abetted assembly and temporally-decoupled loading of cargo into vesicles synthesized from functionally diverse lamellar phase forming amphiphiles. Biomacromolecules 19, 849-859 (2018).

Honors & Awards

Graduate Dean's Dissertation Fellowship **Spring 2023**
Graduate Dissertation Fellowship

Center for Cellular and Biomolecular Machines **Fall 2019**
Graduate Research Fellowship **Spring 2022**

Carbon Neutrality Initiative **2020**
Project Fellowship

Global Food Initiative **2018 & 2019**
Ambassador & Project Fellowship

Merced Nanomaterials Center for Energy and Sensing **Summer 2016**
Undergraduate Research Fellowship

Capstone Innovation Design Clinic **Spring 2016**
1st place award engineering capstone design project.

Outreach

Confocal Microscopy High School Outreach Module **2017, 2018, & 2019**

Research & Teaching Experience

Graduate Student Researcher **May 2017 – 2023 (Present)**
UC Merced | Bioengineering

Teaching Assistant **Fall 2017 – Spring 2022**
UC Merced

- **Python for Bioengineers (BIOE 021)** **Fall 2017, 2018 & Spring 2022**
- **Calculus I (MATH 11)** **Spring 2020**
- **Heat Transfer (ENGR 135)** **Spring 2018**
- **Engineering Capstone Design (ENGR 190)** **Spring 2018**
- **Biotransport Phenomena (BIOE 104)** **Fall 2017**

Junior Specialist **August 2016 – May 2017**
UC Merced | Bioengineering

Abstract

Title: Giant vesicles as cell-mimetic vessels: Induced cellular variation and confinement on a cyanobacterial circadian clock

Dissertation Advisor: Anand Bala Subramaniam

Author: Alexander Zhan Tu Li

Degree: Bioengineering

University/Year: University of California, Merced. 2023

Committee Chair: Victor Muñoz

Giant unilamellar vesicles (GUVs) are spherical structures composed of an aqueous compartment enclosed by a bilayer membrane. They are often seen as a simplified analog of a cell membrane and can be utilized as minimal cell models for studying cellular systems due to their cell-like sizes and capacity to mediate membrane interactions. A paper-based diffusive loading technique termed, OSM-PAPYRUS, is shown to assemble GUVs in physiologically relevant salt solutions with gentle loading of proteins. Characterization of this loading process reveals cell-like variation of encapsulated protein concentrations and a gamma distribution often cited for protein distributions in the cell. This ability to mimic cellular variability in vitro reveals potential in bridging the gap between in vitro and in vivo experimentation. The highly controlled environment of in vitro experiments can be combined with cell-like volumes, phospholipid bilayer, and cellular variation in GUVs. A practical application is explored, encapsulating the post-translation oscillator (PTO) of the cyanobacteria circadian clock system which shows membrane interactions in vivo. The results showed that cellular variation and membrane binding significantly hampers the fidelity of the clock, in contrast to bulk experiments where concentration did not matter once a critical concentration is met. An increase in concentration to cellular levels helps counteract the effect of variation. Modeling the clock reaction using expected distributions and variation of encapsulated proteins, corroborated with the hypothesis that intercellular variation and membrane binding were responsible for trends in the experimental data. The experimental data and model showed that the PTO by itself was not capable of achieving the near 100% fidelity observed in the native cyanobacteria, instead, other cellular components, like SasA and CikA or transcriptional-translational feedback loop (TTFL) would be necessary to achieve in vivo clock fidelity. The GUV model demonstrated advantages over in vivo studies, particularly in the isolation of the PTO, which allowed for the determination that large period variations seen in vivo cannot be produced by the PTO even under cell-like variability and volumes. This demonstrates the ability of GUV in vitro models to obtain context on behaviors not appreciated by either previous bulk in vitro or in vivo studies.

Chapter 1: Introduction

1.1 Motivation and Overview

1.1.1 Giant unilamellar vesicles as minimal cell models

Vesicles are spherical structures that entrap an aqueous compartment enclosed by a bilayer membrane. They can be composed of a variety of amphiphilic molecules, including phospholipids (1–9), fatty acids (5, 10, 11), and polymers (5, 12–15). The membrane is typically semi-permeable, allowing water to pass through but preventing most macromolecules from escaping. Giant unilamellar vesicles (GUVs) are a class of vesicles that are defined as vesicles with diameters than are greater than 1 micrometer but cover a large range of diameters up to above 100 micrometers. GUVs in the lower size range can mimic the femto- to pico- liter volumes in biological cells, and combined with the presence of a phospholipid bilayer can begin to represent a simplified cell membrane. These properties allow the GUVs to be used as a minimal cell model for biophysical studies of cellular systems (16–18), for building synthetic cells (19–25), and potential as drug carriers (26–33). Hydrophilic molecules can be entrapped within the aqueous core while lipophilic molecules can be incorporated into the bilayer membrane, allowing for a high degree of flexibility in incorporating a wide range of molecules. The presence of a bilayer membrane also allows the study of proteins that interact with the membrane, such as for cell division machinery (34), and membrane and cytoskeletal proteins (35–38).

There are a variety of different methods that have been used to assemble GUVs. These methods can be broadly split into two categories, thin-film hydration methods (1–6, 8, 39–41) and droplet transfer methods (30, 42–50). Thin-film hydration methods typically involve drying amphiphiles into a thin film on a substrate, such as glass (39–41, 51), paper (1–6), fabrics (3), and gel (1, 8, 52), and then hydrating the film with an aqueous solution. The phospholipid then self-assembles into vesicular buds that remain attached to the hydrated lipid bilayers on the substrate, through nanotube-like tethers (5). One proposed model for the assembly of vesicles, termed, the budding and merging model, takes a thermodynamic approach in considering the change in free energy due to budding in relation to the elastic, adhesion, and edge energies of the lipid membrane on the surface (2). The authors report that the free energy change for nanoscale bud formation can be negative for nanoscale cylinders (e.g., nanocellulose paper fibers) which translated to greater efficiency in assembling GUVs using those substrates (2). Merging of nanoscale buds into microscale buds was also found to be energetically favored because the elastic energy due to curvature depended on only the number of buds, not the size of the buds (2). The sizes of GUVs are expected to be highly polydisperse for thin-film hydration methods (1, 4, 5, 52). Directly hydrating in high salt is known to negatively impact the assembly of GUVs due to the presence of ions reducing electrostatic repulsion between bilayers, effectively increasing adhesion between bilayers (7, 53–55).

However, multiple thin-film variants now exist that can counteract this effect to varying degrees and produce vesicles in physiologically relevant salt conditions (e.g., 1× phosphate-buffered saline (PBS)), such as gel-assisted hydration (1, 52) and sugar doping (56). A mechanism has been proposed that generally covers both aforementioned variants, in that osmotic pressure exerted on the membranes by dissolved polymer or sugar is responsible for counteracting the increased adhesive energy between bilayers and reduces the free energy for bud formation (57). This observation matches other literature reports that suggest GUVs formed through gel-assisted methods show contamination of the gel into the vesicle lumen or membrane and can alter the mechanical properties of the vesicle (58). A diffusive loading method that shows high yields of vesicles in physiologically relevant salt conditions will be covered in **Chapter 2**, briefly, this method first allows the assembly of microscale buds in low salt, before allowing high salt concentrations to diffuse into the vesicles.

Droplet transfer methods involve first forming an aqueous droplet stabilized by an amphiphilic monolayer before passing it through a water-oil interface where another amphiphilic monolayer is located. This results in the formation of a vesicle with a bilayer membrane. This technique is not known to have issues assembling in high salt, as the mechanisms here simply involve forming a stabilized droplet and passing through a lipid monolayer. Depending on the technique, such as microfluidic jetting (30, 47–50) it is possible to form monodispersed vesicle sizes. Other techniques such as those based on the inverted emulsion technique (43, 45, 46) or the one-pot method (42), tend to produce polydisperse vesicle sizes. There have been findings that suggest organic solvents or oil residues may remain present as contaminates in the membranes of these vesicles (59).

Depending on the intended application, different techniques may be beneficial to specific cases. But the wide range of techniques allows for vesicles to be widely adaptable to a large range of applications. Later in **Chapter 2**, the differences in encapsulation between vesicle assembly techniques will be reviewed and the characterization of a diffusive loading technique will be shown.

1.1.2 Overview of Dissertation

The focus of this dissertation will be the use of GUVs as an in vitro tool to study cellular systems. The size of GUVs is well suited to mimicking cellular volumes, and the presence of a bilayer membrane allows membrane interactions to be explored. GUVs have the potential to bridge the gap between bulk in vitro and in vivo experimentation, providing a highly controlled and customizable environment, while being able to mimic key properties of the cell. The microscale dimensions of GUVs are also well suited for imaging with optical microscopes, which allows the easy determination of the physical properties of GUVs and fluorescent labeling can allow the characterization of encapsulation into GUVs. Additionally, fluorescence can be used as a reporter for cellular systems, or even be paired with quenchers to determine more complex interactions occurring within the vesicle lumens. Localization of macromolecules can also be determined through imaging and examining structures that can form within vesicles, such as the case with cytoskeletal proteins (35–38). In general, any cellular system that can function in a cell-free setting could be a potential candidate to be studied using GUVs as the platform.

In **Chapter 2** of this dissertation, the encapsulation of proteins into GUVs through a diffusive loading technique that utilizes a cellulose paper substrate will be characterized to determine what the encapsulation efficiency, variation, and distribution will look like across a comprehensive analysis involving a range of protein concentration and vesicle sizes. This chapter will first review reports of encapsulation statistics from thin-film hydration methods and droplet-based methods and compare the differences that come from hydration versus droplet partitioning. A thorough review of what kind of cellular systems have already been incorporated into vesicles, and how the system behaved under each methodology type will be performed. Then the methodology for assembly and loading the GUVs and the steps required for the characterization of the encapsulation of a model protein, FITC-BSA, will be thoroughly described. The results of the experiments will show that encapsulation using the diffusive loading method produces a cell-like degree of variation in protein concentration across a population. The protein concentrations also follow a gamma distribution, often used to describe the distribution of protein concentration produced inside biological cells. This demonstrates the ability of the vesicles to mimic intercellular variation. Size and concentration were found to have no significant impact on the encapsulation of protein in GUVs, and the loading concentration was equal to the mean encapsulated concentration, allowing the expected distributions of proteins in vesicles to be easy to predict. The diffusive loading technique is also shown to be well suited to physiologically relevant salt conditions and can gently load sensitive proteins without exposure to non-ideal conditions (e.g., low salt conditions).

In **Chapter 3** of this dissertation, the core oscillator of a cyanobacterial circadian clock will be encapsulated into the GUVs using the diffusive loading technique that was characterized in **Chapter 2**. The effect of cell-like variations, confinement in a limited cell-like volume, and the potential for membrane interactions that were previously observed in vivo, will be studied across a range of protein concentrations. A comprehensive review of the relevant interactions of the clock proteins is performed to give context to the inner workings of the clock when it is partitioned into the GUV model. The initial results showed that the clock partitioned in vesicles behaved significantly differently than its bulk counterpart. Further investigation revealed that in the vesicles, some of the clocks were no longer capable of operating. Clock fidelity, defined as the proportion of clocks that function for a given population, was significantly hampered by cellular variation and membrane binding. A strong positive correlation between protein concentration and the surface area to volume ratio is observed for clock fidelity. In the bulk reactions, the clock rhythm simply worked without issue as long as concentration was past a critical minimum level and had little indication that higher concentrations were at all significant. Concentrations used for typical in vitro experiments with the clock showed only a ~30% fidelity in cell-sized vesicles, much less than the near 100% expected in the native cyanobacteria. When the concentration was increased to near cellular levels, this clock fidelity jumped up to ~71%, a significant improvement. From here it was determined that higher concentration counteracted variation and the size dependency was due to membrane binding reducing free clock protein concentration. A model was developed that incorporated the experimental parameters and was found to be able to reproduce the experimental data very closely. The model is used to explore hypothetical scenarios about the clock and determined that the post-translational core oscillator alone was not sufficient to maintain a highly robust clock in vivo, and must rely on other cellular components or systems, such as the transcriptional-translation feedback loop that was seen as less important because the post-translational oscillator functioned extremely robustly in bulk in vitro tests. But this changed once intercellular variation was introduced to the system, highlighting how using the GUV in vitro model can reveal important context that was not appreciated by bulk in vitro studies.

1.2 Bibliography

1. A. Cooper, V. Girish, A. B. Subramaniam, Osmotic Pressure Enables High-Yield Assembly of Giant Vesicles in Solutions of Physiological Ionic Strengths. *Langmuir* **39**, 5579–5590 (2023).
2. J. Pazzi, A. B. Subramaniam, Nanoscale Curvature Promotes High Yield Spontaneous Formation of Cell-Mimetic Giant Vesicles on Nanocellulose Paper. *ACS Appl. Mater. Interfaces* **12**, 56549–56561 (2020).
3. V. Girish, J. Pazzi, A. Li, A. B. Subramaniam, Fabrics of Diverse Chemistries Promote the Formation of Giant Vesicles from Phospholipids and Amphiphilic Block Copolymers. *Langmuir* **35**, 9264–9273 (2019).
4. J. Pazzi, M. Xu, A. B. Subramaniam, Size Distributions and Yields of Giant Vesicles Assembled on Cellulose Papers and Cotton Fabric. *Langmuir* **35**, 7798–7804 (2018).
5. A. Li, J. Pazzi, M. Xu, A. B. Subramaniam, Cellulose Abetted Assembly and Temporally Decoupled Loading of Cargo into Vesicles Synthesized from Functionally Diverse Lamellar Phase Forming Amphiphiles. *Biomacromolecules* **19**, 849–859 (2018).
6. K. M. Kresse, M. Xu, J. Pazzi, M. García-Ojeda, A. B. Subramaniam, Novel Application of Cellulose Paper As a Platform for the Macromolecular Self-Assembly of Biomimetic Giant Liposomes. *ACS Appl. Mater. Interfaces* **8**, 32102–32107 (2016).
7. P. Walde, K. Cosentino, H. Engel, P. Stano, Giant Vesicles: Preparations and Applications. *ChemBioChem* **11**, 848–865 (2010).
8. A. Weinberger, *et al.*, Gel-assisted formation of giant unilamellar vesicles. *Biophys. J.* **105**, 154–164 (2013).
9. D. J. Estes, M. Mayer, Electroformation of giant liposomes from spin-coated films of lipids. *Colloids Surfaces B Biointerfaces* **42**, 115–123 (2005).
10. P. A. Monnard, D. W. Deamer, Preparation of Vesicles from Nonphospholipid Amphiphiles. *Methods Enzymol.* **372**, 133–151 (2003).
11. K. Morigaki, P. Walde, Fatty acid vesicles. *Curr. Opin. Colloid Interface Sci.* **12**, 75–80 (2007).
12. B. M. Discher, *et al.*, Polymersomes: Tough vesicles made from diblock copolymers. *Science.* **284**, 1143–1146 (1999).
13. A. C. Greene, D. Y. Sasaki, G. D. Bachand, Forming giant-sized polymersomes using gel-assisted rehydration. *J. Vis. Exp.*, e54051 (2016).
14. J. R. Howse, *et al.*, Templated formation of giant polymer vesicles with controlled size distributions. *Nat. Mater.* **8**, 507–511 (2009).
15. D. E. Discher, A. Eisenberg, Polymer vesicles. *Science.* **297**, 967–973 (2002).

16. T. Litschel, P. Schwille, Protein Reconstitution Inside Giant Unilamellar Vesicles. *Annu. Rev. Biophys.* **50**, 525–548 (2021).

17. J. G. Bermudez, H. Chen, L. C. Einstein, M. C. Good, Probing the biology of cell boundary conditions through confinement of Xenopus cell-free cytoplasmic extracts. *Genesis* **55**, 1–10 (2017).

18. V. Noireaux, A. P. Liu, The New Age of Cell-Free Biology. *Annu. Rev. Biomed. Eng.* **22**, 51–77 (2020).

19. I. A. Chen, P. Walde, From self-assembled vesicles to protocells. *Cold Spring Harb. Perspect. Biol.* **2**, 1–14 (2010).

20. A. Kubilis, A. Abdulkarim, A. M. Eissa, N. R. Cameron, Giant Polymersome Protocells Dock with Virus Particle Mimics via Multivalent Glycan-Lectin Interactions. *Sci. Rep.* **6**, 32414 (2016).

21. H. J. Choi, C. D. Montemagno, Artificial organelle: ATP synthesis from cellular mimetic polymersomes. *Nano Lett.* **5**, 2538–2542 (2005).

22. N. P. Kamat, S. J. Henry, D. Lee, D. A. Hammer, Single-vesicle patterning of uniform, giant polymersomes into microarrays. *Small* **9**, 2272–2276 (2013).

23. A. J. Markvoort, *et al.*, Self-reproduction of fatty acid vesicles: A combined experimental and simulation study. *Biophys. J.* **99**, 1520–1528 (2010).

24. S. M. Baker, Synthetic Cells-Self-Assembling Polymer Membranes and Bioadhesive Colloids. *Integr. Med.* **4**, 10–11 (2005).

25. K. Fujiwara, M. Yanagisawa, S. M. Nomura, Reconstitution of intracellular environments in vitro and in artificial cells. *Biophysics (Oxf).* **10**, 43–48 (2014).

26. S. Li, B. Byrne, J. Welsh, A. F. Palmer, Self-Assembled Poly (butadiene)-b-poly(ethylene oxide) Polymersomes as Paclitaxel Carriers. *Biotechnol. Prog* **23**, 278–285 (2007).

27. C. Sanson, *et al.*, A simple method to achieve high doxorubicin loading in biodegradable polymersomes. *J. Control. Release* **147**, 428–435 (2010).

28. J. S. Lee, J. Feijen, Polymersomes for drug delivery: Design, formation and characterization. *J. Control. Release* **161**, 473–483 (2012).

29. A. H. Salama, M. H. Aburahma, Ufasomes nano-vesicles-based lyophilized platforms for intranasal delivery of cinnarizine: preparation, optimization, ex-vivo histopathological safety assessment and mucosal confocal imaging. *Pharm. Dev. Technol.* **21**, 1–10 (2015).

30. D. F. D. F. Do Nascimento, *et al.*, Microfluidic Fabrication of Pluronic Vesicles with Controlled Permeability. *Langmuir* **32**, 5350–5355 (2016).

31. S. H. Kim, H. C. Shum, J. W. Kim, J. C. Cho, D. A. Weitz, Multiple polymersomes for programmed release of multiple components. *J. Am. Chem. Soc.* **133**, 15165–15171 (2011).

32. N. S. Oltra, P. Nair, D. E. Discher, From Stealthy Polymersomes and Filomicelles to "Self" Peptide-Nanoparticles for Cancer Therapy. *Annu. Rev. Chem. Biomol. Eng.* **5**, 281–299 (2014).

33. P. J. Photos, L. Bacakova, B. Discher, F. S. Bates, D. E. Discher, Polymer vesicles in vivo: Correlations with PEG molecular weight. *J. Control. Release* **90**, 323–334 (2003).

34. T. Litschel, B. Ramm, R. Maas, M. Heymann, P. Schwille, Beating Vesicles: Encapsulated Protein Oscillations Cause Dynamic Membrane Deformations. *Angew. Chemie - Int. Ed.* **57**, 16286–16290 (2018).

35. I. López-Montero, *et al.*, Membrane reconstitution of FtsZ-ZipA complex inside giant spherical vesicles made of E. coli lipids: Large membrane dilation and analysis of membrane plasticity. *Biochim. Biophys. Acta - Biomembr.* **1828**, 687–698 (2013).

36. J. S. Hansen, K. Elbing, J. R. Thompson, N. Malmstadt, K. Lindkvist-Petersson, Glucose transport machinery reconstituted in cell models. *Chem. Commun.* **51**, 2316–2319 (2015).

37. B. Sun, D. T. Chiu, Determination of the encapsulation efficiency of individual vesicles using single-vesicle photolysis and confocal single-molecule detection. *Anal. Chem.* **77**, 2770–2776 (2005).

38. F. C. Tsai, B. Stuhrmann, G. H. Koenderink, Encapsulation of active cytoskeletal protein networks in cell-sized liposomes. *Langmuir* **27**, 10061–10071 (2011).

39. L. M. Dominak, C. D. Keating, Polymer encapsulation within giant lipid vesicles. *Langmuir* **23**, 7148–7154 (2007).

40. L. M. Dominak, C. D. Keating, Macromolecular crowding improves polymer encapsulation within giant lipid vesicles. *Langmuir* **24**, 13565–13571 (2008).

41. L. M. Dominak, D. M. Omiatek, E. L. Gundermann, M. L. Heien, C. D. Keating, Polymeric crowding agents improve passive biomacromolecule encapsulation in lipid vesicles. *Langmuir* **26**, 13195–13200 (2010).

42. K. Göpfrich, *et al.*, One-Pot Assembly of Complex Giant Unilamellar Vesicle-Based Synthetic Cells. *ACS Synth. Biol.* **8**, 937–947 (2019).

43. S. Pautot, B. J. Frisken, D. A. Weitz, Production of unilamellar vesicles using an inverted emulsion. *Langmuir* **19**, 2870–2879 (2003).

44. M. Tsugane, H. Suzuki, Reverse Transcription Polymerase Chain Reaction in Giant Unilamellar Vesicles. *Sci. Rep.* **8**, 1–11 (2018).

45. A. Moga, N. Yandrapalli, R. Dimova, T. Robinson, Optimization of the Inverted Emulsion Method for High-Yield Production of Biomimetic Giant Unilamellar Vesicles. *ChemBioChem* **20**, 2674–2682 (2019).

46. B. Xu, J. Ding, J. Xu, T. Yomo, Giant vesicles produced with phosphatidylcholines (Pcs) and phosphatidylethanolamines (pes) by water-in-oil inverted emulsions. *Life* **11** (2021).

47. C. W. Coyne, *et al.*, Lipid Bilayer Vesicle Generation Using Microfluidic Jetting. *J. Vis. Exp.*, 1–6 (2014).

48. M. Sun, Z. Li, S. Wang, G. Maryu, Q. Yang, Building Dynamic Cellular Machineries in Droplet-Based Artificial Cells with Single-Droplet Tracking and Analysis. *Anal. Chem.* (2019) https:/doi.org/10.1021/acs.analchem.9b01481.

49. Y. C. Tan, K. Hettiarachchi, M. Siu, Y. R. Pan, A. P. Lee, Controlled microfluidic encapsulation of cells, proteins, and microbeads in lipid vesicles. *J. Am. Chem. Soc.* **128**, 5656–5658 (2006).

50. A. Jahn, W. N. Vreeland, M. Gaitan, L. E. Locascio, Controlled Vesicle Self-Assembly in Microfluidic Channels with Hydrodynamic Focusing. *J. Am. Chem. Soc.* **126**, 2674–2675 (2004).

51. K. Morigaki, P. Walde, Giant vesicle formation from oleic acid/sodium oleate on glass surfaces induced by adsorbed hydrocarbon molecules. *Langmuir* **18**, 10509–10511 (2002).

52. K. S. Horger, D. J. Estes, R. Capone, M. Mayer, Films of agarose enable rapid formation of giant liposomes in solutions of physiologic ionic strength. *J. Am. Chem. Soc.* **131**, 1810–1819 (2009).

53. H. Stein, S. Spindler, N. Bonakdar, C. Wang, V. Sandoghdar, Production of isolated giant unilamellar vesicles under high salt concentrations. *Front. Physiol.* **8**, 1–16 (2017).

54. K. I. Akashi, H. Miyata, H. Itoh, K. Kinosita, Preparation of giant liposomes in physiological conditions and their characterization under an optical microscope. *Biophys. J.* **71**, 3242–3250 (1996).

55. C. Has, P. Sunthar, A comprehensive review on recent preparation techniques of liposomes. *J. Liposome Res.* **30**, 336–365 (2020).

56. K. Tsumoto, H. Matsuo, M. Tomita, T. Yoshimura, Efficient formation of giant liposomes through the gentle hydration of phosphatidylcholine films doped with sugar. *Colloids Surfaces B Biointerfaces* **68**, 98–105 (2009).

57. A. Cooper, V. Girish, A. B. Subramaniam, Osmotic pressure enables high yield assembly of giant vesicles in solutions of physiological ionic strengths. *Langmuir* (2023).

58. R. B. Lira, R. Dimova, K. A. Riske, Giant unilamellar vesicles formed by hybrid films of agarose and lipids display altered mechanical properties. *Biophys. J.* **107**, 1609–1619 (2014).

59. S. R. Kirchner, *et al.*, Membrane composition of jetted lipid vesicles: A Raman spectroscopy study. *J. Biophotonics* **5**, 40–46 (2012).

Chapter 2: Characterization of encapsulation: Cell-like variation through diffusive loading technique in giant vesicles.

2.1 Introduction

Giant unilamellar vesicles (GUVs) fall into the same size range as biological cells and similarly allow the containment of molecules enclosed within a lipid bilayer membrane. There has been potential for GUVs to be used as a minimal cell model for the study of cellular systems (16–18) or used to build synthetic cells in a bottoms-up approach (60–63). Matching cellular volume can be important when considering the stochastic interactions of molecules and the partitioning of low copy number molecules (64–67). The presence of a membrane can allow for the observation of membrane binding interactions or applications involving the use of transmembrane proteins (35–38). In this chapter, there will be a focus on the variation of encapsulated solutes produced by various GUV assembly methods and comparisons to a modulated loading technique that will be demonstrated to mimic the distribution and magnitude of variation for proteins inside biological cells.

A variety of methods have been demonstrated for partitioning biomacromolecules into cell-like volumes for in vitro experimentation, whether by partitioning into water-in-oil emulsions (droplets) (48, 68, 69), vesicles formed from lipids (34, 38–41, 70–74) or other amphiphiles (5), or PDMS micro containers (75). This includes a wide range of cell-free systems or other biomacromolecules that has been encapsulated into droplets or vesicles to understand the effect of partitioning into cell-sized volumes or interactions with lipid bilayer membranes, including Xenopus egg extracts (48, 68), other transcriptional oscillators (69), transcription-translation (TXTL) gene expression systems (70–74), polymerase chain reactions (PCR) (44), bacterial cell division machinery (34), and various membrane or cytoskeletal proteins (35–38). The following sections will review the different methods of encapsulating or partitioning a volume into cell-sized volumes in droplets and vesicles and the encapsulation statistics the field has reported across various experiments. The sections will be separated into two overarching methodologies, droplet-derived partitioning, and encapsulation using thin film hydration.

2.1.1 Encapsulation in droplet-derived partitioning

Encapsulation of solutes in droplets (48, 68, 69) and vesicles (43, 70, 71, 73, 76, 77) assembled from droplet transfer methods both share a premise of partitioning a solution into amphiphile stabilized droplets suspended in an oil phase. The droplets are stabilized by a monolayer of the amphiphiles, with the hydrophobic group facing out into the oil phase. For vesicle assembled from droplet transfer methods, an extra step is performed where the droplet is passed through the interface of an oil-water phase containing a monolayer of amphiphilic molecules, such as phospholipids, to form a bilayer around the droplet, forming a vesicle (43, 76, 77). Therefore, the actual partitioning of solutes between droplets and droplets transferred vesicles are identical. The primary difference is the presence of a bilayer membrane and suspension in an aqueous phase in the end product. Partitioning of solutes from these methods is expected to be independent random events and follow a Poisson distribution for the expected number of encapsulated solutes in the droplet (67, 69, 70, 75). In Poisson distributions, the standard deviation (SD) is equal to the square root of the mean (μ) (Eq. 1).

$$SD = \sqrt{\mu} \qquad \textbf{Eq. 1}$$

The mean is equal to the average number of molecules (n_0) expected inside a droplet, which can be defined by **Eq. 2** as a function of Avogadro's number (N_A), concentration (C_0), and droplet volume (V).

$$\mu = n_0 = N_A C_0 V \qquad \textbf{Eq. 2}$$

The coefficient of variation (CV) can then be defined solely as a function of the average number of molecules (n_0) in **Eq. 3** using **Eq. 2** and **Eq. 1**.

$$CV = \frac{SD}{\mu} = \frac{\sqrt{\mu}}{\mu} = \frac{\sqrt{n_0}}{n_0} = \frac{1}{\sqrt{n_0}} \qquad \textbf{Eq. 3}$$

This means for droplet-based partitioning, the theoretical encapsulation variation can be calculated by the expected number of molecules for a given volume and concentration. For very small n_0, the CV is high, and for very large n_0, the CV is small. This becomes especially relevant for the encapsulation of biomacromolecules such as messenger RNA (mRNA) or DNA, which are typically present in very low nanomolar concentrations, so the CV would be large (67, 70, 72). For example, if a n_0 in the order of ~10 RNA molecules is expected in a droplet with cell-like volumes, then the CV would be ~32%. However, for typical protein concentrations which are commonly in the µM range, a n_0 on the order of ~10000 protein molecules which can be expected in a droplet with cell-like volumes, will have a minimal CV in the order of ~1%.

Encapsulating cell-free transcription and gene expression systems with droplet-based partitioning seems to generally agree with a Poisson distribution model for partitioning statistics, where the variability in the transcription and/or translation behavior of the system is reported to be close to the expected theoretical CV based on the variation of low copy number components (48, 68–71). One report suggested broader than Poisson variability and found using a Gamma distribution, which is often used for describing the cellular variation, in their models showed more similar results to the experimental data (69). It was suggested that other factors, such as denaturation of protein or inactivation due to adsorption on droplet interface, could lead to broader than Poisson variability (69). Ultimately, it was still determined it was partitioning effects that were the source of variability in droplet and droplet-derived vesicles (48, 68–71).

Size-dependent behaviors that are consistent with partitioning statistics are reported, with smaller droplet or vesicle sizes showing greater variability in the period and reduced number of oscillations for transcription for Xenopus extracts (68), greater variability in the period and amplitude of transcriptional oscillators (69), and greater variability of gene expression products for TXTL systems (70). The general conclusions from droplet partitioning results show that cell-like variation is largely an intrinsic property of gene expression due to the partitioning of low copy number components (70).

2.1.2 Encapsulation in thin-film hydration methods

It could be initially expected that thin film hydration would follow similar partitioning statistics because the proteins are present in the hydration solution when it is partitioned into vesicles. However, the encapsulation of solutes in vesicles assembled from thin-film hydration methods does not follow a Poisson-like distribution (37–41). For example, polymers and proteins encapsulated into GUVs assembled through thin-film hydration on glass have shown a CV as high as 30 – 60 %, when partitioning statistics in Eq. 3 would have only predicted a CV on the order of ~1% (39–41). Or when cell-free TXTL systems are encapsulated using a thin-film hydration method, combined with freeze-thaw encapsulation, showed only ~30% of vesicles successfully expressed detectable amounts of yellow fluorescent protein (YFP) (72), while cell-free TXTL systems from droplet partitioning methods did not report similar findings of non-expressing vesicles (70, 73). While there are studies looking at the encapsulation variation of thin-film methods, there are limited quantitative characterizations of the distributions of encapsulated solutes and varying estimates of encapsulation efficiencies from ~30 % to >100 % (37–41). These encapsulation properties of thin-film methods have led to the perception that thin-film based methods may be suboptimal for studies involving encapsulated cellular systems in favor of droplet transfer methods (16).

Studies of small unilamellar vesicles (SUVs, 100 – 200 nm in diameter) assembled using thin-film hydration followed by extrusion and in one case, freeze-thaw cycles (78), found that the encapsulation of very low concentrations (~0 – 4 molecules expected per SUV) of DNA, RNA, or protein closely follow a Poisson distribution (78, 79). However, the extent that extrusion and freeze-thaw cycling had to play are unknown. In this case, the Poisson variance could be expected to dominate as the mean molecule numbers are very low. When molecular copy numbers are high, the dominant source of variation seen in thin film encapsulation is expected to remain at a constant CV even with varying concentrations. But as the mean number of molecules approaches zero, the variation attributed from a Poisson distribution would continue to increase and can dominate.

2.1.3 The modulated loading paper-based thin film hydration method

This chapter will demonstrate a cellulose paper-based thin-film method (2–4, 6) combined with a diffusive loading technique (5) that can assemble GUVs in high salt and efficiently encapsulate proteins in a way that mimics cell-like variability while maintaining protein functionality. This technique is termed **o**ne-**s**tepped **m**odulated **p**aper-abetted **a**m**p**hiphile h**y**d**r**ation in aq**u**eous **s**olution or OSM-PAPYRUS. Quantitative analysis of large vesicle populations (average of ~1300 vesicles per sample) show encapsulated protein distributions follows a gamma distribution often cited to describe protein variation in biological cells (80–83) and a cell-like coefficient of variation (CV) of ~0.3 (84, 85). The quantitative characterization of this technique demonstrates the novel ability to mimic cell-like variation on even high molecular copy number species of cellular systems encapsulated into an *in vitro* GUV-based minimal cell model. Later in **Chapter 3,** a demonstrated application of this technique is used to study the effect of cell-like variation on cyanobacterial circadian clock systems.

Encapsulation of solutes from vesicles assembled from this diffusive loading method follows a different premise from droplet partitioning and other thin-film methods. In the case of droplets, an aqueous solution is simply partitioned by mechanical action into amphiphile stabilized droplets in an oil phase. In the case of typical thin-film hydration, the vesicles form from rehydrated lipid films with the presence of protein, here, it will be termed spontaneous encapsulation. For diffusive loading with OSM-PAPYRUS, the vesicle buds are first allowed to assemble in a low-salt solution without the intended cargo. Then solutes are added to the external phase and diffusively load into surface-attached spherical buds and GUVs, which remain open to the external environment through their surface tethers (5). This step is phased so that salt buffers can be loaded first to ensure the environment is optimized to persevere the functionality of sensitive proteins. Then the proteins are diffusively loaded after. As lipid bilayers are impermeable to most proteins and other macromolecules, solutes must diffuse between the bilayer stacks on the surface and then into the buds or GUVs through the surface tethers.

One benefit of using OSM-PAPYRUS is to allow the assembly of vesicles using the thin film hydration principles in high or physiologically relevant salt solutions and the ability to encapsulate protein in a buffer optimized environment to prevent degradation of function. Typically, thin film methods cannot produce vesicles efficiently in physiologically relevant salt conditions in part due to decreased repulsion between bilayers (7, 53, 55, 56, 86). Recently, other methods, such as gel-assisted hydration, which is a modified thin film method using hydrogels as the substrate, have been shown to produce vesicles in physiologically relevant salt conditions (52, 87). However, there are significant concerns regarding the contamination of dissolved hydrogels that are encapsulated within the vesicle (58). Because OSM-PAPYRUS uses a cellulose paper substrate, which is generally known to be insoluble in water (88), there would be no expected contaminants that are transferred to the vesicle lumens. Contamination is also of concern for droplet-derived vesicles, which can trap organic solvents in the bilayers (89). This possible contamination may be a concern for uses in the healthcare industry or even as unexpected variables that could affect protein binding or the behavior of cellular systems. A study found pre-doping the lipid film with sugars can produce GUVs in the presence of salt due to increased bilayer distance due to the osmosis of water into the bilayer due to the concentration gradient from the sugar (56). However, in physiologically relevant salt levels (Tris-100 mM NaCl), the number of GUVs produced dropped by more than a factor of 10, producing only tiny numbers of vesicles. But a more recent study found sugar doping was ineffective in producing GUVs in 1× PBS when considering molar yields of lipids (1).

2.2 Materials and Methods

2.2.1 Materials

The following was purchased, Gold Seal™ 60 × 22 mm glass coverslips, Fisherbrand ™ Premium Plain Glass Microscope Slides (75 mm × 25 mm), CELLSTAR® black clear bottom 96 well plates (Greiner), Coplin glass staining jars (DWK Life Sciences), Corning® 15 mm diameter regenerated cellulose syringe filters (0.2 µm pore size), and MilliporeSigma™ Ultrafree™-MC centrifugal filter devices (0.22 µm pore size) from Thermo Fisher Scientific (Waltham, MA). The following was purchased, artist grade tracing paper (Jack Richeson & Co., Inc.), circular hole punches (EK Tools Circle Punch, 3/8 in.), square hollow punch cutters (Amon Tech) from Amazon Inc. (Seattle, WA).

2.2.2 Chemicals

The following was purchased, sucrose (BioXtra grade, purity ≥ 99.5%), glucose (BioXtra grade, purity ≥ 99.5%), bovine albumin-fluorescein isothiocyanate conjugate (FITC-BSA) (albumin from bovine, ≥ 7 mol FITC/mol albumin), sodium chloride (NaCl) (ACS grade, VWR International), manganese (II) chloride tetrahydrate ($MgCl_2$) (ReagentPlus grade, ≥ 99%, Sigma-Aldrich), and ethylenediaminetetraacetic acid (EDTA) (BioReagent grade ≥ 98.5%) from Sigma-Aldrich (St. Louis, MO). We purchased chloroform (ACS grade, purity ≥ 99.8%, with 0.75% ethanol as preservative), 1 N potassium hydroxide (KOH) (Certified grade, 0.995 to 1.005N, Fisher Chemical), 3-aminopropyl trimethoxysilane (APTES) (≥ 98.5%, ACROS Organics), glacial acetic acid (ACS grade, ≥ 99.7%, Fisher Chemical), methanol (ACS grade, ≥ 99.8%, Fisher Chemical), adenosine 5'-triphosphate (ATP solution) (Tris-buffered, > 99% purity via HPLC, Thermo Scientific) from Thermo Fisher Scientific (Waltham, MA). 18.2 MΩ ultrapure water was obtained from an ELGA Pure-lab Ultra water purification system (Woodridge, IL). The following was purchased, 1,2-dioleoyl-*sn*-glycero-3-phosphocholine (18:1 (Δ9-cis) PC (DOPC)), 1,2-distearoyl-*sn*-glycero-3-phosphoethanolamine-N-(methoxy(polyethylene glycol)-2000) (18:0 DSPE-PEG2K), 1,2-distearoyl-*sn*-glycero-3-phosphoethanolamine-N-(biotinyl(polyethylene glycol)-2000) (DSPE-PEG2K-Biotin), and 1,2-dioleoyl-*sn*-glycero-3-phosphoethanolamine-N-(Lissamine rhodamine B sulfonyl) (RhPE) from Avanti Polar Lipids, Inc. (Alabaster, AL). NHS-ester polyethylene glycol (mPEG) (5 kDa) and biotinylated NHS-ester PEG (biotin-mPEG) (5 kDa) was purchased from Laysan Bio, Inc. (Arab, AL).

2.2.3 Preparation of buffers for giant vesicle assembly

A 10× clock buffer stock is prepared, which consists of 200 mM Tris, 1500 mM NaCl, 50 mM MgCl2, 10 mM ATP, and 5 mM EDTA. The 1× clock buffer consists of 20 mM Tris, 150 mM NaCl, 5 mM $MgCl_2$, 1 mM ATP, and 0.5 mM EDTA, and is based on the buffer optimized for cyanobacterial circadian clock proteins (90). A 1 M sucrose and 1 M glucose stock solution is prepared. All buffers and solutions are filtered through a 0.2 μm pore regenerated cellulose syringe filter. The initial budding buffer consists of 119 mM sucrose. The final buffer composition after vesicle assembly is complete consists of 1× clock buffer and 100 mM sucrose. The sedimentation buffer is equimolar with the budding buffer, consisting of 100 mM glucose and 1× clock buffer.

2.2.4 Amphiphile mixtures

The standard lipid mixture used in studies with lipid vesicles consists of a 1 mg/mL solution of DOPC:DSPE-PEG2K:DSPE-PEG2K-Biotin:RhPE (94.4:5.0:0.5:0.1 mol%) in chloroform. Here, DOPC (94.4 mol %) is our primary vesicle forming model phospholipid. DSPE-PEG (5.0 mol %) is a PEG functionalized lipid that will provide steric repulsion and has a primary role of inhibiting aggregation of vesicles in high salt. DSPE-PEG2K-Biotin (0.5 mol %) is a biotin-PEG functionalized lipid that allows biotin-streptavidin binding interactions used for immobilizing vesicles to biotin-streptavidin functionalized glass surfaces. RhPE is a rhodamine functionalized lipid that allows the visualization of bilayer membranes.

2.2.5 Protein loading solutions

Protein loading solutions are prepared at 15× the intended final protein concentrations in 1× clock buffer. FITC-BSA is used as the model protein for investigating encapsulation into GUVs. To obtain a final concentration of 0.88, 1.75, 2.63, and 4.5 μM of FITC-BSA, 15× loading solutions will consist of 13.2, 25.25, 39.45, and 67.5 μM of FITC-BSA, respectively.

2.2.6 Preparation of biotin-PEG functionalized glass

Biotin-PEG functionalized glass allows vesicles to be bound to the glass surface through streptavidin-biotin interactions, effectively preventing lateral and axial diffusion of the vesicles during imaging. The amphiphile mixture used to assemble vesicles must contain a biotinylated lipid for this methodology to work. This procedure that is outlined below is primarily based on procedures originally developed by Chandradoss et al. (91) with some modifications.

First, ten 60 × 22 mm glass coverslips and ten 75 × 25 mm glass slides are each marked with a small line in the top right corner using a diamond scribe pen. This allows quick identification of which surface will be functionalized. Working in a chemical safety hood, the ten marked glass coverslips and ten marked glass slides are placed together into a Coplin glass staining jar in a way where each of the five slots will contain one glass coverslip and one glass slide with the surface to be functionalized facing away from one another. Even if only the coverslips are used, include the glass slides so the coverslips will stay within the slots in the Coplin glass staining jar. The Coplin glass staining jar should be maintained clean and reserved for glass functionalization. Fill the jar containing the glass with 50 mL of ultrapure water, then swirl the jar, discard the water, and then repeat these steps two more times. Then fill the jar with 50 mL of acetone and sonicate the jar for 20 minutes in a bath sonicator. Discard the acetone and rinse with ultrapure water three times. Next, fill the jar with 50 mL of 1 N KOH and sonicate the jar in a bath sonicator for 30 minutes. Remove the jar from the sonicator and leave it in the fume hood overnight to allow KOH to continue to etch the glass.

The next day, prepare a 50 mL silanization mixture in methanol of 3-aminopropyl trimethoxysilane (APTES) and acetic acid at 10 v/v% and 5 v/v%, respectively. Discard KOH in the jar to the waste, then rinse with ultrapure water three times. Then add the silanization mixture into the jar and incubate for 30 minutes. Afterward, discard the silanization mixture and rinse with 50 mL of neat methanol for a total of 3 times. Then, dry the coverslips using a stream of ultrapure nitrogen gas from a nitrogen gun. Next, create a humidity chamber using an empty 10-100 or 100-1000 plastic pipette tip box with the insert included and fill the box with 20 mL of ultrapure water (**Fig. 2.1A-B**).

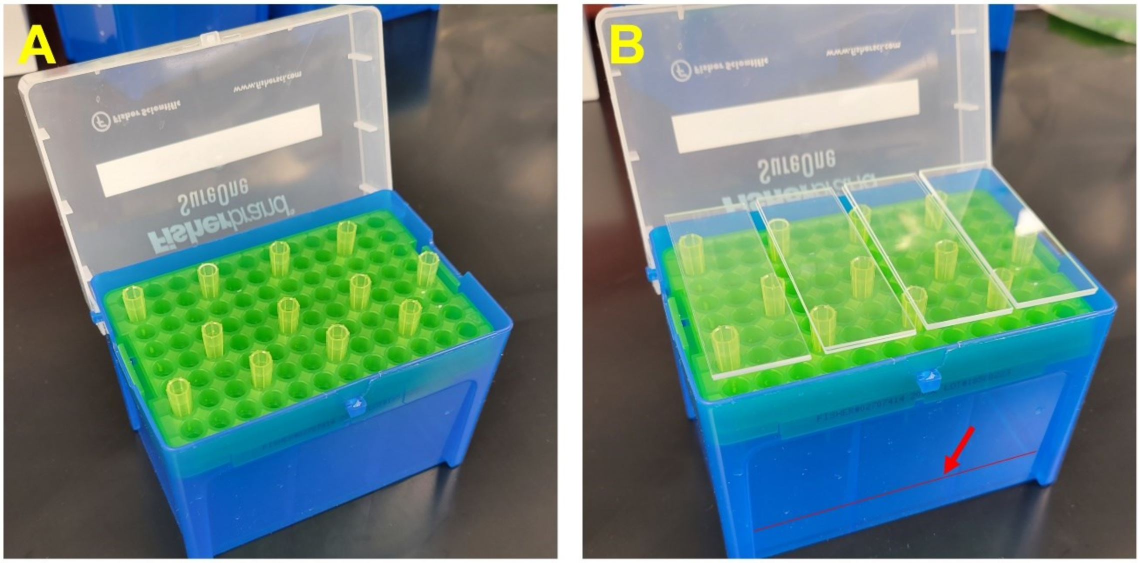

Fig. 2.1. Humidity chamber for slide functionalization. (A) Arrangement of empty pipette tips in a pipette box to store glass during glass functionalization. **(B)** Two-layer glass sandwiched with the PEG-Biotin functionalization solution in between them. A red arrow and line indicate the fill line for water.

Prepare a mixture of NHS-ester polyethylene glycol (PEG) (5 kDa) and biotinylated NHS-ester PEG (5 kDa) at a concentration of 125 mg/mL and 3.1 mg/mL, respectively, in 0.1 M sodium bicarbonate buffer (pH 8.5). Deposit 64 µL of this mixture so it is sandwiched between two sets of coverslips or slides from the staining jar. Then place it into the humidity chamber propped up by pipette tips slotted in place on top of the plastic insert (**Fig. 2.1B**). Avoid trapping air bubbles between the glass, instead, gently press the glass together to push large air bubbles out. Close the lid of the humidity chamber and place the glass into a dark and cool place, such as a cabinet. Allow the functionalization to continue overnight. The next day slide the glass sandwiches apart and rinse the functionalized surface with excess running ultrapure water. Dry the glass by blowing a steady stream of ultrapure nitrogen gas from a nitrogen gun. Store each pair of glass slides and coverslips in a 50 mL Falcon^{TM} centrifuge tube so the functionalized sides are not in contact with each other, then store the tubes in a -20 °C freezer until use.

2.2.7 Giant vesicle assembly using PAPYRUS

While working in a chemical safety hood, 10 μL of a 1 mg/mL lipid solution of DOPC:DSPE-PEG2K:DSPE-PEG2K-Biotin:RhPE (94.4:5.0:0.5:0.1 mol %) in chloroform is deposited onto a 9.5 mm diameter circular cutout of tracing paper using a Hamilton glass syringe. The lipid is dispensed slowly, nearly parallel to the paper, while simultaneously using the long edge of the syringe tip to evenly spread the lipid across the tracing paper until the chloroform evaporates. During this process, the tracing paper is held by tweezers and is not placed down until the chloroform has completely evaporated. After the chloroform has visually evaporated, the lipid-coated tracing paper is placed into a vacuum chamber for 1 hour to ensure the removal of any residual chloroform. This summarizes the core PAPYRUS method that has been developed by the Subramaniam group (2–6). From here, the method splits into various variants that allow decoupling of loading and assembly conditions, assembly in high salt, and gentle protein loading.

2.2.7.1 Diffusive loading with OSM-PAPYRUS

The one-stepped modulated (OSM) PAPYRUS method allows giant unilamellar vesicle (GUV) assembly in high salt conditions by first allowing budding to occur under optimal low salt conditions (**Fig. 2.2A**). Diffusive loading is then used to introduce high salt buffers into the vesicle buds through nanotube tethers (**Fig. 2.2A**). During this the assembly and loading process nanobud merging is occuring (**Fig. 2.2B**), in which nanobuds merge to form larger buds. Eventually these nanobuds will merge into micrometer scale buds (**Fig. 2.2C**). For all OSM-PAPYRUS experiments, the assembly and loading steps are done at room temperature. It is possible to perform either the assembly or loading steps at individually differing temperatures as done in if amphiphile or protein of choice requires elevated or lower temperatures.

First a polydimethylsiloxane (PDMS) gasket (10 mm $Ø_{OD}$ × 6 mm $Ø_{ID}$ × 1 mm) is affixed onto a clean glass slide to form a PDMS vesicle assembly chamber. Then the amphiphile coated tracing paper is removed from the vacuum chamber and placed in the PDMS assembly chamber. Then 15 μL of sucrose is mixed with 111 μL of ultrapure water and then added together into the assembly chamber with the paper. Then 3 minutes of incubation time is given for vesicle buds to form. Vesicle buds can form optimally under this low ionic strength solution. Then 14 μL of the concentrated 10× clock buffer is added underneath the paper, which diffuses through the external phase and into the vesicles through nanotube tethers that keep the vesicle buds attached to the surface of the paper. The concentrated buffer is added beneath the paper to ensure the concentration gradient is not above the vesicle buds so that the buds do not collapse due to the diffusion of water out of the buds. Then 10 μL of 15× protein solution is added directly to the external phase, above the paper substrate, and given an additional 110 minutes of time for the protein to diffuse into the vesicles. Because the buffer conditions of the proteins can be optimized during the high salt loading step the protein will not risk denaturation, allowing the gentle encapsulation of the sensitive proteins through the same nanotube tether pathway. **Table 1** summarizes the addition and steps for OSM-PAPYRUS.

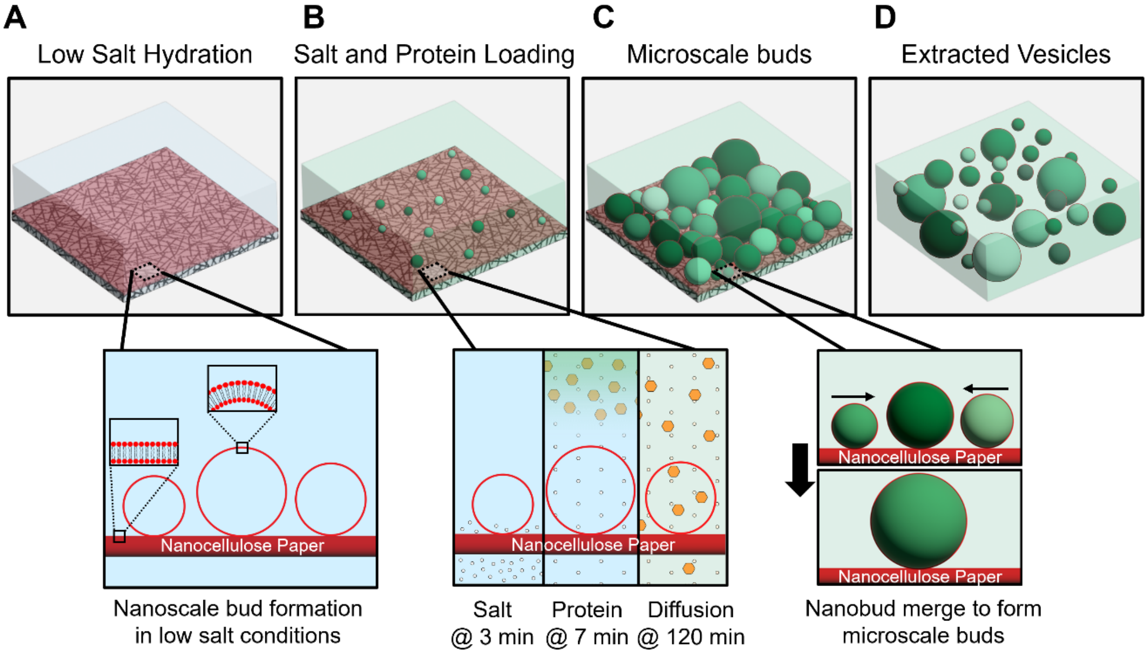

Fig. 2.2. Assembly of giant unilamellar vesicles (GUVs) using a stepped formation method (OSM-PAPYRUS). (A) Starting in the nanoscale, nano-sized buds form in low salt conditions for 3 minutes, then concentrated salt buffers (white circles) are added to the external phase beneath the paper. The salt will diffuse into the buds through the membrane tethers. Proteins are added at T = 7 minutes to the external phase and will only be exposed to the optimal buffer conditions to avoid denaturing. A total of 120 minutes **(B)** Nano-sized buds continuously merge into larger buds during the assembly and loading process. **(C)** In the micron scale, the cellulose paper substrate can be seen with many cellulose fibers. Merging nanobuds eventually form larger micron-scale buds. **(D)** Pipette aspiration extracts vesicles from the surface of the paper and becomes fully enclosed. Variation of protein concentrations between vesicles can be seen, indicated by shades of green.

The vesicles are then extracted by aspirating with a 100-1000 μL pipette set at a volume displacement of 150 μL for a total of six times over different spots on the paper. This will detach the buds from the surface of the paper and allow them to become fully enclosed by the phospholipid bilayer membrane and thus closed off from the external phase. Water may still diffuse through the phospholipid membrane, but most macromolecules, such as proteins, cannot. One important note of the diffusive loading process with OSM-PAPYRUS is due to the physical disturbances of adding salts or proteins to the sample, some buds detach prematurely and become enclosed vesicles before the cargo can be loaded, resulting in the presence of some empty vesicles (**Fig. 2.2D**).

Table 1. Table of additions and incubation times for OSM-PAPYRUS

Step	Name	Concentration	Volume	Incubation Time
Low Salt Assembly	Ultrapure water	--	111 μL	3 min
	Sucrose	1000 mM	15 μL	
Diffusive Loading	Clock buffer	10×	14 μL	7 min
	FITC-BSA (1 × clock buffer)	15×	10 μL	110 min
End	Final Composition	100 mM Sucrose, 1× Clock buffer, 1× FITC-BSA	Total: 150 μL	Total: 120 min

2.2.8 Sample preparation and imaging

A custom imaging chamber is used for imaging the extracted vesicles. To make this chamber, a PEG-biotin functionalized glass coverslip is split into two equal parts (~30 × 22 mm), widthwise, using a diamond scribe. Then a circular PDMS gasket (Ø = 10 mm) with an internal 6 mm × 6 × mm × 1 mm square chamber is affixed to one half of the PEG-biotin functionalized glass coverslip (**Fig. 2.3A**). The affixation of the PDMS gasket and the glass should form a sufficient seal through van der Waals interactions, as long as both the PDMS gasket and glass are highly clean and free from dust. The PDMS gasket will not permanently bond unless the PDMS and glass are plasma cleaned first, but in this use case, a non-permanent bonding is sufficient and allows easier cleaning and reuse of the PDMS. Then 20 μL of 0.1 mg/mL streptavidin is added to the chamber and allowed to incubate for 15 minutes. Then the streptavidin is completely removed with a pipette and discarded, and the streptavidin-coated coverslip is then washed five times with 60 mL of the sedimentation buffer to remove any unbound streptavidin. After washing, we add 30 μL of the harvested vesicle solution to the chamber and then 30 μL of the sedimentation buffer. The chamber is then sealed with a 22 × 22 mm square coverslip. Wait 3 hours for the vesicles to sediment to the bottom of the chamber and bind to the streptavidin-treated glass through biotin-streptavidin interactions.

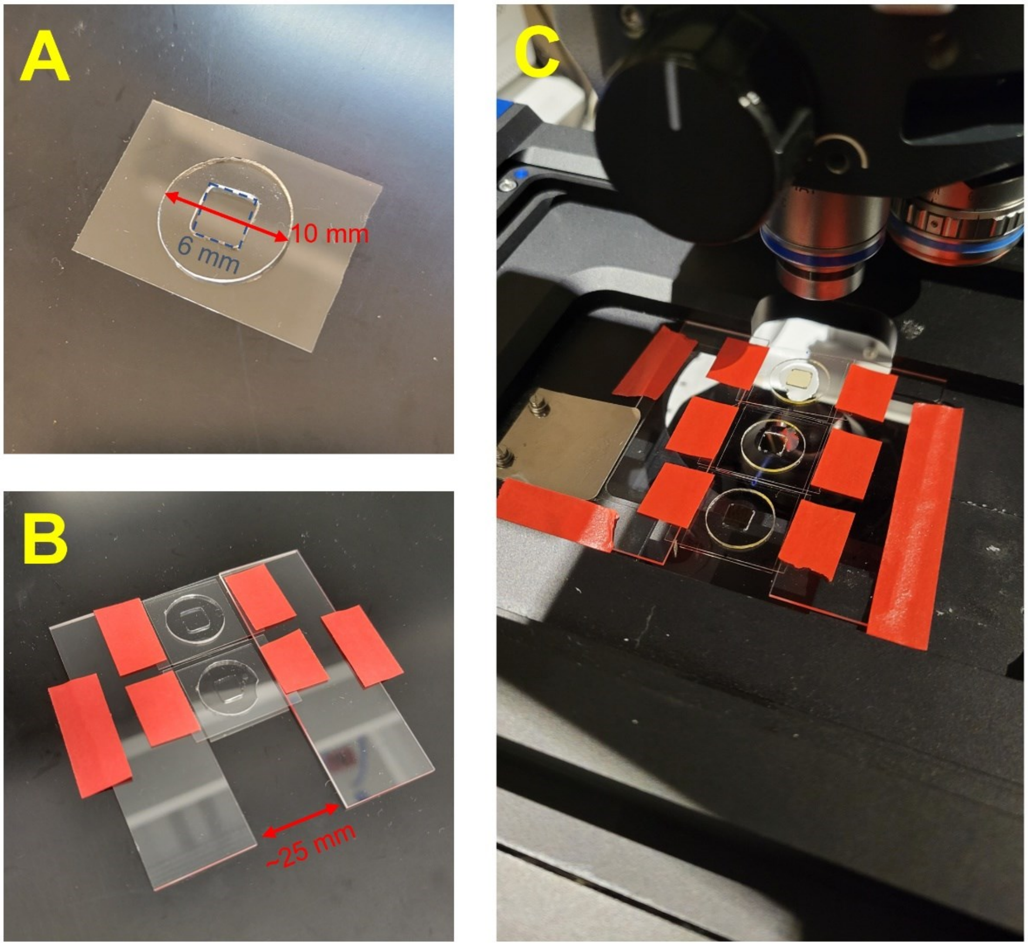

Fig. 2.3. Imaging chamber and microscope adapter. (A) PDMS gasket (Ø =10 mm) with a square chamber (6 × 6 × 1 mm) is adhered onto a functionalized coverslip. **(B)** After sedimentation, the sample is flipped and placed into an imaging adapter. The passivated coverslip rests between the two glass slides and is taped down. **(C)** Imaging adapter is secured onto the LSM 880 microscope.

Prior to imaging, the vesicle sample is flipped upside down, so the bound vesicles are now at the top surface, which allows imaging using high NA but low working distance objectives on upright microscopes. The sample is placed in a custom-made stage adapter that allow the imaging chamber to hang by the top coverslip (**Fig. 2.3B**). This ensures that the imaging plane is flat and square with the microscope stage. Not using this adapter can allow PDMS gaskets that are not completely flat to cause the imaging plane to be angled. This adapter is simply made by placing two glass slides (75 × 25 mm) parallel along the length with a spacing of 25 mm between them. Then tape the two glass slides down so they do not move. The samples can now be placed between the glass slides so that the top surface (after the prior flipping) hangs between the two glass slides. Then tape the samples to the glass slides. Up to three samples can fit on this imaging adapter and remain imageable by the microscope, if care is taken to place the samples closely together and towards the any one end of the adapter.

A Zeiss LSM 880 upright microscope, with a Zeiss 63× 1.4 NA Oil Plan-Apochromat objective is used to image the samples. The imaging adapter with the samples are placed onto the microscope (**Fig. 2.3C**) and secured with tape. Immersion oil is added to the top of each sample prior to imaging. Two imaging channels are set up alternating every line. The 'red' vesicle membrane channel is set up to image rhodamine-PE lipids was configured with 2.5% power for the 561 nm diode-pumped solid-state (DPSS) laser and a detector gain of 700 A.U. for the confocal photomultiplier tube (PMT) detector. The 'green' protein channel is setup to image FITC-BSA was configured with 2% power for the 488 nm argon laser and a detector gain of 650 A.U. for the gallium arsenide phosphide (GaAsP) detector. The pinhole diameter is set to 1 A.U., corresponding to a 0.7 μm thick optimal section in the z-plane. A 7×7 tilescan, consisting of 49 images covering a region of 135 × 135 μm per image, is taken using reflection-based autofocusing with an offset of 3 μm into the sample from the glass surface. The image resolution is set to 1584×1584 pixels with 4× line averaging applied.

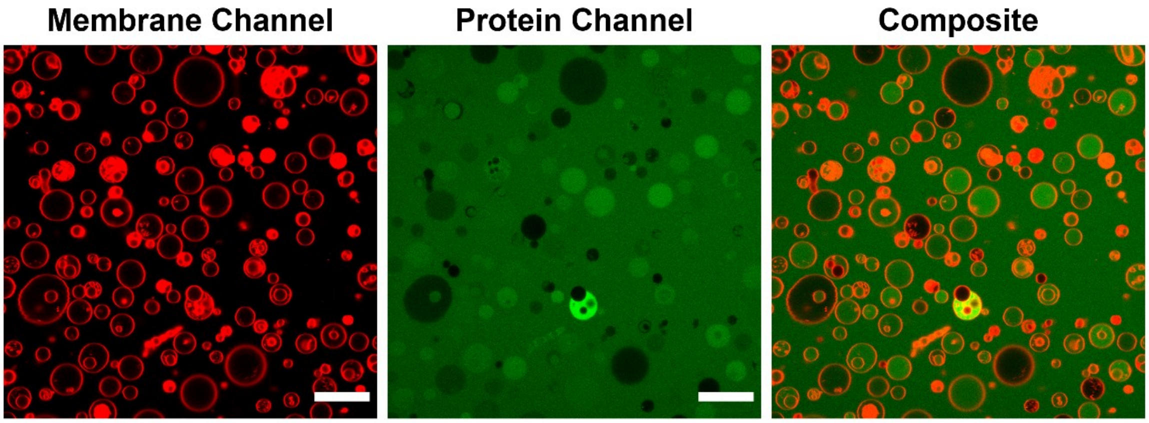

Fig. 2.4. Example of an image captured with two channels. The membrane channel of giant unilamellar vesicle (GUV) (left, red) shows the membranes of vesicles labeled with Rhodamine-PE. The protein channel (middle, green) shows the fluorescently labeled FITC-BSA proteins encapsulated in the vesicles and present in the background. A composite image (right) shows the membrane forms the boundary around the interior of the vesicles. FITC-BSA concentration here is 2.63 μM. Scale bars: 20 μm.

2.2.9 GUV Image Analysis and Processing

The following MATLAB-based GUV image analysis and processing routines have been in part adapted and modified from code that has been codeveloped by colleagues in the Subramaniam lab. MATLAB functions will be denoted by *italicized* text. The images taken using this protocol contain a known concentration of protein in the background, which allows us to create an intensity to concentration calibration curve. All images are represented as grayscale bitmaps with a single intensity value for each pixel per channel. Any color is false-colored and added in post processing for visual identification of different channels.

2.2.9.1 Watershed Segmentation

Vesicle images for this chapter contains two image channels, first the GUV membrane channel which contains intensity data in the presence of phospholipid membranes, and second the protein channel which contains intensity data relative to the concentration of proteins in a given voxel volume. The GUV membrane channel **Fig. 2.5A** is used to determine the location of GUVs and other phospholipids containing objects (e.g., aggregates, multilamellar vesicles (MLVs), and multivesicular vesicles (MVVs)). The image is first sharpened (*imsharpen*) to make the border of the objects more pronounced (**Fig. 2.5B**), which helps with accurate detection of object borders. The sharpening radius value, defined as the standard deviation (SD) of the Gaussian lowpass filter, is set to 5 pixels and the strength of the sharpening effect is set to a scalar of 3. This sharpening is noted to be more important when using high NA objectives and rhodamine fluorophores, as the border intensity may fluctuate and cause circular hollow objects to not be recognized as single entity. Then a flood-fill operation is implemented (*imfill*) for holes in the image so objects become fully filled (**Fig. 2.5C**). Holes here are defined as objects that cannot be filled by flood-filling the background from the edge of the image. The image is then binarized using Otsu's method to obtain multilevel thresholds (*multithresh*) and the first threshold level is picked to binarize the image, so the background is equal to 0 and regions of interest (ROIs) with detected objects are equal to 1 (**Fig. 2.5D**).

The next steps will implement the watershed transform to segregate object close enough to be detected as a single object. First a Euclidean distance transform (*bwdist*) is performed on the binary image to compute a value for each pixel that represents the distance between every pixel and the closest nonzero pixel (**Fig. 2.5E**). Then the background, defined as the area outside of identified ROIs and has assigned values of zero by the binarization process, is removed by setting background values to negative infinity so it will be ignored by the watershed transform (**Fig. 2.5F**). Then a H-minima transform (*imhmin,* H = 1) is performed to remove all minima whose depth is less than H. This allows the tuning of watershed segmentation for either more (increasing H) or less (decreasing H) sensitivity in separating objects. It is highly recommended that at least H value of ≥ 1 is selected to avoid the over-segmentation of objects. The watershed transformation is then applied with the *watershed* function. This algorithm separates objects that are connected by utilizing the local minima that are produced by the distance transform and meet the specified H-minima requirement. The *watershed* function also labels the locations which each object occupies with a unique numerical value. The *regionprops* function is applied on the watershed-transformed image to determine the regions associated with the background. The background will present as an object with the largest area and the pixels representing the background are labeled with a '1'. The location of pixels making up the background is saved as a background mask and will be later applied to the 'green' protein channel to measure background intensities and used for field flatness correction. Then objects that are touching the border, either by the edge or corner (8-way connectivity), are removed using the *imclearborder* function (**Fig. 2.5H**). These objects are removed because they are considered partial objects with some parts cut off by the image border and not suitable for analysis. It is important that this object removal be performed after registering the background mask, or the background could include intensity data from this partial objects. The remaining objects are again binarized and then relabeled to prevent any missing labels, creating the final segmented object mask. This object mask can then be applied to the GUV membrane channel to obtain data including vesicle diameter and intensity, and to the protein channel to obtain the intensity of proteins encapsulated in individual vesicles. But prior to that the field flatness correction needs to be performed.

(Figure on next page)

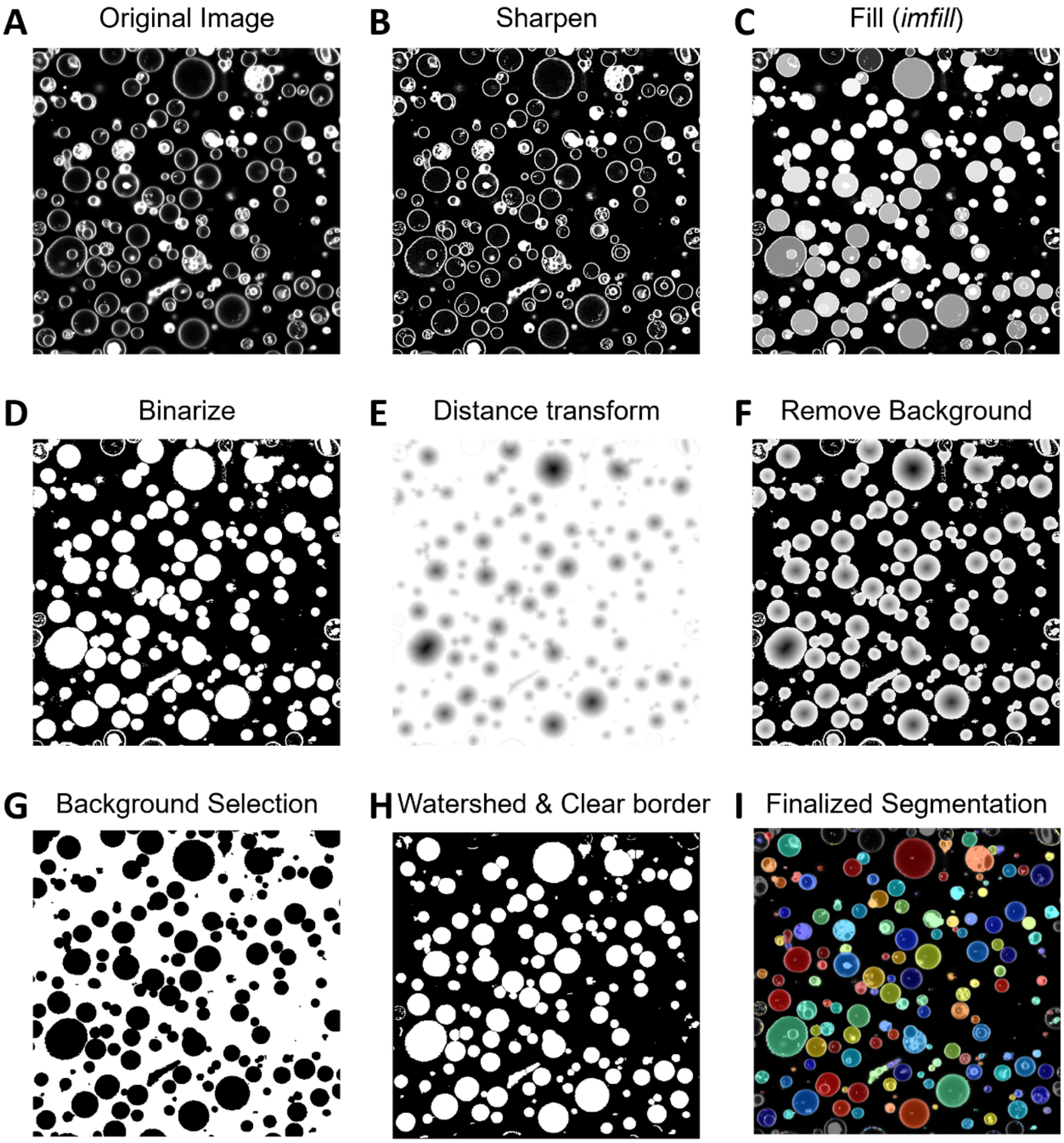

Fig. 2.5. Watershed segmentation of giant unilamellar vesicles and other objects from confocal microscope images. A) Original image showing lipid membranes from GUVs and other objects. **B)** Sharpening filter (*imsharpen*, radius = 5 SD, strength = 3) used to sharpen images and make the border of GUVs more pronounced. **C)** Image region identified as holes are flood filled (*imfill*) to form filled shapes. **D)** Image is binarized with a multilevel image threshold using Otsu's method to characterize detected objects as 1 (white) and background as 0 (black). **E)** Euclidean distance transform performed for watershed implementation. Black depth represents the distance to nearest nonzero pixel. **F)** Background (completely black) is removed to excluded from the watershed transform. **G)** Background mask (white) is selected and saved. **H)** After watershed implementation, partial objects connected to the border are excluded (*imclearborder*). I) Finalized segmentation image showing separate segmented objects randomly colored. Image size is 134.95×134.95 μm (1584×1584 pixels).

2.2.9.2 Field Flatness Correction

Although a Plan-Apochromat objective provides a good field flatness, there were still noticeable dimming of towards the edges of the images (**Fig. 2.6A**). To ensure that the measurements of intensities were accurate, a post-processing field flatness correction was performed. The background mask (**Fig. 2.6B**, red areas) is applied to the protein channel to obtain the background data without any objects included. The dark areas will be ignored as they are not a part of the background. Then the background data is fitted with a 2D polynomial surface fit (**Fig. 2.6C**) using Eq. 4:

$$f(x,y) = a_0 + a_1x + a_2y + a_3x^2 + a_4y^2 + a_5xy) \qquad \textbf{Eq. 4}$$

The maximum height (z_{max}) is obtained from the fitted surface and a correction factor is created by taking the z_{max} divided by the fitted surface $\left(\frac{z_{max}}{f(x,y)}\right)$. The correction factor is then multiplied to the original protein channel image data including the objects. This results in a flattened field as shown in **Fig. 2.6D** and ensures variation of intensity due to field flatness is minimized.

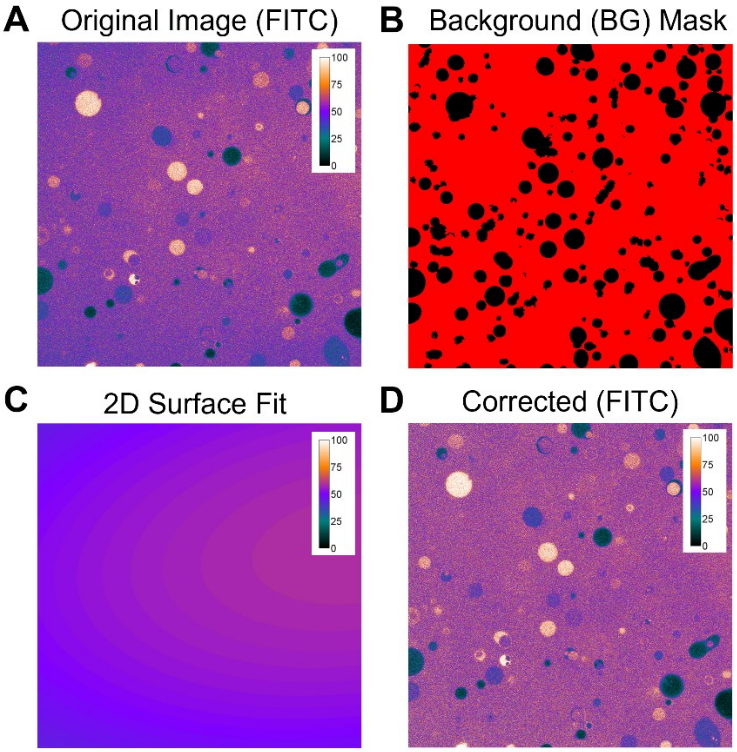

Fig. 2.6. 2D polynomial surface fitting for field flatness correction. A) The original image shows the intensity of the FITC channel before field flatness correction. B) The background mask shows the selection of the background (red), excluding any objects (black) in the image. C) The background data is fitted with a 2D polynomial surface ($f(x,y) = a_0 + a_1x + a_2y + a_3x^2 + a_4y^2 + a_5xy$), which is used to create a correction matrix. D) The corrected image shows an even field flatness, where the background intensity of the edges is now consistent with the center. A colormap is applied to accentuate differences in field flatness.

2.2.9.3 Selection using the coefficient of variation

The watershed segmentations provide data for all objects detected in the image, but it does not differentiate between different types of objects that may be in the sample (**Fig. 2.7A**). GUVs are of the target of interest but lipid aggregates, MLVs, and MVVs may also be present in the sample. To differentiate between these object types, a coefficient of variation (CV = SD/mean) based selection algorithm is used. In the GUV membrane channel (red), the large contrast between the bright fluorescent intensity (FI) in the membrane and dark FI in the lumen of GUVs will show a very large CV. In contrast an aggregate, MLV, or MVV will have a greater intensity in the interior of the object and result in a lower CV. The CV is calculated using the intensity of all pixels located within each object. Based off observation of the CV of images taken, it was determined a minimum CV of 0.75 would select for GUVs well while excluding other object types (**Fig. 2.7B**). For negative control samples, where no proteins are encapsulated into the vesicles, a CV selection is also performed on the protein channel to remove rare cases where they contain localized intensity in the lumen but are actually inverted lipid tails.

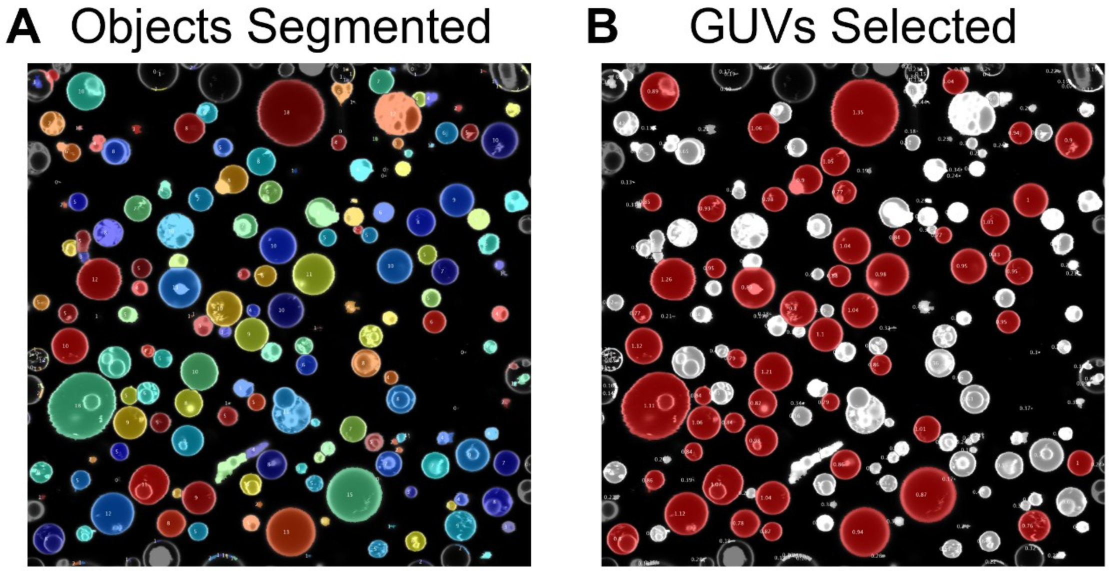

Fig. 2.7. Selection of giant unilamellar vesicles (GUVs) from segmented objects. A) All objects were indiscriminately detected using the watershed segmentation routine. B) A coefficient of variation (CV) based selection algorithm is used to select only GUVs (red highlighted). Other objects such as aggregates, multilamellar vesicles (MLVs), and multivesicular vesicles (MVVs) are excluded. A CV cutoff of 0.75 is used. Image size is 134.95×134.95 μm (1584×1584 pixels).

2.2.10 Imaging setup for characterization of diffusive loading

The imaging parameters are setup so intensities collected from GUVs only arise from the interior of the GUV lumen and do not include intensity from FITC-BSA present in the background around the GUVs. Images are taken with a high NA (1.4 NA) objective that can give us an image slicing thickness of 0.7 μm (**Fig. 2.8A**). The slicing thickness, or axial resolution, determines the axial range of the imaging plane in which light is collected. A slicing thickness of 0.7 μm will allow light to be collected from the interior of the vesicles. A 3 μm offset from the imaging surface is used so the imaging plane will be within the lumen of most vesicles. Only vesicles with diameters ≥3 μm are considered in the analysis because the 3 μm offset combined with the 0.7 μm thickness of the imaging plane will mean vesicles below 3 μm will not fully fall within the imaging plane (**Fig. 2.8A**). Additionally, intensity measurements across GUVs show that due to the curvature of the membrane and the diffraction limited resolution, intensity measurements close to the membrane can capture background intensity outside of the GUV (**Fig. 2.8B-C, ROI #1 & #3**). The curvature of the membrane near the edge can allow some portion of the background to be captured within the imaging voxel. The diffraction limited lateral resolution for the Zeiss LSM880 can be approximated with the Rayleigh's criterion (92, 93) in Eq. 5, where λ_{ex} is the excitation wavelength (nm) and NA is the numerical aperature of the objective.

$$R_{lateral} = 0.61\frac{\lambda_{ex}}{NA} \qquad \textbf{Eq. 5}$$

This gives us a diffraction limited lateral resolution of ~244 nm, or the smallest size of features that can be resolved for a λ_{ex} of 551 nm and NA of 1.4. The resolution displayed on the confocal microscope software shows 85 nm, which is notably different from the diffraction limited lateral resolution. This is because the Nyquist oversampling criteria (94, 95) has not yet been applied and does not reflect the more useful measure of diffraction limited resolution. To obtain the diffraction limited resolution from the displayed resolution on the microscope, a 2.5 times multiplier is needed to account for the Nyquist oversampling criteria. **Eq. 6** shows how the resolution of the microscope with 561 nm excitation wavelength and a 1.4 NA objective of 98 nm is calculated. Note this resolution for confocal images taken shows up as ~85 nm because it is optimized for the 488 nm excitation wavelength.

$$N_{lateral} = 0.61\frac{\lambda_{ex}}{2.5NA} \qquad \textbf{Eq. 6}$$

Because the thickness of the lipid membrane for a pure DOPC membrane is approximately ~5 nm (96–98), so the thickness of vesicle membranes are clearly much smaller than the diffraction limited lateral resolution. The actual membrane thickness is much smaller than appears in the images. So, intensities measurements close to the vesicle membrane likely capture some of the background outside the vesicle. These effects lead to the increase of intensity seen in **Fig. 2.8B-C** as the membrane is approached. To ensure the most accurate measurement of intensity, only the core intensity, defined in the image as the intensity from a concentric ROI with a diameter equal to 30% of the vesicle diameter, of the vesicle is measured

(**Fig. 2.8B-C**, ROI #2). The axial resolution can be obtained from **Eq. 7**, where the refractive index of the medium (η) needs to be considered. For these experiments using the 63× 1.4 NA objective, immersion oil is used as the medium, which has a refractive index of 1.51.

$$R_{axial} = \frac{1.77\lambda_{ex}\eta}{NA^2} \qquad \textbf{Eq. 7}$$

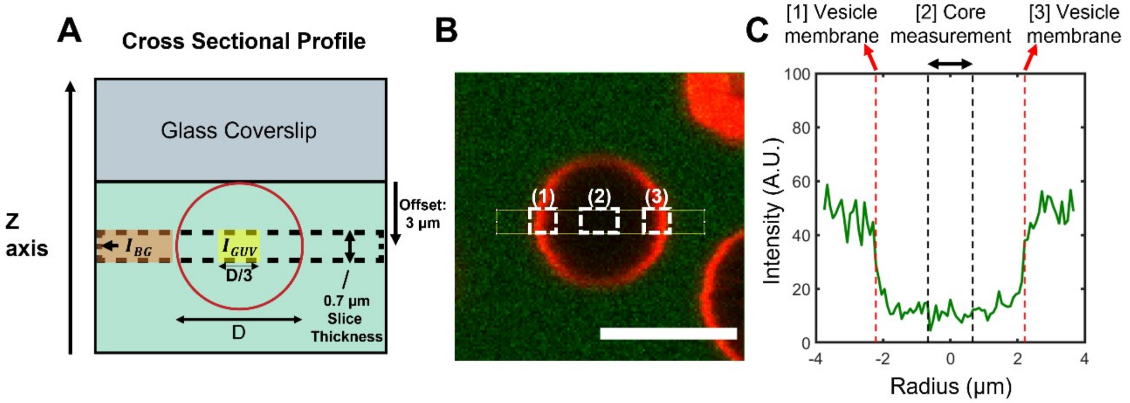

Fig. 2.8. Schematic of imaging setup for intensity measurements. (A) Cross sectional profile (frontal plane) showing glass and vesicle. An offset of 3 µm from the bottom surface of the glass coverslip is used for imaging. The slicing thickness is set to 0.7 µm, so only vesicles with diameters (D) ≥3 µm can be sufficiently captured in the imaging plane. Intensity is only measured from the core (I_{GUV}), with the imaging region defined as a cylinder (diameter = D/3, height = 0.7 µm). The background intensity is captured in areas devoid of vesicles (I_{BG}). **(B)** Top-down image (axial plane) showing a GUV (red) that has not be loaded with proteins (green). The background contains 1.75 µM of protein (green). Three regions of interest (ROIs) (white boxes) are labeled. Scale bar = 5 µm. **(C)** Intensity of proteins as a function of the distance from the center of the GUV (radius). Near the vesicle membranes [1 & 3] there is a spike in measured intensity. The core measurement [2] avoids these areas.

2.2.11 Preloading Variant with OSM-PAPYRUS

A separate set of methods was used for the preloading variant of OSM-PAPYRUS. Here, the same lipid film deposition procedures are followed as in **2.2.7**, except now the cargo loading step is performed first. First, 10 μL of a 15× FITC-BSA concentration (5.65 μM, 11.29 μM, and 22.58 μM FITC-BSA concentrations were used) is added directly to the lipid coated paper first and given 10 minutes to incubate. During this time, vesicle assembly is occuring because the FITC-BSA is dissolved in ultrapure water. After 10 minutes of incubation in a high concentration of FITC-BSA, a premixed solution of 15 μL of 1 M sucrose in 110 μL of ultrapure water is added directly to the sample. Immediately after this step, 15 μL of 10× PBS is added underneath the paper and allowed to diffuse into the vesicles for another 110 minutes, for a total preparation time of 120 minutes. **Table 2** shows the summary of the additions and incubations times for the preloading technique. The final concentration of FITC-BSA in the sample was 0.38 μM, 0.75 μM, and 1.50 μM. The same extraction technique as in **2.2.7** is used to extract vesicles off the surface of the paper.

In preparation for imaging, a similar custom PDMS chamber is used as in **2.2.8**, except a regular microscope slide is used instead of a functionalized coverslip, as no binding is required for this imaging configuration. Instead of streptavidin, 30 μL of 1 mg/mL of casein is added to the chamber so the glass surface will be passivated by the nonspecific binding of casein. After 30 minutes of incubation with the casein, the casein is rinsed out of the chamber with an excess flow of ultrapure water for approximately 2 seconds. The chamber is then dried using a steady stream of ultrapure nitrogen gas from a nitrogen gun. Then 5 μL of extracted vesicles are added to 55 μL of the sedimentation buffer with 1× PBS instead of 1× clock buffer. The chamber is then sealed with a 22 × 22 mm square coverslip and allowed to sediment for 2 hours before imaging.

Imaging is performed with a W Plan-Apochromat 20× 1.0 NA objective on the Zeiss LSM 880 confocal microscope. Two imaging channels are set up alternating every line. The 'red' vesicle membrane channel is setup to image rhodamine-PE lipids was configured with 2.5% power for the 561 nm diode-pumped solid-state (DPSS) laser and a detector gain of 700 A.U. for the confocal photomultiplier tube (PMT) detector. The 'green' protein channel is setup to image FITC-BSA was configured with 10% power for the 488 nm argon laser and a detector gain of 650 A.U. for the gallium arsenide phosphide (GaAsP) detector. The pinhole diameter is set to 1 A.U., corresponding to a 1.3 μm thick optimal section in the z-plane. Ten images were taken manually per sample, with the focus being manually adjusted so the majority of vesicles appeared in focus. Image resolution was set at 2692 × 2692 pixels with an image size of 320.5 × 320.5 μm. The imaging chamber is placed directly onto the microscope with no special adapters. Water is placed as the immersion medium on top of the imaging chamber prior to imaging.

This sample preparation and imaging setup described here is an older methodology and is superseded by the methods described in **2.2.7** to **2.2.10**. These methods reflect only the preloading variant data in **2.3.4** and should be used for reference only to those experiment sets.

Table 2. Additions and incubation times for the preloading variant of OSM-PAPYRUS

Step	Name	Concentration	Volume	Incubation Time
Cargo Preloading	FITC-BSA	15×	10 µL	10 min
Low Salt Assembly	Ultrapure water	--	110 µL	~0 min
	Sucrose	1000 mM	15 µL	
Diffusive Loading	PBS	10×	15 µL	110 min
End	Final Composition	100 mM Sucrose, 1× PBS, 1× FITC-BSA	Total: 150 µL	Total: 120 min

2.3 Results and Discussion

2.3.1 Deciphering encapsulation statistics from OSM-PAPYRUS

Vesicles assembled through the **o**ne-**s**tepped **m**odulated **p**aper-abetted **a**m**p**hiphile h**y**d**r**ation in aq**u**eous **s**olution (OSM-PAPYRUS) method follow a diffusive loading principle where the cargo to be encapsulated must diffuse into the pre-formed vesicle buds through their nanotube like tethers. An example image of GUVs assembled through OSM-PAPYRUS with FITC-BSA encapsulated is shown in **Fig. 2.9A**, where the intensity of the FITC-BSA (green) is seen to vary within the GUVs. Like most thin film hydration methods (1, 4, 5, 52), the size distributions of vesicles show a high degree of polydispersity, **Fig. 2.9** shows giant unilamellar vesicles (GUVs) produced with OSM-PAPYRUS, which show diameters ranging from approximately 3 – 35 µm. Smaller GUVs below 3 µm exists within the sample, however, the imaging setup precludes vesicles smaller than 3 µm (see **2.2.10** & **Fig. 2.8**). Due to the imaging setup taking images with an offset of 3 µm from the glass surface and a small slicing thickness of 0.7 µm, the sizes of GUVs shown in **Fig. 2.9B** tend to underestimate true GUV diameters. However, as true GUV diameters are not of sufficient concern for the purposes of the upcoming analysis of encapsulation efficiency and variation, adjustments to calculate for true GUV diameters are not performed. The diameter of GUVs given here still provides an adequate general estimate and differentiation of vesicle sizes. In **Fig. 2.9C**, diffusive loading of encapsulated concentrations of FITC-BSA shows a large variation of intensity within the population of vesicles. This suggests that the diffusive loading process of OSM-PAPYRUS produces non-uniform concentrations encapsulated within GUVs.

The background, or the areas that are not occupied with vesicles, contain a known concentration of protein equal to the loading concentration used to load the proteins. Measurement of the background intensity allows the determination of the fluorescent intensity expected inside a vesicle if it has captured the protein with 100% efficiency. If the intensity of the vesicle is divided by this background intensity, a measure of relative encapsulation efficiency (EE$_{rel}$) can be obtained. In **Fig. 2.9D**, the EE$_{rel}$ shows that the largest peak centers around a value of ~1.0 EE$_{rel}$, or 100% efficiency. However, there is also a smaller peak, suggesting a bimodal distribution with one distribution containing significantly lower EE$_{rel}$. Because a population of empty vesicles can be seen in **Fig. 2.9A**, a likely hypothesis is that these belong to population of empty vesicles.

To confirm the hypothesis of the existence of two populations, one empty and another filled, negative controls where no protein was loaded into the vesicles but still present in the background were performed. Two distinct populations could be seen in the intensity histograms of the positive control experiments, one with a peak in a distinct lower intensity compared to the dominant peak (**Fig. 2.10A**). The lower population corresponded with the expected distribution of the empty vesicles from the negative control samples (**Fig. 2.10B**). Empty vesicles are excluded using the *findpeaks* function on the intensity histogram line plots smoothed with a 3-point window moving mean filter to find the peak location and other peak parameters of the empty vesicle population. The peak location plus the full width at half height (FWHH) of the negative control is calculated to find the intensity cutoff criteria for empty vesicles. Empty vesicles likely arise from either spontaneous detachment of vesicles prior to loading or during loading due to the addition of salts or protein which can add shear forces to the system.

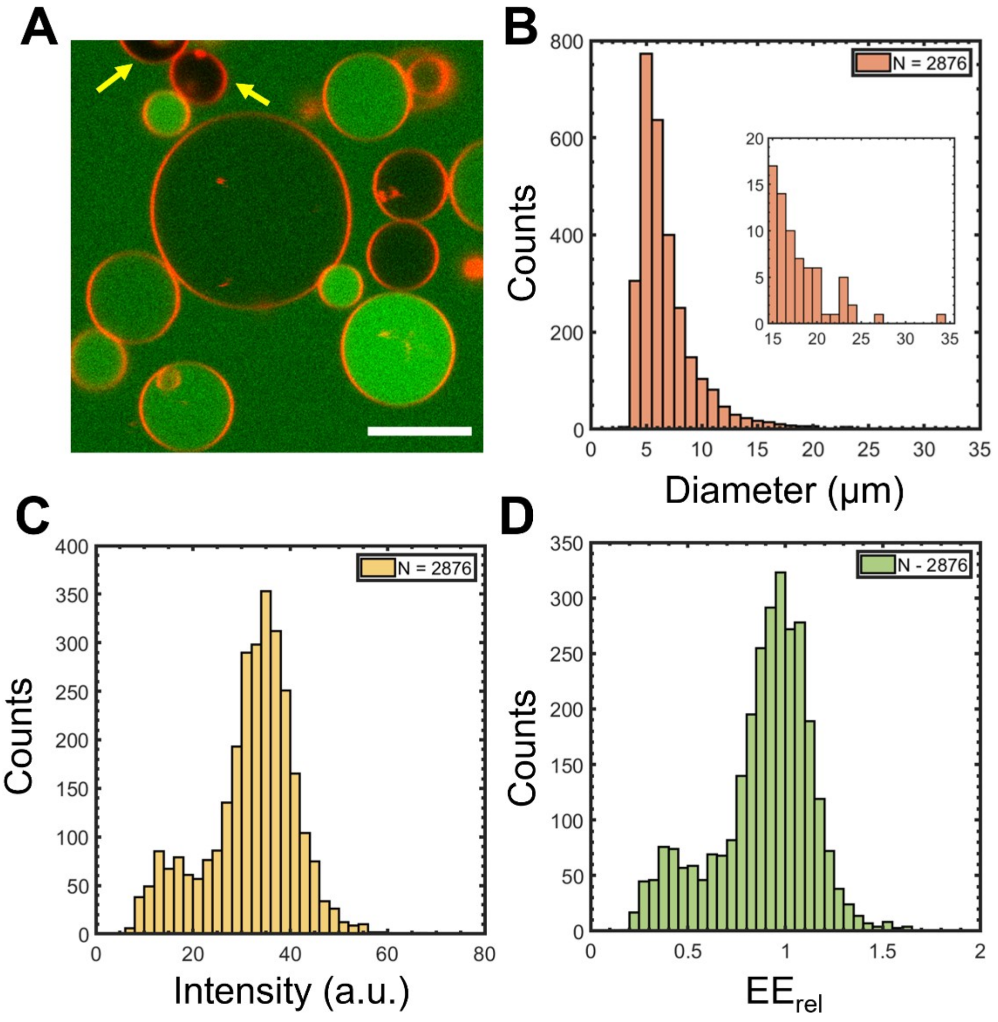

Fig. 2.9. Encapsulation in GUVs with OSM-PAPYRUS. A) 0.88 μM FITC-BSA (green) encapsulated into GUVs (red) show a varying concentration of encapsulated FITC-BSA indicated by varying intensities in vesicles. Yellow arrows point to empty vesicles. Image is taken using a 63× 1.4 NA objective. C) Histogram showing size distribution of GUVs in sample after all post processing steps are performed. B) Histogram showing intensity of encapsulated FITC-BSA (0.88 μM) in the population. D) Histogram of the relative encapsulation efficiency (EE_{rel}), defined as the encapsulated intensity divided by the background intensity. A population size of N = 2876 vesicles was used for this analysis. The scale bars are 10 micrometers.

To characterize the encapsulation of the model protein from the diffusive loading process (**Fig. 2.2**), a series of experiments with varying loading concentrations of FITC-BSA of 0.88, 1.75, 2.63, and 4.5 μM was performed. For each loading concentration, three independent repeats were performed. Negative controls were also performed for each concentration to determine empty vesicles. The percentage of empty vesicles was determined for every independent repeat across the varying loading concentrations in **Fig. 2.10C**. Here, an analysis of variance (ANOVA) significance test was performed to determine if concentration influenced the number of empty vesicles. It was determined from the ANOVA test that there are no significant differences in empty vesicle percentages when concentration is varied [$F(3,8) = 0.46, p = 0.72$]. The full details of the ANOVA test results are available in **Appendix A.1**. The fraction of empty vesicles is consistent with the earlier hypothesis that vesicles can detach prematurely, likely from shear forces introduced to the system when adding salts and proteins. On average, ~20% of vesicles were found to be empty.

Detailed analysis of empty vesicles in **Fig. 2.11A** from the negative controls showed rare higher intensity cases (**Fig. 2.11B)**. What this likely shows is some vesicles have formed interior or inversed tubes/tails, in which the vesicles themselves remain self-contained, but since the tubes have formed into the vesicle interior, the background can be seen within these inversed tubes. The presence of streptavidin-biotin binding could be one reason these tubes are exhibited, as affixation of a part of the membrane to the glass may have some unknown effects on the membrane behavior. An additional CV selection routine on the FITC-BSA channel will exclude these rare cases from the analysis. It may be possible to reduce or eliminate these cases if the vesicles are made to be slightly hypertonic, which can suppress the formation of tails or tubes. Tails are more likely with hypotonic conditions as excessive membrane area can be created due to water diffusing out of the vesicle lumen.

(Figure on next page)

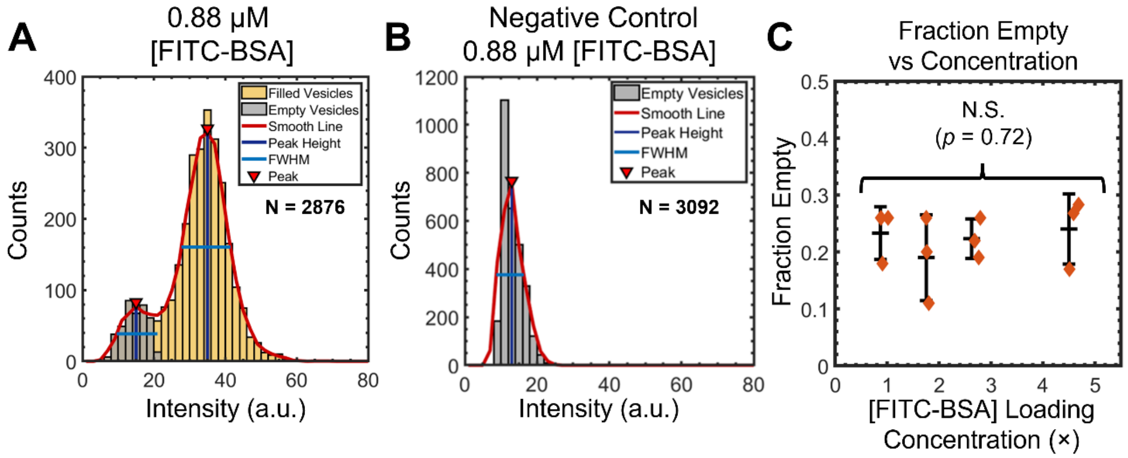

Fig. 2.10. Two distinct distributions for FITC-BSA in vesicles. (A) Histogram of intensities inside vesicles for 0.88 µM FITC-BSA (N = 2876 vesicles), the distribution of non-empty vesicles (yellow) and empty vesicles (gray). The percentages of empty vesicles (EV%) are shown. Peak fitting is performed to find the two peak locations and the full width at half maximum (FWHM) corresponding to filled and empty vesicles. **(B)** Negative control sample with no FITC-BSA encapsulated but with 0.88 µM FITC-BSA in the background shows the expected intensity distribution of empty vesicles. **(C)** The fraction of empty vesicles is plotted against the FITC-BSA loading concentration. An analysis of variance (ANOVA) test was performed [$F(3,8) = 0.46$, $p = 0.72$] showing no fraction empty does not vary with loading concentration.

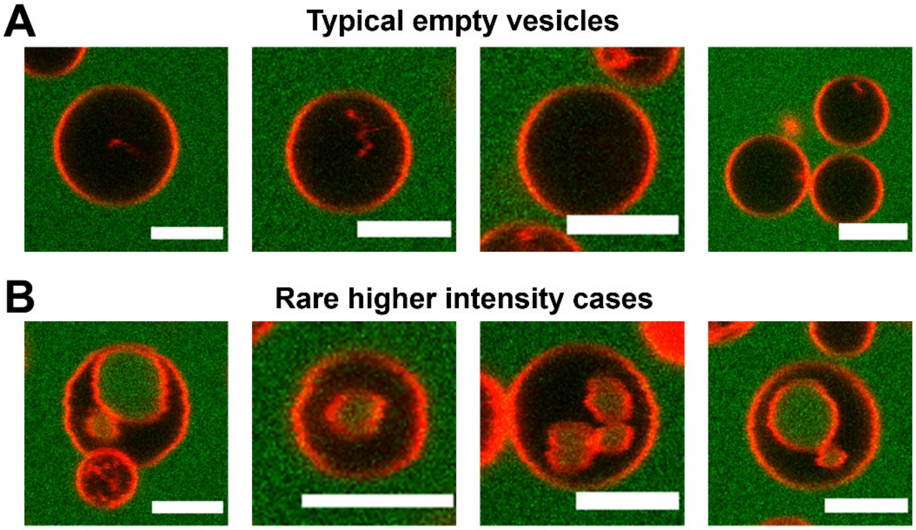

Fig. 2.11. Negative control vesicles can show rare higher intensity cases. A) Typical empty vesicles in the negative control, with no FITC-BSA (green) in the interior of the vesicle (red). B) Rare cases where even though the vesicle is empty, suspected inverted tubes can cause the appearance of higher intensity. These can be filtered out by using a CV selection on the FITC-BSA channel.

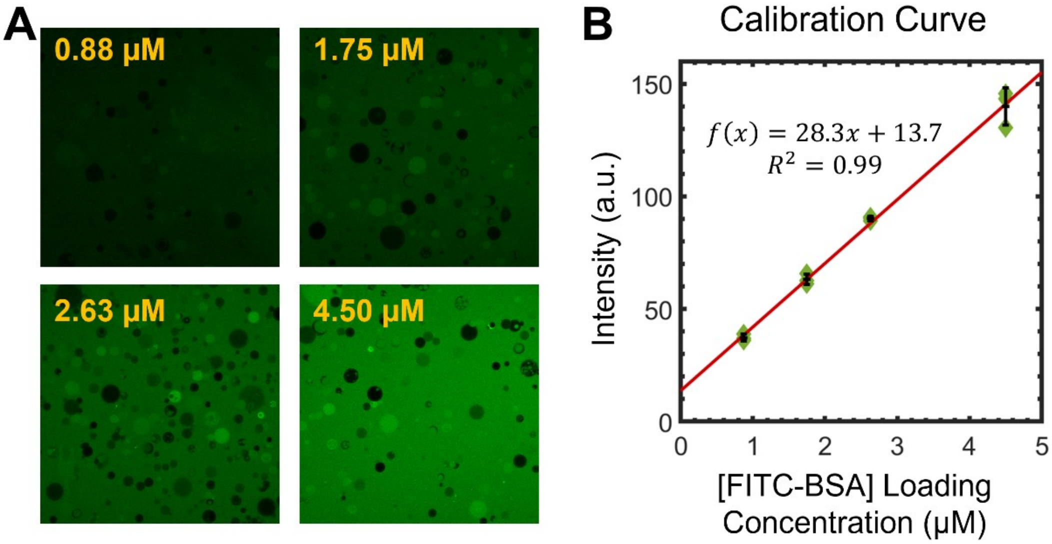

Fig. 2.12. Calibration curve and protein distribution. (A) Calibration curve relating the measured intensity to the concentration of FITC-BSA. **(B)** Encapsulated FITC-BSA in GUVs can be adequately described as a gamma distribution (purple line). The mean and coefficient of variation (CV) calculated from the gamma fit values (k, θ) are displayed. The histogram represents data from an average of 3 independent repeats with a loading concentration of 1.75 µM FITC-BSA.

To better compare and represent the encapsulation data, the intensity is converted into concentration values. The protein intensity value obtained from the background corresponds to a known protein concentration, so the background intensity (**Fig. 2.12A**) was used to create a calibration curve to convert intensity into concentration. Example images of the FITC-BSA channel (green) show the background intensity changes as a function of protein loading concentration. Although the area where vesicles are located is still shown, the processing to determine background intensity will ignore regions where objects are present. The intensity showed a linear relationship with concentration ($y = 30.2x + 10.6, R^2 = 0.996$) in **Fig. 2.12B**. The intensity inside the vesicles then can be converted into protein concentration using the calibration curve.

To show the variation in encapsulated proteins were not simply due to the polydisperse vesicle sizes, we evaluated the encapsulated FITC-BSA concentrations as a function of vesicle diameter. In **Fig. 2.13** encapsulated FITC-BSA concentrations with a loading concentration of 1.75 µM is plotted against vesicle diameters, shown with a violin plot for each diameter size class. The distribution of FITC-BSA appeared to be highly consistent across vesicle sizes. A Kruskal-Wallis (KW) ANOVA test was performed due to the non-normality and unequal sample sizes. The test showed encapsulated concentrations is independent to the vesicle diameter [$X^2(6, 617) = 2.01$, $p = 0.92$]. The full details of the KW-ANOVA test results are avaliable in **Appendix A.2**. This concludes that the variation of encapsulated proteins is not due to the polydisperse vesicle sizes, instead the variation appears to be an inherent property of OSM-PAPYRUS.

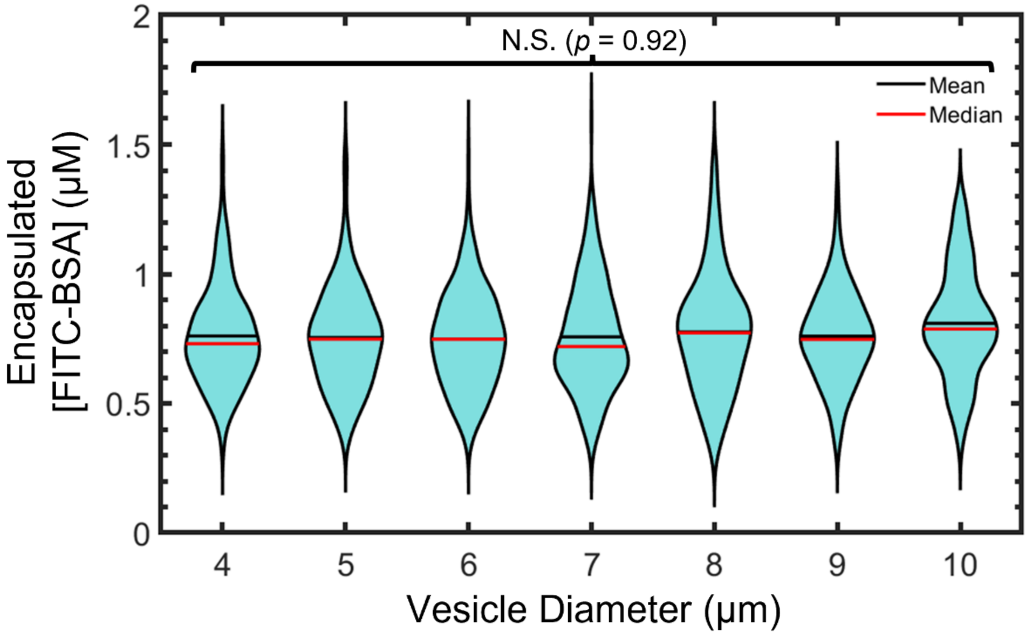

Fig. 2.13. Encapsulated protein does not vary with vesicle diameter. Distributions of encapsulated protein concentrations in vesicles are shown as a function of vesicle diameter using violin plots. Vesicles diameters were binned so each integer value includes vesicles with diameters ±0.5 µm to the integer value. An Kruskal-Wallis (KW) ANOVA test shows encapsulated concentrations is not significantly affected by vesicle diameter [$X^2(6, 617) = 2.01$, $p = 0.92$]. Data here represents a loading concentration of 1.75 µM FITC-BSA. Mean (black line) and median (red line) are shown on each violin plot.

2.3.2 Cell-like variability of encapsulated proteins

A gamma distribution (k, θ) (**Eq. 8**) describes the distribution of encapsulated proteins in a population of vesicles (**Fig. 2.14**) across a range of protein concentration (0.88 – 4.5 μM).

$$f(x) = \frac{1}{(k-1)!\,\theta^k} x^{k-1} e^{-\frac{x}{\theta}} \qquad \textbf{Eq. 8}$$

The mean, the standard deviation (SD), and the coefficient of variation (CV) from the fitted parameters is calculated, for gamma distributions the mean is $\mu = k\theta$, the standard deviation is $SD = \sqrt{k\theta^2}$, and the coefficient of variation is SD/μ. Gamma distributions are often used to describe the distribution of protein concentrations in biological cells (80–83). The mean CV of the encapsulated proteins produced with OSM-PAPYRUS was approximately ~0.3, which closely mimics the measured variation seen in biological cells (84, 85). This shows that the diffusive loading from the OSM-PAPYRUS technique is able to mimic both the distribution of protein concentrations and the magnitude of variation from biological cells, thus able to reproduce cell-like variation. In this case the mechanisms from which the variation arises is expected to be different, where variation of protein concentration in cells arise primarily from partitioning of low molecular number species, stochastic expression, or other noisy cell processes (64, 65, 83, 99–102). In this case, the origin of the variation is different as no gene expression is occuring, instead the variation likely arises due to the diffusive loading or other aspects of the OSM-PAPYRUS technique. A log-likelihood ratio test (LRT) against a normal distribution is performed for each distribution. In the LRT the log-likelihood of a gamma distribution is subtracted from log-likelihood of a normal distribution. A positive value suggests the gamma distribution is a better fit than the normal distribution.

Partitioning variation can still be applicable to this system, however the FITC-BSA molecular copy numbers are sufficiently high even for the smallest vesicle sizes that partitioning variation based on Poisson statistics is not significant. A quick calculation using **Eq. 3** can show us the CV expected for a given concentration and given vesicle size in **Table 3**. The molecular copy numbers even for the lowest tested concentraiton and vesicle size is still significantly high, in the order of 10^3 molecules. If solely based on Poisson partitioning statistics, then the conditions based on protein concentrations and vesicle sizes only suggest a maximum CV of 1.2%, much lower than coefficient of variation of ~30% exhibited by the vesicle populations. This means for OSM-PAPYRUS, the variation exhibited is not strictly due to partitioning effects, and instead must come from other aspects of the assembly and diffusive loading process. The key advantages to this greater-than-partitioning variability, is that proteins species commonly in the μM concentration range are encapsulated in a distribution similar to how they would appear with in a cell that has expressed them, which opens up the possibility of directly encapsulating protein-based cellular systems and studying the effect of intercellular variation.

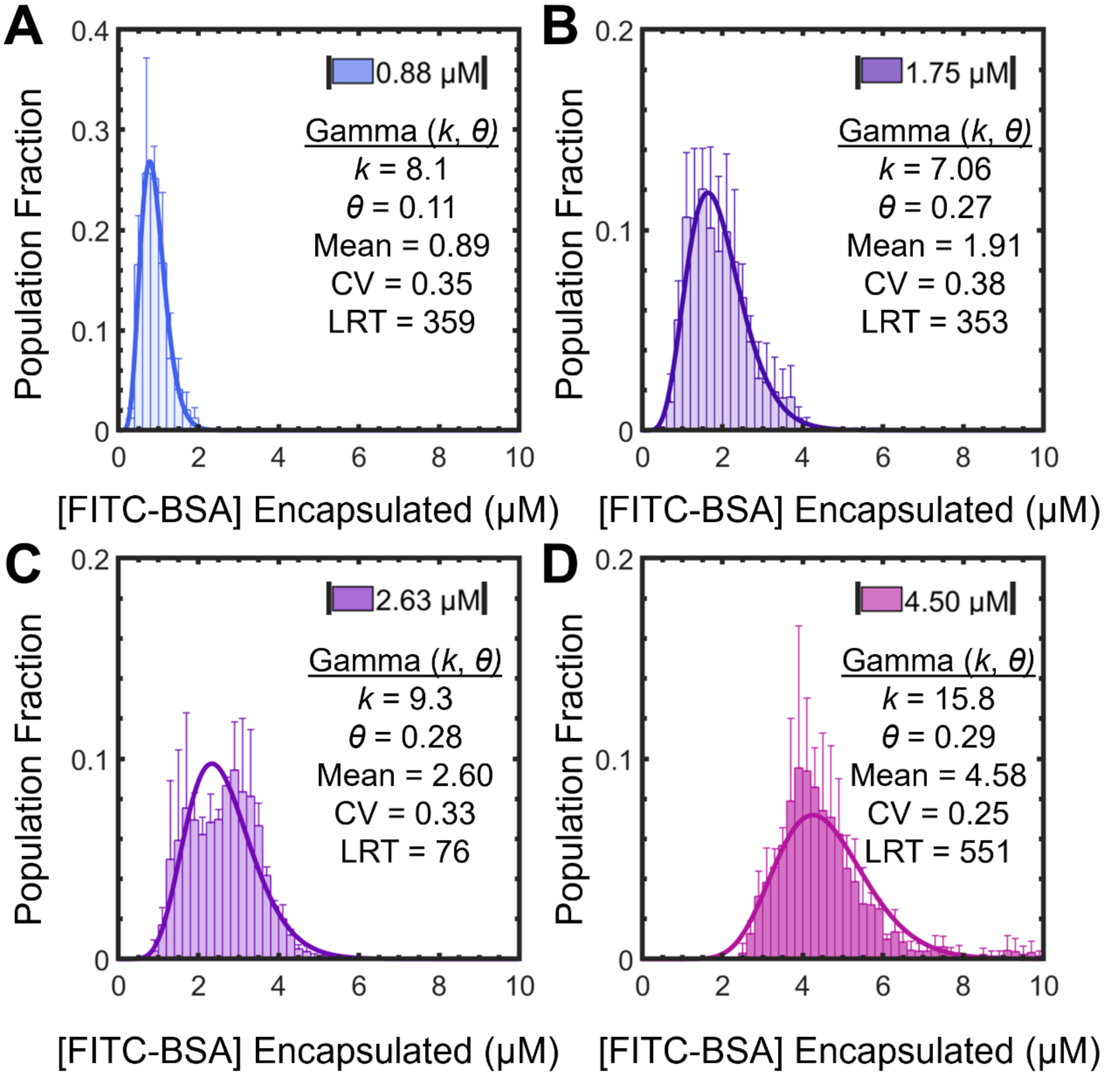

Fig. 2.14. Gamma distribution describes the distribution of encapsulated proteins. Distributions of protein encapsulated in vesicles from OSM-PAPYRUS are shown when loading concentration varies from **(A)** 0.88 μM, **(B)** 1.75 μM, **(C)** 2.63 μM, and **(D)** 4.50 μM FITC-BSA. Each histogram shows an averaged distribution from three independent repeats. The error bars indicate the standard deviation at each concentration bin (bin width = 0.2 μM). A gamma distribution has been fitted for each histogram (thick colored lines). Gamma distribution parameters (k, θ) are included in the figure along with the mean and CV calculated from the fitted parameters. Each independent repeat had an average of N = 1300 vesicles.

Table 3. Copy numbers and expected variation based on Poisson partitioning statistics.

Diameter (μm)	Volume (L)	FITC-BSA Concentration 0.88 μM	 1.75 μM	 2.63 μM	 4.5 μM
3	1.4×10^{-14}	7.5×10^{3} (CV = 1.2%)	1.5×10^{4} (CV = 0.8%)	2.2×10^{4} (CV = 0.7%)	3.8×10^{4} (CV = 0.5%)
4	3.4×10^{-14}	1.8×10^{4} (CV = 0.8%)	3.5×10^{4} (CV = 0.5%)	5.3×10^{4} (CV = 0.4%)	9.1×10^{4} (CV = 0.3%)
6	1.1×10^{-13}	6.0×10^{4} (CV = 0.4%)	1.2×10^{5} (CV = 0.3%)	1.8×10^{5} (CV = 0.2%)	3.1×10^{5} (CV = 0.2%)
8	2.7×10^{-13}	1.4×10^{5} (CV = 0.3%)	2.8×10^{5} (CV = 0.2%)	4.2×10^{5} (CV = 0.2%)	7.3×10^{5} (CV = 0.1%)
10	5.2×10^{-13}	2.8×10^{5} (CV = 0.2%)	5.5×10^{5} (CV = 0.1%)	8.3×10^{5} (CV = 0.1%)	1.4×10^{6} (CV = 0.1%)

2.3.3 Encapsulation efficiency and the consistency of variation

Before the OSM-PAPYRUS technique is to be used for studying cellular systems, a better understanding of the encapsulation statistics is important to decipher. In **Fig. 2.15A**, the mean encapsulated FITC-BSA concentration in a population of filled vesicles is plotted against the FITC-BSA loading concentration, with three independent repeats performed for each loading concentration (0.88, 1.75, 2.63, 4.50 μM). A linear regression ($f(x) = x, R^2 = 0.95$) is fitted, showing that the mean encapsulated concentration had a 1:1 correlation to the loading concentration. This suggests that although there is a large degree of variation (CV = ~0.3), the mean encapsulated concentration centers around an encapsulation efficiency of 100%. This is an interesting finding, in that whatever protein concentration is used to load the vesicles, the mean of the distribution will be at the loading concentration. This will make it easier to determine the distribution of concentrations that are expected to be encapsulated into vesicles when encapsulating components of cellular systems to study.

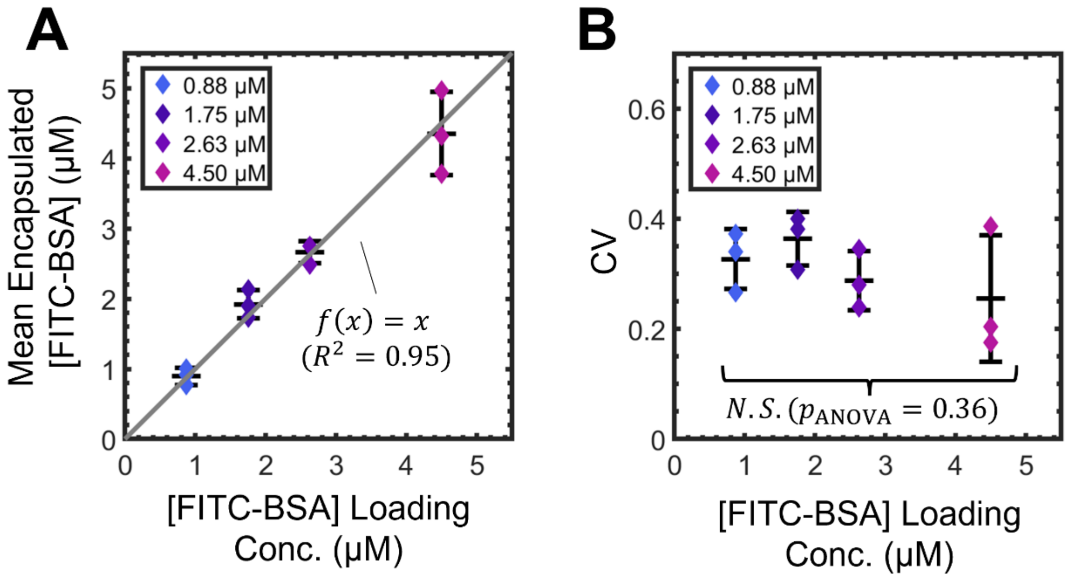

Fig. 2.15. Mean encapsulation efficiency and variation as a function of concentration. A) The mean encapsulated concentration of FITC-BSA within populations of vesicles as a function of loading concentration (0.88 – 4.50 μM) fitted with a linear regression ($f(x) = x, R^2 = 0.95$). B) Coefficient of variation (CV) as a function of loading concentration. An ANOVA test is performed which shows no significant differences (N.S.) in CV between varying loading concentrations. Error bars show ±1 standard deviation. The middle black bar shows the mean value of the three independent repeats per concentration.

Next, the variation is plotted against the FITC-BSA loading concentration in **Fig. 2.15B**, here the CV does not appear to have any clear trends when loading concentration is varied. There is some variation in the CV, however the CV of one concentration overlaps with the others. To statistically determine whether the differences in variation were significant, an ANOVA test was performed. The ANOVA test showed that the CV does not change according to the loading concentration [F(3,8) = 1.24, p = 0.36]. The full details of the ANOVA test results are avaliable in **Appendix A.1**. So, these results suggest that the encapsulation of proteins into vesicles with OSM-PAPYRUS can be described as having a mean equal to the loading concentration and a consistent variation across loading concentrations. This means the expected encapsulation of proteins from cellular components can be well characterized, as the expected distribution is a gamma distribution, and of which its parameters (k, θ) can be adequately described by known values of the mean and variation. This can be done by using the relationships of the gamma parameters, where the mean is $\mu = k\theta$, the standard deviation is $SD = \sqrt{k\theta^2}$, and so the $CV = \frac{\sqrt{k\theta^2}}{\mu}$. These relationships to the mean and CV allow k to be described as **Eq. 9** and θ to be described as **Eq. 10**. So even if the encapsulation distribution of a protein species is not directly measured, it would be possible to estimate the expected distribution based on these statistics. This would particularly be of use in many cell-free systems when fluorescently tagging every species would be difficult.

$$k = \frac{1}{CV^2} \qquad \textbf{Eq. 9}$$

$$\theta = \mu CV^2 \qquad \textbf{Eq. 10}$$

2.3.4 Preloading variant of OSM-PAPYRUS generates no empty vesicles

The preloading variant of the OSM-PAPYRUS technique forgoes diffusive loading of intended cargo, such as FITC-BSA, and instead introduces the cargo at an elevated concentration and reduced volume during the inital hydration step. The sucrose is added to dilute the high concentration of the protein towards the targeted final concentration, and then the high salt is added. The preloading variant ensures proteins can be encapsulated in the vesicle during the hydration step where assembly of vesicle occurs, similar to typical thin-film hydration methods. Then instead of diffusive loading into these vesicles, when sucrose and salts are added it dilutes the protein concentration and diffusive unloading occurs instead. In **Fig. 2.16A-C** images of vesicles (red) encapsulating FITC-BSA (green) show no sign of empty vesicles, as all vesicles appear to be filled. Instead, there are instances of hyper-encapsulation (**Fig. 2.16A-C**, white arrows) occuring where vesicles exhibit extremely high intensities. The hyper-encapsulation likely arises from vesicles becoming detached during the addition of sucrose and high salt buffers, similarly to the empty vesicle reported in the diffusive loading variate of OSM-PAPYRUS. The elimination of empty vesicles is the main advantage of the preloading variant, but the main disadvantage is that the cargo must be exposed to low ionic conditions. This exposure could denature or otherwise affect the functionality of sensitive proteins, such as the cyanobacteria clock proteins as discussed in the next chapter. For non-sensitive proteins or other cargo, the preloading variant may present as the better option as no additional steps are necessary to remove empty vesicles from the analysis.

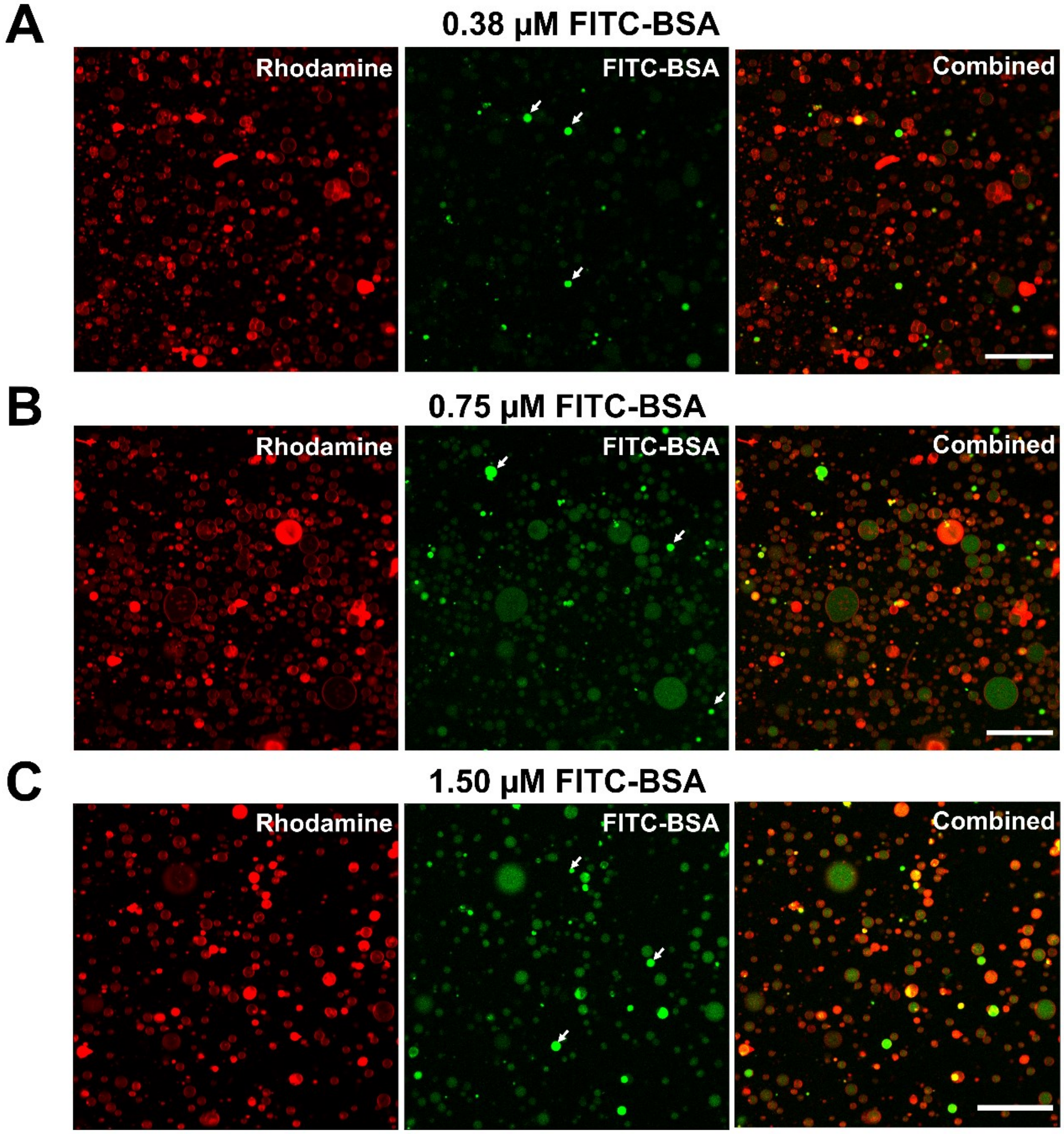

Fig. 2.16. Preloading does not generate empty vesicles. The preloading variant of OSM-PAPYRUS technique show encapsulation of FITC-BSA (green) does not generate empty vesicles for final concentrations of **(A)** 0.38 µM, **(B)** 0.75 µM, and **(C)** 1.50 µM FITC-BSA. White arrows point to cases of high encapsulation, where FITC-BSA concentrations are significantly higher. Images are taken with 20× 1.0 NA objectives. Scale bar = 50 µm.

In **Fig. 2.17**, histograms showing the encapsulated intensity distribution within vesicles with diameters 6 ± 0.5 μm encapsulated with final FITC-BSA concentration of 0.38 μM, 0.75 μM, and 1.50 μM. Only vesicles from same diameter size class are used for comparison here as the imaging configuration could mean each voxel captured by the confocal microscope will contain a different volume based on vesicles diameter. So larger vesicles can contain a higher intensity than a smaller vesicle, even if the concentration is the same in these experiments. Analysis of a single diameter size class will allow direct comparison without having to worry about size related effects. **Fig. 2.17** shows there is variation in the encapsulated concentration of protein seen even when using the preloading technique. This suggests variation also occurs from the diffusive unloading of the preloaded proteins or that the variation may come from another shared process all together.

The intensity histogram on the right (**Fig. 2.17**, right) shows the presence of rare high encapsulation vesicles (HEVs), defined as vesicles with more than three times the median intensity. The median intensity is used to characterize HEVs because mean intensities will be biased towards the significantly higher intensity of HEVs, which in some cases have >30× the median intensity of the population. The measured intensity of HEVs could be slightly underestimated in some cases because in some HEVs the intensity is overexposed due to significantly greater concentrations of protein encapsulated.

A gamma distribution describes vesicles well in **Fig. 2.17** with HEVs excluded. Just as with empty vesicles, HEVs arise from a separate process when buds detach early. Table 4 shows the summary statistics of the distributions for 0.38 μM, 0.75 μM, and 1.50 μM FITC-BSA concentrations. The coefficient of variation (CV) of the intensity distribution including the HEVs were extremely high, ranging from a CV of 65 % to 166 %. This large CV is not surprising given the presence of HEVs with up to 30× the median intensity would greatly distort standard deviation measurements.

With the HEVs removed, Table 4 show the CV values ranges from 30 – 33%, which matches the expected CV from the diffusive loading variant of OSM-PAPYRUS. This suggests that both the preloading and diffusive loading variant of OSM-PAPYRUS is capable of producing cell-like variation, when excluding vesicles that are prematurely detached. This shows promise in the adaptability and application of the OSM-PAPYRUS technique for the study of cellular systems. If the cellular systems contain sensitive components that require specific buffer conditions, the diffusive loading variant may be optimal. But otherwise, if empty vesicles are less acceptable, preloading variant of the technique can be used with similar results in mimicking intercellular variation.

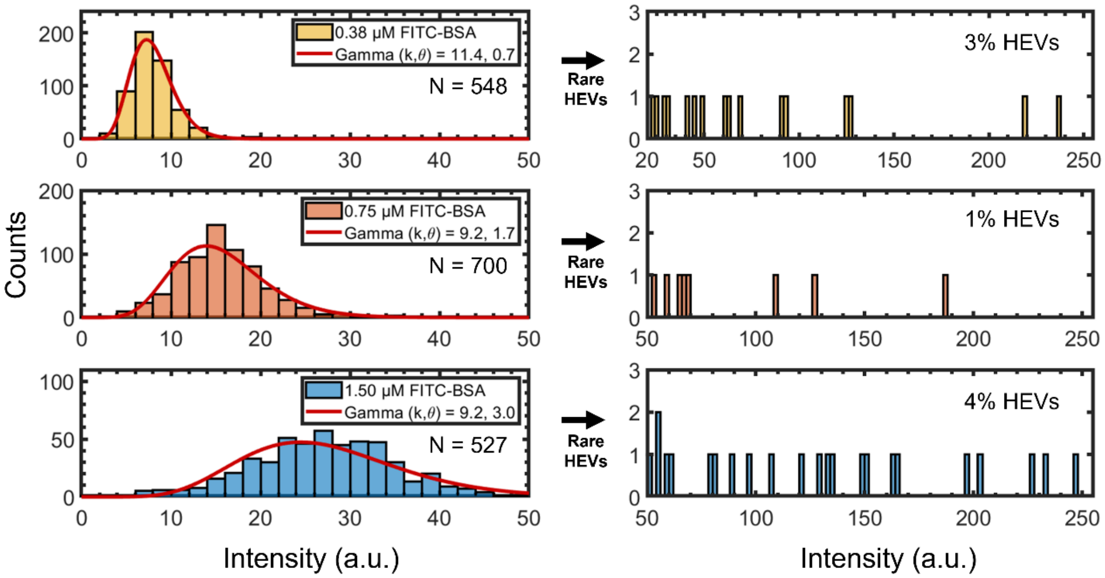

Fig. 2.17. Encapsulated FITC-BSA distribution in preloaded vesicles. Histograms show the distribution of encapsulated FITC-BSA for 0.38, 0.75 and 1.50 μM concentrations. (Left) Distribution of FITC-BSA in vesicles with (right) rare hyper-encapsulated vesicles (HEV). HEVs are defined as those with intensities ≥ (3 × median). Data composed from vesicles with diameters 6 ± 0.5 μm. Gamma distribution fitted to the distributions excluding HEVs.

Table 4. Comparison of encapsulation data with and without hyper-encapsulated vesicles (HEV).

Concentration (μM)	Median Intensity (a.u.)	HEV Cutoff (3 × median)	CV (w/ HEVs)	CV (w/o HEVs)
0.38	7.7	23	166 %	30 %
0.75	15.4	46	65 %	33 %
1.50	27.6	83	82 %	33 %

2.4 Conclusions

This chapter covered the methodology and built up the framework to be able to quantitatively characterize the variation in the encapsulation of macromolecules using the OSM-PAPYRUS technique. It was found through the encapsulation of a model fluorescently labeled protein, FITC-BSA, that the variation in protein concentrations within a population of vesicles followed a gamma distribution matching the distribution of proteins in biological cells and distribution of proteins had a coefficient of variation (CV = ~0.3) similar to cellular levels. The OSM-PAPYRUS method further allows formation in high ionic salt conditions that are commonly required for the optimal function of cellular systems and allows a gentle encapsulation of the protein cargo. This method is contamination free, as the cellulose paper substrate is not soluble in water. The cell-like variation and the gamma distribution remain constant across varying protein concentrations. While there are some empty vesicles produced, likely from the shear forces introduced from the addition of protein, the fraction that is empty do not vary with protein concentrations and can be detected and removed from the analysis. If empty vesicles must be taken out of the equation, a preloading variant of OSM-PAPYRUS can produce a similar gamma distribution with cell-like variation. However, this would require exposing the cargo to a low-ionic salt solution for a short period of time and would instead produce hyper-encapsulated vesicles. This suggests that the OSM-PAPYRUS technique is well suited to mimicking the cellular variation of proteins seen in cells and the variation can be well characterized and understood. This highlights the potential in creating minimal cell models for in vitro experimentation with the OSM-PAPYRUS technique. This minimal cell model will be able to incorporate cell-free systems into cell-sized vessels, in order to study how the system behaviors when there is a variation in component proteins and the presence of a lipid bilayer membrane that acts as a surface for membrane interactions. Unlike droplet partitioning methods, which can only produce cell-like variation for components with very low molecular copy numbers, this method shows cell-like variation can be mimicked even for high molecular copy numbers. In the next chapter, a circadian clock system from cyanobacterial will be encapsulated into vesicles assembled and loaded with OSM-PAPYRUS and the behavior of the clock in those vesicles will be compared with the clock behavior in bulk in vitro experiments. This will demonstrate the applications for the technique and what knowledge can be gained from studying a cellular system in vesicles with cell-like variation.

2.5 Bibliography

1. A. Cooper, V. Girish, A. B. Subramaniam, Osmotic Pressure Enables High-Yield Assembly of Giant Vesicles in Solutions of Physiological Ionic Strengths. *Langmuir* **39**, 5579–5590 (2023).
2. J. Pazzi, A. B. Subramaniam, Nanoscale Curvature Promotes High Yield Spontaneous Formation of Cell-Mimetic Giant Vesicles on Nanocellulose Paper. *ACS Appl. Mater. Interfaces* **12**, 56549–56561 (2020).
3. V. Girish, J. Pazzi, A. Li, A. B. Subramaniam, Fabrics of Diverse Chemistries Promote the Formation of Giant Vesicles from Phospholipids and Amphiphilic Block Copolymers. *Langmuir* **35**, 9264–9273 (2019).
4. J. Pazzi, M. Xu, A. B. Subramaniam, Size Distributions and Yields of Giant Vesicles Assembled on Cellulose Papers and Cotton Fabric. *Langmuir* **35**, 7798–7804 (2018).
5. A. Li, J. Pazzi, M. Xu, A. B. Subramaniam, Cellulose Abetted Assembly and Temporally Decoupled Loading of Cargo into Vesicles Synthesized from Functionally Diverse Lamellar Phase Forming Amphiphiles. *Biomacromolecules* **19**, 849–859 (2018).
6. K. M. Kresse, M. Xu, J. Pazzi, M. García-Ojeda, A. B. Subramaniam, Novel Application of Cellulose Paper As a Platform for the Macromolecular Self-Assembly of Biomimetic Giant Liposomes. *ACS Appl. Mater. Interfaces* **8**, 32102–32107 (2016).
7. P. Walde, K. Cosentino, H. Engel, P. Stano, Giant Vesicles: Preparations and Applications. *ChemBioChem* **11**, 848–865 (2010).
8. A. Weinberger, *et al.*, Gel-assisted formation of giant unilamellar vesicles. *Biophys. J.* **105**, 154–164 (2013).
9. D. J. Estes, M. Mayer, Electroformation of giant liposomes from spin-coated films of lipids. *Colloids Surfaces B Biointerfaces* **42**, 115–123 (2005).
10. P. A. Monnard, D. W. Deamer, Preparation of Vesicles from Nonphospholipid Amphiphiles. *Methods Enzymol.* **372**, 133–151 (2003).
11. K. Morigaki, P. Walde, Fatty acid vesicles. *Curr. Opin. Colloid Interface Sci.* **12**, 75–80 (2007).
12. B. M. Discher, *et al.*, Polymersomes: Tough vesicles made from diblock copolymers. *Science.* **284**, 1143–1146 (1999).
13. A. C. Greene, D. Y. Sasaki, G. D. Bachand, Forming giant-sized polymersomes using gel-assisted rehydration. *J. Vis. Exp.*, e54051 (2016).
14. J. R. Howse, *et al.*, Templated formation of giant polymer vesicles with controlled size distributions. *Nat. Mater.* **8**, 507–511 (2009).
15. D. E. Discher, A. Eisenberg, Polymer vesicles. *Science.* **297**, 967–973 (2002).

16. T. Litschel, P. Schwille, Protein Reconstitution Inside Giant Unilamellar Vesicles. *Annu. Rev. Biophys.* **50**, 525–548 (2021).

17. J. G. Bermudez, H. Chen, L. C. Einstein, M. C. Good, Probing the biology of cell boundary conditions through confinement of Xenopus cell-free cytoplasmic extracts. *Genesis* **55**, 1–10 (2017).

18. V. Noireaux, A. P. Liu, The New Age of Cell-Free Biology. *Annu. Rev. Biomed. Eng.* **22**, 51–77 (2020).

19. I. A. Chen, P. Walde, From self-assembled vesicles to protocells. *Cold Spring Harb. Perspect. Biol.* **2**, 1–14 (2010).

20. A. Kubilis, A. Abdulkarim, A. M. Eissa, N. R. Cameron, Giant Polymersome Protocells Dock with Virus Particle Mimics via Multivalent Glycan-Lectin Interactions. *Sci. Rep.* **6**, 32414 (2016).

21. H. J. Choi, C. D. Montemagno, Artificial organelle: ATP synthesis from cellular mimetic polymersomes. *Nano Lett.* **5**, 2538–2542 (2005).

22. N. P. Kamat, S. J. Henry, D. Lee, D. A. Hammer, Single-vesicle patterning of uniform, giant polymersomes into microarrays. *Small* **9**, 2272–2276 (2013).

23. A. J. Markvoort, *et al.*, Self-reproduction of fatty acid vesicles: A combined experimental and simulation study. *Biophys. J.* **99**, 1520–1528 (2010).

24. S. M. Baker, Synthetic Cells-Self-Assembling Polymer Membranes and Bioadhesive Colloids. *Integr. Med.* **4**, 10–11 (2005).

25. K. Fujiwara, M. Yanagisawa, S. M. Nomura, Reconstitution of intracellular environments in vitro and in artificial cells. *Biophysics (Oxf).* **10**, 43–48 (2014).

26. S. Li, B. Byrne, J. Welsh, A. F. Palmer, Self-Assembled Poly (butadiene)-b-poly(ethylene oxide) Polymersomes as Paclitaxel Carriers. *Biotechnol. Prog* **23**, 278–285 (2007).

27. C. Sanson, *et al.*, A simple method to achieve high doxorubicin loading in biodegradable polymersomes. *J. Control. Release* **147**, 428–435 (2010).

28. J. S. Lee, J. Feijen, Polymersomes for drug delivery: Design, formation and characterization. *J. Control. Release* **161**, 473–483 (2012).

29. A. H. Salama, M. H. Aburahma, Ufasomes nano-vesicles-based lyophilized platforms for intranasal delivery of cinnarizine: preparation, optimization, ex-vivo histopathological safety assessment and mucosal confocal imaging. *Pharm. Dev. Technol.* **21**, 1–10 (2015).

30. D. F. D. F. Do Nascimento, *et al.*, Microfluidic Fabrication of Pluronic Vesicles with Controlled Permeability. *Langmuir* **32**, 5350–5355 (2016).

31. S. H. Kim, H. C. Shum, J. W. Kim, J. C. Cho, D. A. Weitz, Multiple polymersomes for programmed release of multiple components. *J. Am. Chem. Soc.* **133**, 15165–15171 (2011).

32. N. S. Oltra, P. Nair, D. E. Discher, From Stealthy Polymersomes and Filomicelles to "Self" Peptide-Nanoparticles for Cancer Therapy. *Annu. Rev. Chem. Biomol. Eng.* **5**, 281–299 (2014).

33. P. J. Photos, L. Bacakova, B. Discher, F. S. Bates, D. E. Discher, Polymer vesicles in vivo: Correlations with PEG molecular weight. *J. Control. Release* **90**, 323–334 (2003).

34. T. Litschel, B. Ramm, R. Maas, M. Heymann, P. Schwille, Beating Vesicles: Encapsulated Protein Oscillations Cause Dynamic Membrane Deformations. *Angew. Chemie - Int. Ed.* **57**, 16286–16290 (2018).

35. I. López-Montero, *et al.*, Membrane reconstitution of FtsZ-ZipA complex inside giant spherical vesicles made of E. coli lipids: Large membrane dilation and analysis of membrane plasticity. *Biochim. Biophys. Acta - Biomembr.* **1828**, 687–698 (2013).

36. J. S. Hansen, K. Elbing, J. R. Thompson, N. Malmstadt, K. Lindkvist-Petersson, Glucose transport machinery reconstituted in cell models. *Chem. Commun.* **51**, 2316–2319 (2015).

37. B. Sun, D. T. Chiu, Determination of the encapsulation efficiency of individual vesicles using single-vesicle photolysis and confocal single-molecule detection. *Anal. Chem.* **77**, 2770–2776 (2005).

38. F. C. Tsai, B. Stuhrmann, G. H. Koenderink, Encapsulation of active cytoskeletal protein networks in cell-sized liposomes. *Langmuir* **27**, 10061–10071 (2011).

39. L. M. Dominak, C. D. Keating, Polymer encapsulation within giant lipid vesicles. *Langmuir* **23**, 7148–7154 (2007).

40. L. M. Dominak, C. D. Keating, Macromolecular crowding improves polymer encapsulation within giant lipid vesicles. *Langmuir* **24**, 13565–13571 (2008).

41. L. M. Dominak, D. M. Omiatek, E. L. Gundermann, M. L. Heien, C. D. Keating, Polymeric crowding agents improve passive biomacromolecule encapsulation in lipid vesicles. *Langmuir* **26**, 13195–13200 (2010).

42. K. Göpfrich, *et al.*, One-Pot Assembly of Complex Giant Unilamellar Vesicle-Based Synthetic Cells. *ACS Synth. Biol.* **8**, 937–947 (2019).

43. S. Pautot, B. J. Frisken, D. A. Weitz, Production of unilamellar vesicles using an inverted emulsion. *Langmuir* **19**, 2870–2879 (2003).

44. M. Tsugane, H. Suzuki, Reverse Transcription Polymerase Chain Reaction in Giant Unilamellar Vesicles. *Sci. Rep.* **8**, 1–11 (2018).

45. A. Moga, N. Yandrapalli, R. Dimova, T. Robinson, Optimization of the Inverted Emulsion Method for High-Yield Production of Biomimetic Giant Unilamellar Vesicles. *ChemBioChem* **20**, 2674–2682 (2019).

46. B. Xu, J. Ding, J. Xu, T. Yomo, Giant vesicles produced with phosphatidylcholines (Pcs) and phosphatidylethanolamines (pes) by water-in-oil inverted emulsions. *Life* **11** (2021).

47. C. W. Coyne, *et al.*, Lipid Bilayer Vesicle Generation Using Microfluidic Jetting. *J. Vis. Exp.*, 1–6 (2014).

48. M. Sun, Z. Li, S. Wang, G. Maryu, Q. Yang, Building Dynamic Cellular Machineries in Droplet-Based Artificial Cells with Single-Droplet Tracking and Analysis. *Anal. Chem.* (2019) https:/doi.org/10.1021/acs.analchem.9b01481.

49. Y. C. Tan, K. Hettiarachchi, M. Siu, Y. R. Pan, A. P. Lee, Controlled microfluidic encapsulation of cells, proteins, and microbeads in lipid vesicles. *J. Am. Chem. Soc.* **128**, 5656–5658 (2006).

50. A. Jahn, W. N. Vreeland, M. Gaitan, L. E. Locascio, Controlled Vesicle Self-Assembly in Microfluidic Channels with Hydrodynamic Focusing. *J. Am. Chem. Soc.* **126**, 2674–2675 (2004).

51. K. Morigaki, P. Walde, Giant vesicle formation from oleic acid/sodium oleate on glass surfaces induced by adsorbed hydrocarbon molecules. *Langmuir* **18**, 10509–10511 (2002).

52. K. S. Horger, D. J. Estes, R. Capone, M. Mayer, Films of agarose enable rapid formation of giant liposomes in solutions of physiologic ionic strength. *J. Am. Chem. Soc.* **131**, 1810–1819 (2009).

53. H. Stein, S. Spindler, N. Bonakdar, C. Wang, V. Sandoghdar, Production of isolated giant unilamellar vesicles under high salt concentrations. *Front. Physiol.* **8**, 1–16 (2017).

54. K. I. Akashi, H. Miyata, H. Itoh, K. Kinosita, Preparation of giant liposomes in physiological conditions and their characterization under an optical microscope. *Biophys. J.* **71**, 3242–3250 (1996).

55. C. Has, P. Sunthar, A comprehensive review on recent preparation techniques of liposomes. *J. Liposome Res.* **30**, 336–365 (2020).

56. K. Tsumoto, H. Matsuo, M. Tomita, T. Yoshimura, Efficient formation of giant liposomes through the gentle hydration of phosphatidylcholine films doped with sugar. *Colloids Surfaces B Biointerfaces* **68**, 98–105 (2009).

57. A. Cooper, V. Girish, A. B. Subramaniam, Osmotic pressure enables high yield assembly of giant vesicles in solutions of physiological ionic strengths. *Langmuir* (2023).

58. R. B. Lira, R. Dimova, K. A. Riske, Giant unilamellar vesicles formed by hybrid films of agarose and lipids display altered mechanical properties. *Biophys. J.* **107**, 1609–1619 (2014).

59. S. R. Kirchner, *et al.*, Membrane composition of jetted lipid vesicles: A Raman spectroscopy study. *J. Biophotonics* **5**, 40–46 (2012).

60. J. C. Blain, J. W. Szostak, Progress toward synthetic cells. *Annu. Rev. Biochem.* **83**, 615–640 (2014).

61. B. C. Buddingh', J. C. M. Van Hest, Artificial Cells: Synthetic Compartments with Life-like Functionality and Adaptivity. *Acc. Chem. Res.* **50**, 769–777 (2017).

62. B. C. Buddingh', J. C. M. Van Hest, Artificial Cells: Synthetic Compartments with Life-like Functionality and Adaptivity. *Acc. Chem. Res.* **50**, 769–777 (2017).

63. Y. Mulla, A. Aufderhorst-Roberts, G. H. Koenderink, Shaping up synthetic cells. *Phys. Biol.* **15** (2018).

64. M. Kærn, T. C. Elston, W. J. Blake, J. J. Collins, Stochasticity in gene expression: From theories to phenotypes. *Nat. Rev. Genet.* **6**, 451–464 (2005).

65. B. B. Kaufmann, A. van Oudenaarden, Stochastic gene expression: from single molecules to the proteome. *Curr. Opin. Genet. Dev.* **17**, 107–112 (2007).

66. R. Losick, C. Desplan, Stochasticity and cell fate. *Science.* **320**, 65–68 (2008).

67. E. Altamura, P. Carrara, F. D'Angelo, F. Mavelli, P. Stano, Extrinsic stochastic factors (solute partition) in gene expression inside lipid vesicles and lipid-stabilized water-in-oil droplets: a review. *Synth. Biol.* **3**, 1–16 (2018).

68. Y. Guan, *et al.*, A robust and tunable mitotic oscillator in artificial cells. *Elife* **7** (2018).

69. M. Weitz, *et al.*, Diversity in the dynamical behaviour of a compartmentalized programmable biochemical oscillator. *Nat. Chem.* **6**, 295–302 (2014).

70. K. Nishimura, S. Tsuru, H. Suzuki, T. Yomo, Stochasticity in gene expression in a cell-sized compartment. *ACS Synth. Biol.* **4**, 566–576 (2015).

71. H. Saito, *et al.*, Time-resolved tracking of a minimum gene expression system reconstituted in giant liposomes. *ChemBioChem* **10**, 1640–1643 (2009).

72. D. Blanken, P. Van Nies, C. Danelon, Quantitative imaging of gene-expressing liposomes reveals rare favorable phenotypes. *Phys. Biol.* **16** (2019).

73. K. Nishimura, *et al.*, Cell-free protein synthesis inside giant unilamellar vesicles analyzed by flow cytometry. *Langmuir* **28**, 8426–8432 (2012).

74. S. I. M. Nomura, *et al.*, Gene Expression within Cell-Sized Lipid Vesicles. *ChemBioChem* **4**, 1172–1175 (2003).

75. D. K. Karig, S. Y. Jung, B. Srijanto, C. P. Collier, M. L. Simpson, Probing cell-free gene expression noise in femtoliter volumes. *ACS Synth. Biol.* **2**, 497–505 (2013).

76. M. Abkarian, E. Loiseau, G. Massiera, Continuous droplet interface crossing encapsulation (cDICE) for high throughput monodisperse vesicle design. *Soft Matter* **7**, 4610–4614 (2011).

77. D. Van Swaay, A. Demello, Microfluidic methods for forming liposomes. *Lab Chip* **13**, 752–767 (2013).

78. B. Okumus, T. J. Wilson, D. M. J. Lilley, T. Ha, Vesicle encapsulation studies reveal that single molecule ribozyme heterogeneities are intrinsic. *Biophys. J.* **87**, 2798–2806 (2004).

79. G. Longatte, *et al.*, Statistical predictions on the encapsulation of single molecule

binding pairs into sized-dispersed nanocontainers. *Phys. Chem. Chem. Phys.* **24**, 28029–28039 (2022).

80. N. Friedman, L. Cai, X. S. Xie, Linking stochastic dynamics to population distribution: An analytical framework of gene expression. *Phys. Rev. Lett.* **97**, 1–4 (2006).

81. C. Jia, A. Singh, R. Grima, *Concentration fluctuations in growing and dividing cells: Insights into the emergence of concentration homeostasis* (2022).

82. Z. Cao, R. Grima, Analytical distributions for detailed models of stochastic gene expression in eukaryotic cells. *Proc. Natl. Acad. Sci. U. S. A.* **117**, 4682–4692 (2020).

83. L. Ham, R. D. Brackston, M. P. H. Stumpf, Extrinsic Noise and Heavy-Tailed Laws in Gene Expression. *Phys. Rev. Lett.* **124**, 108–101 (2020).

84. M. B. Elowitz, A. J. Levine, E. D. Siggia, P. S. Swain, Stochastic gene expression in a single cell. *Science.* **297**, 1183–1186 (2002).

85. A. Sigal, *et al.*, Variability and memory of protein levels in human cells. *Nature* **444**, 643–646 (2006).

86. K. I. Akashi, H. Miyata, H. Itoh, K. Kinosita, Formation of giant liposomes promotedby divalent cations: Critical role of electrostatic repulsion. *Biophys. J.* **74**, 2973–2982 (1998).

87. F. C. Tsai, B. Stuhrmann, G. H. Koenderink, Encapsulation of active cytoskeletal protein networks in cell-sized liposomes. *Langmuir* **27**, 10061–10071 (2011).

88. J. T. Marsh, F. C. Wood, *An Introduction to the Chemistry of Cellulose* (Ossler Press, 1939).

89. S. R. Kirchner, *et al.*, Membrane composition of jetted lipid vesicles: A Raman spectroscopy study. *J. Biophotonics* **5**, 40–46 (2012).

90. J. Heisler, A. Chavan, Y.-G. Chang, A. LiWang, Real-Time In Vitro Fluorescence Anisotropy of the Cyanobacterial Circadian Clock. *Methods Protoc.* **2**, 42 (2019).

91. S. D. Chandradoss, *et al.*, Surface passivation for single-molecule protein studies. *J. Vis. Exp.*, 1–8 (2014).

92. J. Jonkman, C. M. Brown, G. D. Wright, K. I. Anderson, A. J. North, Tutorial: guidance for quantitative confocal microscopy. *Nat. Protoc.* **15**, 1585–1611 (2020).

93. A. Ferrand, K. D. Schleicher, N. Ehrenfeuchter, W. Heusermann, O. Biehlmaier, Using the NoiSee workflow to measure signal-to-noise ratios of confocal microscopes. *Sci. Rep.* **9**, 1–12 (2019).

94. C. L. Smith, Basic confocal microscopy. *Curr. Protoc. Neurosci.* (2011) https:/doi.org/10.1002/0471142301.ns0202s56.

95. J. B. Pawley, Handbook of biological confocal microscopy: Third edition. *Handb. Biol. Confocal Microsc. Third Ed.* **3rd**, 442–452 (2006).

96. D. Regan, J. Williams, P. Borri, W. Langbein, Lipid Bilayer Thickness Measured by

Quantitative DIC Reveals Phase Transitions and Effects of Substrate Hydrophilicity. *Langmuir* **35**, 13805–13814 (2019).

97. J. Pan, S. Tristram-Nagle, N. Kučerka, J. F. Nagle, Temperature dependence of structure, bending rigidity, and bilayer interactions of dioleoylphosphatidylcholine bilayers. *Biophys. J.* **94**, 117–124 (2008).

98. J. Gallová, D. Uhríková, A. Islamov, A. Kuklin, P. Balgavý, Effect of cholesterol on the bilayer thickness in unilamellar extruded DLPC and DOPC liposomes: SANS contrast variation study. *Gen. Physiol. Biophys.* **23**, 113–128 (2004).

99. D. Huh, J. Paulsson, Random partitioning of molecules at cell division. *Proc. Natl. Acad. Sci. U. S. A.* **108**, 15004–15009 (2011).

100. M. Soltani, C. A. Vargas-Garcia, D. Antunes, A. Singh, Intercellular Variability in Protein Levels from Stochastic Expression and Noisy Cell Cycle Processes. *PLoS Comput. Biol.* **12**, 1–23 (2016).

101. A. Eldar, M. B. Elowitz, Functional roles for noise in genetic circuits. *Nature* **467**, 167–173 (2010).

102. A. Bar-Even, *et al.*, Noise in protein expression scales with natural protein abundance. *Nat. Genet.* **38**, 636–643 (2006).

103. H. Kageyama, *et al.*, Cyanobacterial Circadian Pacemaker: Kai Protein Complex Dynamics in the KaiC Phosphorylation Cycle In Vitro. *Mol. Cell* **23**, 161–171 (2006).

Chapter 3: Intracellular variation and membrane binding hampers circadian clock fidelity: An approach using cell-mimetic giant vesicles.

3.1 Introduction

Chapter 2 characterized the encapsulation of proteins in giant unilamellar vesicles (GUVs) and revealed that cellular levels of variation can be replicated in populations of GUVs using the method OSM-PAPYRUS. This indicated the potential use of GUVs to study cellular systems in an environment that more closely resembles the cell. Now, to demonstrate the practical applications of using GUVs, a cellular system will be encapsulated and explored to determine if significant findings can be obtained from using the GUV based minimal cell model, and if it can be advantageous over bulk in vitro and in vivo experimentation. The primary requirements will be a system that is relatively well studied using bulk in vitro and/or in vivo experiments, and that the system in question must be able to function in a cell-free setting. There must also be some open questions that could be answered by encapsulating into a GUV minimal cell model.

3.1.1 The Core Clock Protein Oscillator from Cyanobacteria

Circadian clocks systems allow organisms, including humans, the ability to anticipate the predictable and ubiquitous day/night cycle, linking the timing to key cellular functions including metabolism and gene expression (103, 104), confer fitness enhancements (105, 106), and more broadly has important implication in our sleep cycles (107–110). Though, not only large complex organisms such as animals have circadian clocks, in fact single-celled organisms such as the cyanobacteria, *Synechococcus elongatus (S. elongatus)* is among the simplest organisms with a circadian clock (104, 111–116). The full circadian clock involves the three Kai clock proteins, KaiA, KaiB and KaiC (111, 117–120), the input-output sensor histidine kinase, *Synechococcus* adaptive sensor A (SasA) (121), and the circadian input kinase A (CikA) (120, 122). The whole clock involves a transcription-translation feedback loop (123, 124) but it was found that the core oscillator, consisting of KaiA, KaiB and KaiC clock proteins, acts as a post-translational oscillator (PTO) (103) and that TTFL is not required for robust ~24 hour oscillations for bulk experiments in vitro (112). This opened the way to a large number of in vitro studies on the clock and many discoveries were found on the interactions of the clock. The core oscillator centers around the oscillation of the ordered phosphorylation of KaiC (125, 126), with KaiA stimulating the autophosphorylation of KaiC (103, 127–129), and the formation of KaiBC complexes that sequester KaiA, reducing phosphorylation rate of KaiC, and acting as the negative feedback loop (103, 130, 131) which will eventually allow KaiC to dephosphorylate and reset the system (129, 130). The interactions between these clock proteins and formation of protein complexes make up the circadian oscillation without any transcriptional feedback. The state of the clock may be measured by measuring KaiC phosphorylation state (103, 111, 119, 132, 133), or the use of fluorescence anisotropy to measure the formation of KaiBC and KaiABC complexes (90, 134). Later in this chapter, fluorescence intensity would be introduced as a viable way to measure the clock state as well through quenching of KaiB-6IAF upon forming KaiBC complexes.

3.1.2 Encapsulating the clock within giant unilamellar vesicles

Studies on the clock using typical bulk in vitro techniques usually involve large volumes on the order of 10 μL or 10^{-5} L, while cellular volumes are typically much smaller closer to 10^{-15} L. There are some open questions regarding the core oscillator of the clock regarding how the clock may function differently confined in a cell-sized volume with cell-like variation. A study of the clock in vivo, which looked at the varying the expression level of the Kai clock proteins while disabling the TTFL mechanism by replacing native *kai* genes with copies containing a theophylline-inducible riboswitch (135). The authors found that high copy numbers were important to reduce the effect of stochastic interactions that lead to a large variation in the period of oscillations (135). Yet in vitro studies have found that maximum period variation is smaller even when proteins stoichiometry is modulated (134). There have also been reports suggesting that the Kai proteins are found in the membrane fractions of cell extracts (111) and that the Kai proteins can dynamically localize to the membrane according to the circadian rhythm (136). Bulk in vitro experiments lack a membrane for the clock proteins to interact with so the impact of membrane localization cannot be well studied. Bulk clock reactions in vitro have shown the core oscillator can tick reliably for as many as 12 days (90, 134, 137–139). Due to stochastic gene expression, degradation, turnover, and unequal partitioning during cytokinesis, intercellular noise can be as large as ~10-50 % in prokaryotic cells, and ~10-30 % in eukaryotic cells in vivo (64, 65, 84, 85, 140). The variation of proteins between cyanobacteria produced from the *kaiBC* promoter is estimated to exhibit a coefficient of variation (CV) of approximately 25% to 30% (141). This closely matches the estimates for the CV exhibited by OSM-PAPYRUS of ~30% (**2.3.3**).

This chapter will explore how encapsulating the clock into GUVs can be used to understand the effect of cellular properties. This includes confinement in cell-like volumes, presence of phospholipid bilayers, and intercellular variation. These properties will be shown to affect the clock oscillations in ways that could not be appreciated by in vitro bulk studies. The clock behavior under varying protein expression levels will also be compared with results reported in both in vivo and bulk in vitro studies. The GUV model will be shown to act as a bridge between the well-defined and controlled nature of in vitro studies and the ability to mimic cellular properties from in vivo studies. The findings suggest that delegation of the TTFL as less important in comparison to the post-translational core oscillator is no longer as clear when intercellular variation is involved. It will also highlight how the complicated nature of in vivo studies may make it difficult to determine whether certain behavior arises from the intended target of study, in this case, the core oscillator. With encapsulation statistics characterized in **Chapter 2**, a model is produced that can predict the robustness of the clock and expected period deviations based off known limitations from bulk studies. The interaction of the Kai protein with the membrane will be investigated and localization is shown to be able to occur on these synthetic phospholipid bilayer membranes.

3.1.3 Cyanobacteria membrane and lipid vesicle membrane composition

In this chapter, the GUVs are comprised of a synthetic phospholipid bilayer composed of 94.4 mol % of DOPC, 5 mol % of DSPE-PEG2K, 0.5 mol % of DSPE-PEG2K-Biotin, and 0.1 mol % of RhPE (see **2.2.4**). DOPC is a monounsaturated zwitterionic lipid, meaning the fatty acid chains each have one carbon double bond and have positive and negative charges, but a net charge of 0. These lipids form a super majority in the GUV (94.5 mol %). The GUVs also contain 5 mol % of DSPE-PEG2K, which is a polyethylene glycol (PEG) functionalized saturated anionic lipid with a net charge of -1. This PEG functionalized lipid provides steric repulsion to prevent aggregation of GUV membranes in buffers with high salt concentrations (e.g., 1× clock buffer). A biotinylated version of DSPE-PEG2K (DSPE-PEG2K-Biotin) allows the GUVs to be immobilized by allowing binding to streptavidin proteins that can be functionalized to glass surfaces. Lastly, the RhPE is labeled with a rhodamine fluorophore, that allows imaging of the GUVs membranes. The molecular structure diagrams of these lipids are shown in **Fig. 3.1**. These lipids were picked primarily because they have been well studied and have been tested by us to produce large numbers of GUVs in high salt with the OSM-PAPYRUS method.

The lipid composition of these GUVs is expected to differ from lipids that make up cyanobacteria membranes. The cyanobacteria membrane is primarily composed of neutral polyunsaturated galactolipids (monogalactosyldiacylglycerol (MGDG) and digalactosyldiacylglycerol (DGDG)) and anionic lipids (sulfoquinovosyldiacylglycerol (SQDG) and phosphatidylglycerol (PG)) (142–147). The galactolipids, primarily MGDG and DGDG, which composes of >80 mol% of lipids in the plastid envelope and >90 mol% of lipids in the thylakoid membranes (143). These have a high content of polyunsaturated fatty acids, both 18:3 (linolenic acid) and 16:3 (hexadecatrienoic acid), with some smaller proportions monounsaturated fatty acids chains (16:1) (144). The molecular structure diagrams of these lipids are shown in **Fig. 3.2**. Note that GUVs are spherical, while cyanobacteria can be described as spherocylinders, so the surface volume to area ratio would be greater for cyanobacteria. Additionally cyanobacteria have multiple membranes, including outer, inner, and thylakoid membranes (136, 143, 150).

Although the lipid composition of GUVs and bacteria differ, phosphocholine (PC) lipids are often used to take the place of bacteria membranes when studying membrane interactions of various membrane and cytoskeletal proteins in vitro (34, 148, 149). In these cases, membrane interactions still occur in the PC lipid dominated membranes and provide insightful discoveries. Therefore, PC lipids can be suitable for studies of membrane interactions despite differences to the bacteria membranes.

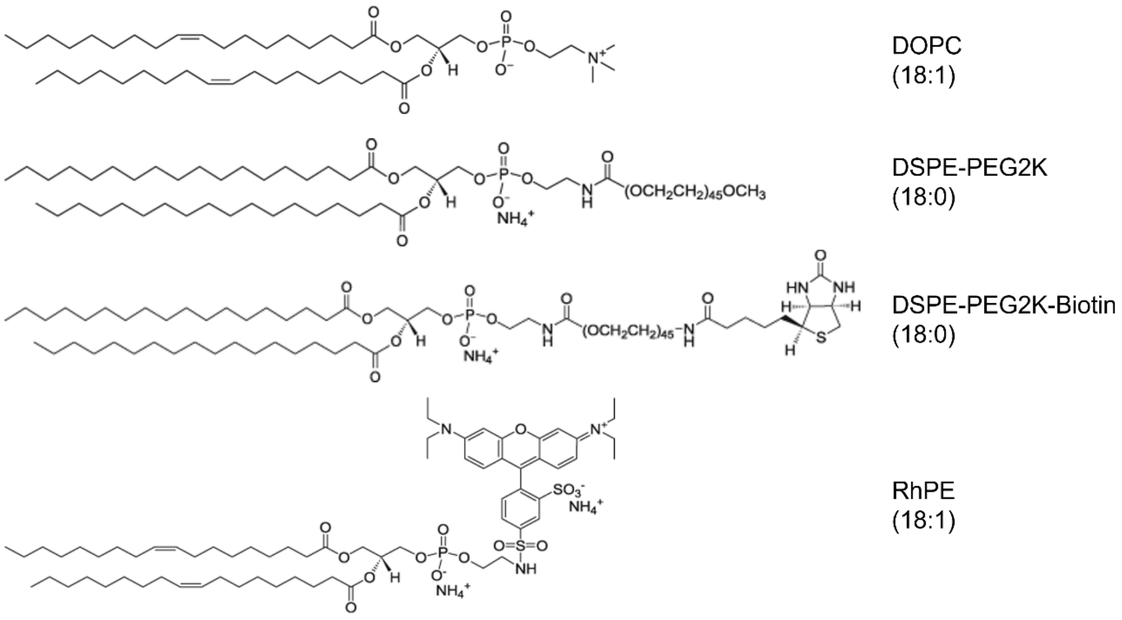

Fig. 3.1. Molecular structure diagram of lipid types in vesicles produced in this chapter. Vesicles produced in this chapter are comprised of DOPC, DSPE-PEG2K, DSPE-PEG2K-Biotin, and RhPE. In the parentheses the first number refers to the number of carbons in the fatty acid chain, and the second number refers to the number of double bonds.

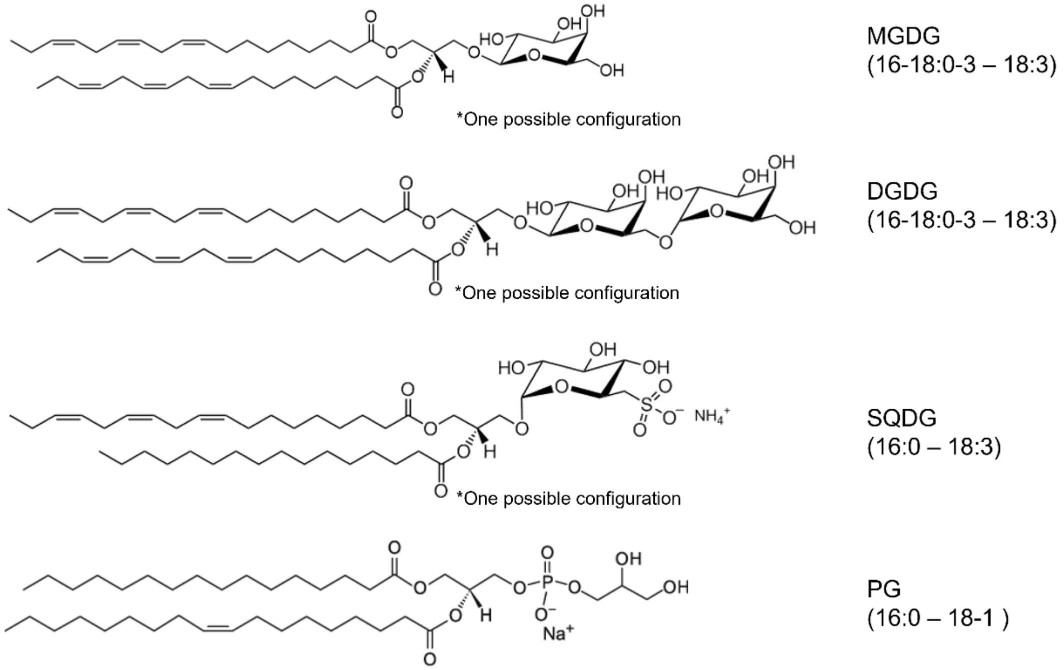

Fig. 3.2. Molecular structure diagram of primary lipid types in cyanobacteria. In the parentheses the first number refers to the number of carbons in the fatty acid chain, and the second number refers to the number of double bonds. These lipids may have varying configurations.

3.2 Materials and Methods

3.2.1 Materials

The following were purchased, Gold Seal™ 60 × 22 mm glass coverslips, Fisherbrand TM Premium Plain Glass Microscope Slides (75 mm × 25 mm), CELLSTAR® black clear bottom 96 well plates (Greiner), Coplin glass staining jars (DWK Life Sciences), Corning® 15 mm diameter regenerated cellulose syringe filters (0.2 μm pore size), and MilliporeSigmaTM UltrafreeTM-MC centrifugal filter devices (0.22 μm pore size) from Thermo Fisher Scientific (Waltham, MA). The following was purchased, artist grade tracing paper (Jack Richeson & Co., Inc.), circular hole punches (EK Tools Circle Punch, 3/8 in.), square hollow punch cutters (Amon Tech) from Amazon Inc. (Seattle, WA).

3.2.2 Chemicals

The following was purchased, sucrose (BioXtra grade, purity ≥ 99.5%), glucose (BioXtra grade, purity ≥ 99.5%), bovine albumin-fluorescein isothiocyanate conjugate (FITC-BSA) (albumin from bovine, ≥ 7 mol FITC/mol albumin), sodium chloride (NaCl) (ACS grade, VWR International), manganese (II) chloride tetrahydrate ($MgCl_2$) (ReagentPlus grade, ≥ 99%, Sigma-Aldrich), and ethylenediaminetetraacetic acid (EDTA) (BioReagent grade ≥ 98.5%) from Sigma-Aldrich (St. Louis, MO). The following was purchased, chloroform (ACS grade, purity ≥ 99.8%, with 0.75% ethanol as preservative), 1 N potassium hydroxide (KOH) (Certified grade, 0.995 to 1.005N, Fisher Chemical), 3-aminopropyl trimethoxysilane (APTES) (≥ 98.5%, ACROS Organics), glacial acetic acid (ACS grade, ≥ 99.7%, Fisher Chemical), methanol (ACS grade, ≥ 99.8%, Fisher Chemical), adenosine 5'-triphosphate (ATP solution) (Tris-buffered, > 99% purity via HPLC, Thermo Scientific) from Thermo Fisher Scientific (Waltham, MA). 18.2 MΩ ultrapure water was obtained from an ELGA Pure-lab Ultra water purification system (Woodridge, IL). The following was purchased, 1,2-dioleoyl-*sn*-glycero-3-phosphocholine (18:1 (Δ9-cis) PC (DOPC)), 1,2-distearoyl-*sn*-glycero-3-phosphoethanolamine-N-(methoxy(polyethylene glycol)-2000) (18:0 DSPE-PEG2K), 1,2-distearoyl-*sn*-glycero-3-phosphoethanolamine-N-(biotinyl(polyethylene glycol)-2000) (DSPE-PEG2K-Biotin), and 1,2-dioleoyl-*sn*-glycero-3-phosphoethanolamine-N-(lissamine rhodamine B sulfonyl) (RhPE) from Avanti Polar Lipids, Inc. (Alabaster, AL). NHS-ester polyethylene glycol (mPEG) (5 kDa) and biotinylated NHS-ester PEG (biotin-mPEG) (5 kDa) was purchased from Laysan Bio, Inc. (Arab, AL).

3.2.3 Preparation of Kai clock proteins and buffers.

Previously published protocols was used to express, purify, and label KaiA, KaiB, KaiB-6IAF, and KaiC (90). The 10× clock buffer consists of 200 mM Tris, 1500 mM NaCl, 50 mM MgCl2, 10 mM ATP, and 5 mM EDTA. The 1× clock buffer consists of 20 mM Tris, 150 mM NaCl, 5 mM MgCl2, 1 mM ATP, and 0.5 mM EDTA (90). The budding buffer consists of 119 mM sucrose. The sedimentation buffer is the 1× clock buffer with 100 mM glucose.

3.2.4 Bulk clock reaction measurements of fluorescence intensity

Place 50 μL of the reactions into wells in a black clear bottom 96-well plate. To minimize evaporation during the multiday experiments, fill empty wells in the plate with ultrapure water. Use a SpectraMax® M2e plate reader to measure the mean fluorescence intensity every 30 minutes using bottom read. The chamber temperature is set to 30 °C, fluorescence was excited at 485 nm, and emission was collected at 530-538 nm. Measurements were taken with high detector sensitivity and each data point is an average of 6 reads.

3.2.5 Fluorescence quenching measurements

Tryptophan residues quench the fluorescence intensity of conjugated fluorophores (2). KaiC has 6 tryptophan residues per hexamer near the KaiB-binding site on the CI domain (3). Determine if the binding of KaiB-6IAF to KaiC quenches the fluorescence of KaiB-6IAF by titrating fully-phosphorylated cold-conditioned KaiC from 0 μM to 7 μM into a 50:50 mixture of KaiB:KaiB-6IAF. Add 25 μL of 50:50 mixture of KaiB:KaiB-6IAF at a concentration 7 μM to 25 μL of serially diluted KaiC in a black clear bottom 96 well plate and. The final concentration of the 50:50 mixture of KaiB:KaiB-6IAF is 3.5 μM (1× wild type (WT) concentration). Since KaiB binds slowly to fully phosphorylated KaiC, kinetic plots of the mean intensity of KaiB-6IAF over 22 hours are obtained. Observations show that the intensity of KaiB6IAF drops monotonically in a manner that depended on the concentration of KaiC. For concentrations of KaiC > 0.22 μM, a minimum of intensity was reached after 10 hours, reflective of the slow binding kinetics of KaiB to KaiC. The change in intensity is plotted at 10 hours relative to the initial intensity versus the concentration of KaiC. The change in intensity decreased linearly with increasing KaiC concentration up to 3.5 μM. Beyond this concentration, the change in intensity saturated. This result confirms that KaiC acts as a quencher for KaiB-6IAF due to KaiC-KaiB binding. Monitoring the change in mean fluorescence intensity should allow determination of complex formation between 50:50 mixture of KaiB:KaiB-6IAF and KaiC.

3.2.6 Bulk clock reaction measurements

0.5× concentrations contain 0.6 μM KaiA, 0.88 μM KaiB, 0.88 μM KaiB-6IAF, and 1.75 μM KaiC. 0.75× concentrations contain 0.9 μM KaiA, 1.31 μM KaiB, 1.31 μM KaiB-6IAF, and 2.63 μM KaiC. 1.0× concentrations contain 1.2 μM KaiA, 1.75 μM KaiB, 1.75 μM KaiB-6IAF, and 3.5 μM KaiC. 1.5× WT concentrations contain 1.8 μM KaiA, 2.63 μM KaiB, 2.63 μM KaiB-6IAF, and 5.25 μM KaiC. Kinetic measurements of fluorescence intensity were taken for 96 hours.

3.2.7 Preparation of coverslips functionalized with PEG-Biotin

Follow protocols previously dictated in **Chapter 2.2.6**.

3.2.8 Protein loading solutions

Protein loading solution were prepared at 15× the intended final protein concentration in 10 μL of 1× clock buffer. The solution is filtered using MilliporeSigma™ Ultrafree™ -MC centrifugal filters in a microcentrifuge at 12,000 revolutions per minute (RPM) for 3 minutes to remove any aggregated protein. For clock reactions, the 15× protein loading solution consists of 9 μM KaiA, 13.1 μM KaiB, 13.1 μM KaiB-6IAF, and 26.3 μM KaiC for 0.5× protein concentrations, 13.5 μM KaiA, 19.7 μM KaiB, 19.7 μM KaiB-6IAF, and 39.4 μM KaiC for 0.75× protein concentrations, 18 μM KaiA, 26.25 μM KaiB, 26.25 μM KaiB-6IAF, and 52.5 μM KaiC for 1× protein concentrations, 27 μM KaiA, 39.4 μM KaiB, 39.4 μM KaiB-6IAF, and 78.8 μM KaiC for 1.5× protein concentrations.

3.2.9 Assembly of vesicles and loading of proteins

Follow protocols previously dictated in **Chapter 2.2.7**.

3.2.10 Sample preparation for imaging

Follow protocols previously dictated in **Chapter 2.2.8** with the following modifications:

Do not place a coverslip on the chamber during sedimentation. Insure the sample is covered by a 100 mm Petri dish cover and contains two folded Kimwipes saturated with water to prevent evaporation (**Fig. 3.3A**). For the time series imaging of clock reactions in vesicles, additional steps are performed to minimize evaporation and interference from unbound vesicles and unencapsulated protein, that require the chamber to not be sealed by a coverslip. After 3 hours, exchange the sedimentation buffer with vesicle free hydration buffer. Then gently remove 30 μL of the supernatant from the sample and add 30 μL of fresh vesicle-free hydration buffer. Repeat this process five times. Then seal the imaging chamber with a circular glass coverslip (diameter = 12 mm), which produces a 1 mm overhang around the imaging chamber. The overhang is filled with Loctite® Instant Mix Epoxy and allowed at least 15 minutes to set before imaging (**Fig. 3.3B**). Sealing with epoxy minimizes evaporation from the chamber over the multi-day course of imaging. Failure to seal with epoxy will cause large air bubbles that form which will interfere with imaging and can change the concentration of the solutions and in the vesicle.

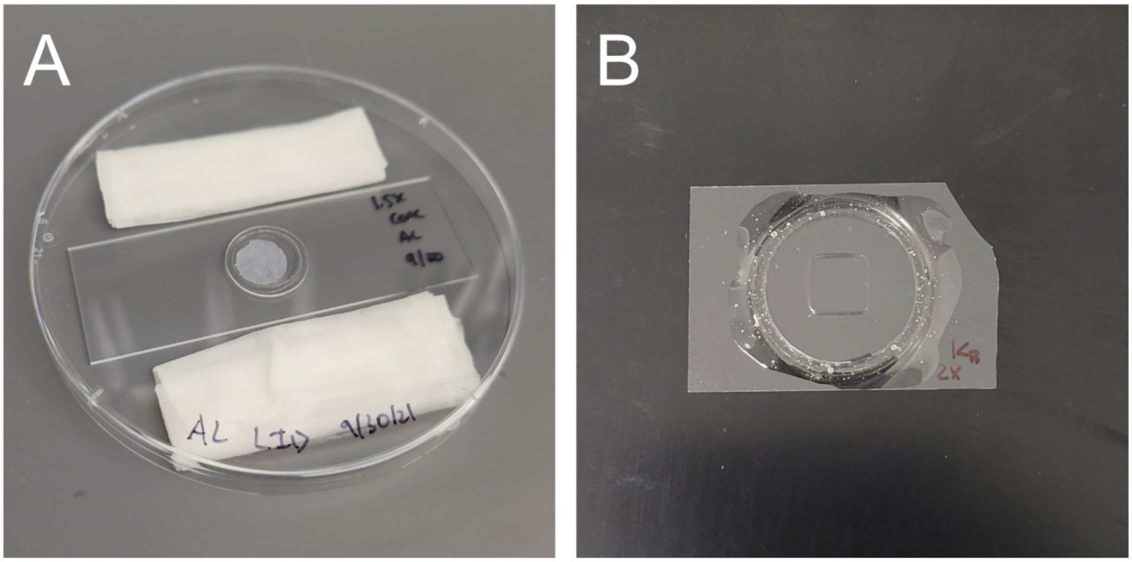

Fig. 3.3. Sample preparation for imaging. (A) Sample during diffusive loading step of OSM-PAPYRUS is covered with a 100 mm petri dish lid with two folded Kimwipes saturated with water. **(B)** Imaging chamber after sealing with epoxy to prevent evaporation.

3.2.11 Imaging of clock loaded vesicles

The vesicles and proteins are imaged via dual-channel imaging using a Zeiss LSM 700 on an upright stand with a 20×/0.8 NA Plan-Apochromat objective. The sample chamber is flipped so that the vesicles are close to the objective on the upright stand and placed onto a Peltier stage set to 33 °C, which corresponds to a sample temperature of 30 °C. The 'red' channel was configured to image the rhodamine-PE in the GUV membranes, and the 'green' channel was configured to image the fluorescein labeled KaiB (KaiB-6IAF channel). The rhodamine-PE was excited with a 555 nm laser and the KaiB-6IAF was excited with a 488 nm laser. The timeseries imaging consists of 10 positions (328 × 328 μm per position) over the course of 5 days, imaging every 2 hours. Positions are chosen so they contain many vesicles with polydisperse size distributions to sample a large range of vesicle sizes. Reflection-based autofocus is used prior to capturing each image to determine the z-position of the glass surface and imaging a specified offset (+5 μm) into the sample. Images were taken with a resolution of 2048 × 2048 pixels (0.16 × 0.16 μm pixel size) with 4× line averaging. The pinhole was set to 13.6 Airy Units (AU), corresponding to a 26.7 μm section. Core measurements are not used and the whole vesicle is measured to maximum signal. Background leakage is not a concern as the background is cleared in these samples.

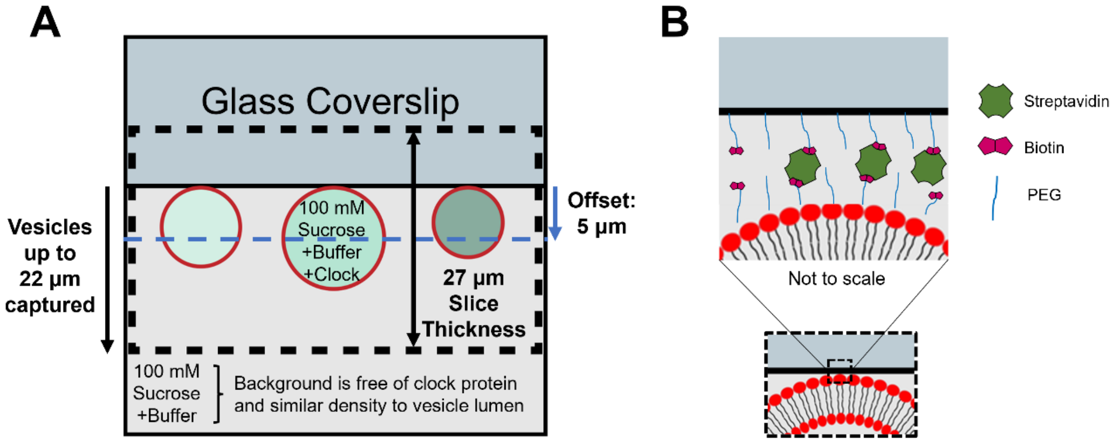

Fig. 3.4. Schematic of imaging setup for clock vesicles. (A) The axial focal plane is set at an offset of 5 µm from the surface of the glass coverslip, with a slice thickness of ~27 µm. This means vesicles up to 22 µm in diameter will be expected to be fully captured in the axial sectioning. The background is free of clock protein and has a similar density to the vesicle lumen. **(B)** Streptavidin-biotin binding is used to tether the vesicles to the surface of the biotin functionalized glass coverslip. Note protein and lipids sizes are not to scale, they are shown here for visualization.

3.2.12 Time series initial processing

Preprocess the raw native *.czi* time series images using the *MultiStackReg* plugin with the 'Translation' algorithm in ImageJ to align the images. The alignment corrects for random drifts in the images that occur at each acquisition time point. Objects ranging from 1 µm up to 40 µm are present within the images. Select objects with diameters of 2, 3, 4, 6, 8, and 10 µm for analysis. Further curate the vesicles by manually removing objects that do not resemble GUV (defined as spherical objects with uniform intensities). Empty vesicles are identified as the vesicles with the bottom 20% of mean intensity values for each size.

3.2.13 Time traces of fluorescence intensity

Obtain the time-trace of the intensity of the KaiB-6IAF from each vesicle using the *regionprops* MATLAB function. The time-trace of the background intensity is subtracted from the vesicle signals. The signals are normalized by the intensity at t*=0. The normalized KaiB-6IAF time traces of each vesicle are then detrended by fitting a two-term exponential decay equation ($y = ae^{bt} + ce^{dt}$). Here the zero time represents the time the first image was taken, occurring approximately 7 hours after the clock reaction was created.

3.2.14 Fast Fourier Transform (FFT) analysis for clock behavior

A fast Fourier transform (FFT) is performed with 1000 point zero-padding on each of the time traces. The FFT spectrum is converted into a single-sided amplitude spectrum. The Kai proteins are expected to have a maximum period range of 20 to 26 hours in bulk even under extreme protein stoichiometry changes (134). The *findpeaks* MATLAB function is used to find the global maxima peak within 16 to 30 hours. To be classified as oscillating the global peak must have a height of > 0.04 and a signal-to-noise ratio (SNR) of 1.3 to exclude cases where high frequency noise with large amplitude can be erroneously detected as a signal within our expected oscillation frequency range. The frequency of the peak location is converted into the characteristic period of oscillation for that clock vesicle.

This analysis resulted in ≤ 1% of the vesicles from the negative control being falsely identified as oscillating for vesicles ≥ 3 μm in diameter. For the signal inside the vesicles, the same FFT analysis was performed. If no peaks were detected above the minimum noise threshold, we consider that vesicle to not oscillate. Clock fidelity is the sum of vesicles that oscillate divided by the total number of vesicles in the group. A clock fidelity value of zero would mean no vesicles oscillate and one would mean all vesicles oscillate.

3.2.15 Model: Assignment of Kai proteins in vesicles

Because proteins form complexes during encapsulation and co-encapsulate together, it is estimated that approximately 13% of KaiC are expected to form a KaiABC protein complex prior to vesicle extraction based on KaiC serial dilution data at the time of vesicle extraction. The KaiABC complex is assumed to consist of KaiA, KaiB and KaiC monomers in a 12:6:6 molar ratio (129, 151). Then independently assign KaiA, KaiB, KaiC, and KaiABC concentrations in 5000 simulated vesicles by sampling with a gamma distribution with the shape parameter, k, and scale parameter, θ. The parameter values are determined assuming a CV of 0.31 and a mean concentration (μ) corresponding to the loading concentration of the protein (μ = loading concentration, see **2.3.3**) with the co-encapsulated concentration (x) of KaiA, KaiB, and KaiC in the KaiABC complex subtracted. Then the parameters can be calculated with $k = 1/CV^2$ and $\theta = CV^2(\mu - x)$. For KaiABC gamma distributions the μ is 13% of the KaiC loading concentration while the CV remains the same. Each vesicle thus has a range of KaiA, KaiB, KaiC, and KaiABC concentrations. After the gamma distribution is created, the concentration of the constituent components of the KaiABC complexes are redistributed back into the respective KaiA, KaiB, or KaiC concentrations.

KaiB binds to the membrane, thus reducing the free concentration of KaiB in the lumen. We use an estimate of 650 KaiB monomers bound per μm^2 of surface area of the vesicle. This estimate is similar to the number of KaiB molecules bound *in vivo*, ~447 to 715 KaiB monomer per μm^2 surface area of a cyanobacteria, assuming two concentric membranes (103). However, cyanobacteria have multiple membranes, an outer membrane, plasma membrane, and internal thylakoid membranes (136, 150), so the true number of KaiB monomers bound per μm^2 of membrane area may be much closer to our estimate. Using

Eq. 11 where initial KaiC concentration, and a *b* value of 650, we reduce the concentration of free KaiB ($C_{free,\,KaiB}$) based on the amount of KaiB bound to the membrane (bA_s). We define free protein as protein located in the lumen of the vesicle and consider membrane bound KaiB to be unavailable to participate in the clock reaction.

$$C_{free,\,KaiB} = C_{i,KaiB}\left(V_i C_{i,KaiB} N_A - \frac{b}{C_{i,KaiB} N_A}\frac{3}{r}\right) \qquad \textbf{Eq. 11}$$

3.2.16 Model: Limiting concentration and ratio conditions

Limiting concentrations ($C_{L,[X]}$) and ratios are obtained from our bulk plate reader experiments and stoichiometric ratios from values in the literature. The clock fails in our bulk experiments when the concentration of the clock proteins is 0.5× WT concentration, that is when the concentration of KaiA < 0.6 μM, KaiB < 1.75 μM, and KaiC < 1.75 μM. This result is consistent with previous bulk measurements (103, 134, 152). The limiting stoichiometric ratios of KaiA and KaiB are measured relative to a fixed KaiC concentrations (103, 134, 152). The limiting ratio of KaiA to KaiC ($R_{L,[KaiA:C]}$) is 0.17 and of KaiB to KaiC ($R_{L,[KaiB:C]}$) is 0.5. The upper limit of stoichiometric ratios between KaiA to KaiC is 1.02 (103, 134, 152). There appears to be no upper limit of stoichiometric ratios for KaiB to KaiC (134, 152).

3.2.17 Model: Fidelity calculations

A vesicle is considered to oscillate only if all the protein stoichiometries are at or above the defined limiting ratio, at or below the maximum ratios, and the concentration of free proteins are at or above the minimum concentration for all protein species. A measure of clock fidelity is determined by taking the sum of vesicles that do oscillate divided by the total number of vesicles in the group, where 0 would mean no vesicles oscillate and 1 would mean all vesicles oscillate.

3.2.18 Model: Simulation of periods

The oscillation period from our bulk measurements is used as our reference period for each loading concentration. The period is modified, which is for a fixed [KaiA]:[KaiB]:[KaiC] ratio of 1.2:3.5:3.5, with known effects of stoichiometric variation from rescaled data obtained from literature reports (134) using **Eq. 12**. The period data is recreated in **Fig. 3.5** for reference.

$$\mathrm{T_i} = \mathrm{T}_{[A]:\{B]:[C]} + \Delta\mathrm{T}_{[A]:[C]} + \Delta\mathrm{T}_{[B]:[C]} \qquad \textbf{Eq. 12}$$

For the boxplots of the simulated periods, the populations count (N) was matched to the counts measured in the experimental data for the respective data groups.

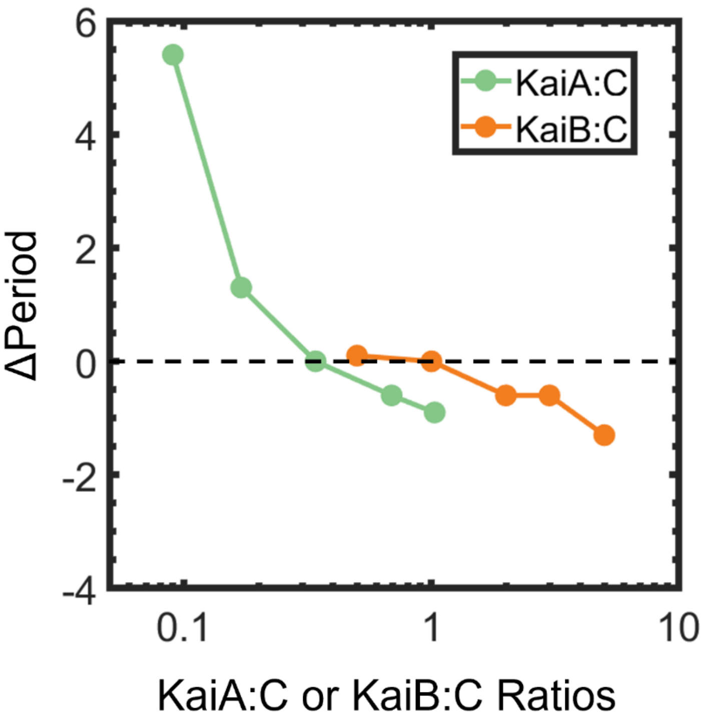

Fig. 3.5. Changes in period based off KaiA:KaiC and KaiB:KaiC ratios. The data is obtained from (134) and replotted here for reference. Changes in the ratio of KaiA to KaiC (KaiA:C) and ratio of KaiB to KaiC (KaiB:C) causes changes in the period.

3.2.19 Model: Amplitude Simulation

The amplitude from the bulk reaction and the mean amplitude from the population of oscillating vesicles both changed linearly with KaiC concentration. The amplitudes in bulk were 0.09 units higher than those measured in the vesicles, likely due to variation of protein stoichiometry and differences in imaging methodologies. We normalized amplitude values between the bulk and in vesicle simulations by subtracting 0.09 from all the amplitudes (**Fig. 3.6**). Amplitudes were only determined for vesicles that met the criteria for oscillation.

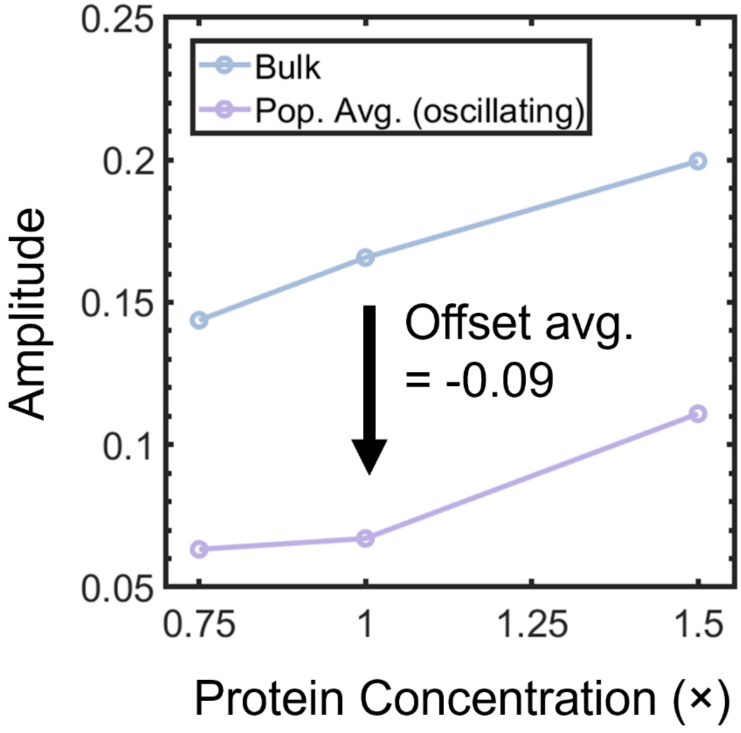

Fig. 3.6. Amplitude offset for simulated signals. Bulk amplitude is offset by -0.09 to meet the lower amplitude observed in vesicles for calculating amplitude in simulated signals.

3.2.20 Significance testing

Anderson Darling tests were performed to determine violation of normality in populations. Significance testing for equal variances was done with Levene's test (absolute differences), which is robust to violation of normality. The one-way analysis of variance (ANOVA) test is used to determine statistical significance between groups where the sample sizes are equal, and where no violation of normality occurs. ANOVA tests were used to determine the statistical significance of varying protein concentrations to the coefficient of variation of encapsulated protein concentrations and the fraction of empty vesicles. The non-parametric Kruskal Wallis one-way analysis of variance (KW-ANOVA) test is used to determine statistical significance between groups where the sample sizes are not equal and where a violation of normality occurs. KW-ANOVA tests were used to determine statistical significance of varying vesicles diameter to the encapsulated protein concentrations and varying protein loading concentrations to the oscillation period of the clock oscillator. The statistics for these significance tests are shown in **Appendix A.1 and A.2**.

3.2.21 Estimate of KaiB to lipid ratio in vivo

Approximately 50-80% of KaiB is estimated to reside with membrane bound fractions (111). The surface area of S. elongatus modeled as a spherocylinder with a length of 2.51 μm and radius of 1.12 μm, is 10.8 μm^2 (153). The volume of the elongatus is 2.11 μm^3. Using an in vivo copy number of 19,000 KaiB molecules and assuming two concentric membranes, 50% to 80% of the KaiB residing in the membrane leads to ~447 to 715 KaiB per μm^2 of membrane area.

3.3 Results and Discussion

3.3.1 The inner working of the core oscillator of the cyanobacterial circadian clock measured in real time using fluorescence intensity measurements

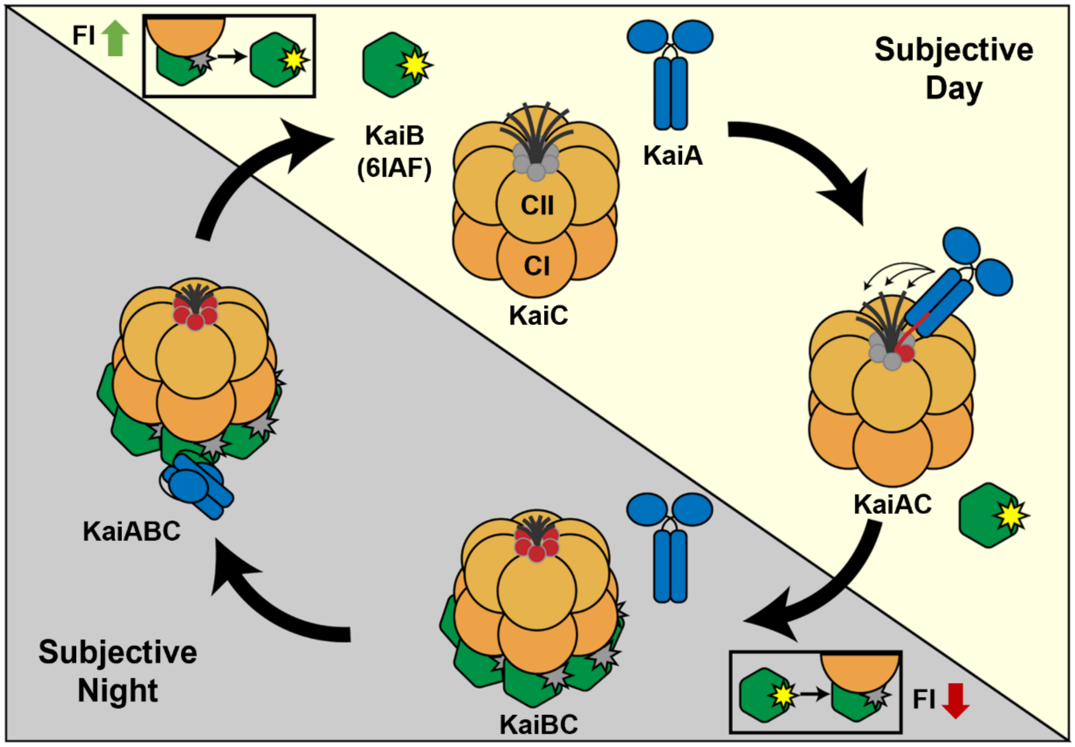

Fig. 3.7. Schematic of the oscillation cycle of the cyanobacterial circadian clock. (Top) Three Kai proteins, KaiA, KaiB (with 50 mol % KaiB-6IAF), and KaiC with ATP make up the core oscillator of the cyanobacterial circadian clock. (Right) During the subjective day, transient KaiAC complexes form and drive the autophosphorylation of KaiAC. During the subjective night (Bottom) KaiBC complexes form when KaiC becomes hyperphosphorylated (red circles), and upon complex formation KaiB-6IAF is quenched reducing fluorescence intensity (FI). (Left) KaiA is sequestered into KaiBC complexes to form KaiABC complexes. The cycle restarts when KaiC becomes fully dephosphorylated (Top), and the Kai proteins disassociate. KaiB-6IAF becomes unquenched and recovering its FI. Red circles on KaiC represent the phosphorylation state.

The core oscillator of the clock consists of the three clock proteins, KaiA, KaiB, and KaiC. This core oscillator along with adenosine triphosphate (ATP) generates robust oscillations in both KaiC phosphorylation (103, 111, 119, 132, 133) and the association of KaiBC complexes (90, 134) with a near 24 hours period in vitro. The core oscillator is considered post-translational so it does not require translational feedback to be able to function in vitro (103), although later in the chapter this point will be revisited with subtleties after exploration of clock behaviors in vesicles. The schematic in **Fig. 3.7** overviews the protein complex formations that comprises the oscillation. Here, during the subjective day starting from with the proteins in its disassociated states, KaiA transiently binds to the A-loops of the CII domain of KaiC to form KaiAC complexes, which then stimulates the auto-phosphorylation of KaiC (103, 127–129). When KaiC is not in a KaiAC complex, KaiC will undergo auto-dephosphorylation (127, 154). When all KaiC phosphorylation sites at residues S431 and T432 become phosphorylated (119, 133), referred to as hyperphosphorylated KaiC, KaiC will undergo a conformational change (125, 126), where the A-loops of the CII domain will be buried stopping further phosphorylation (127, 129, 154) and fold-switched monomer KaiB can bind to the now exposed B-loop of the CI domain (103, 129, 131, 155). The KaiBC complexes can then sequester KaiA in a KaiABC complex, reducing the concentration of free KaiA which in turns decreases the KaiC autophosphorylation rate, serving as a negative feedback control for the phosphorylation of KaiC (103, 130, 131). Sequestration of enough KaiA will allow KaiC to undergo net dephosphorylation, and the upon complete dephosphorylation will lead to the disassociation of KaiBC and KaiABC complexes and bring the cycle back to the starting point to begin again (129, 130). There are some addition mechanisms have been proposed, including the monomer exchange of KaiC (103, 132) and the KaiB fold switching (155), but are not reflected in **Fig. 3.7**.

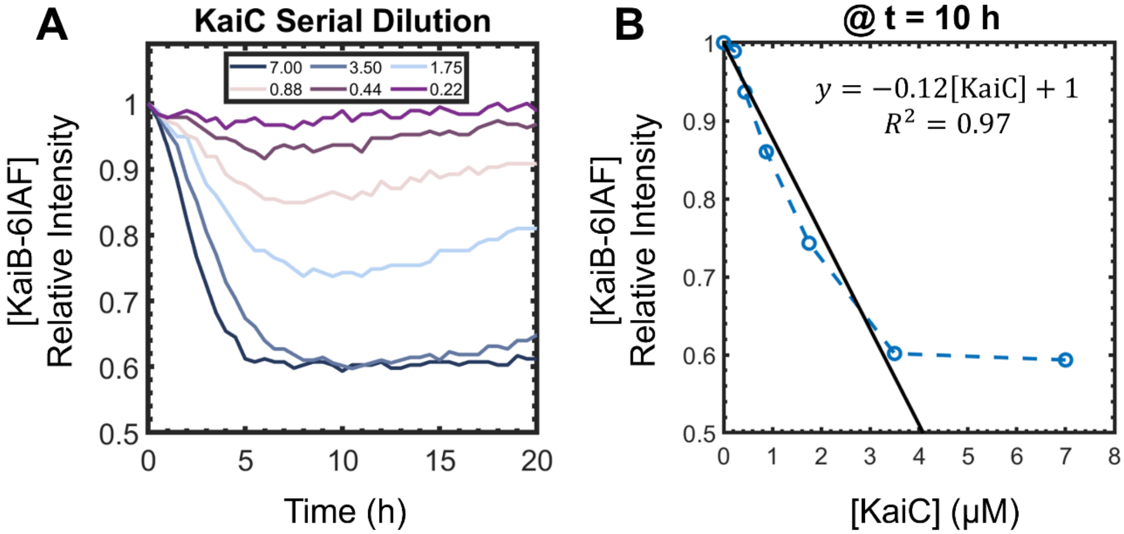

Fig. 3.8. Bulk kinetic quenching studies of KaiB and KaiC. (A) The relative intensity of KaiB-6IAF is measured with a serial dilution of KaiC (7 μM to 0.22 μM) and a constant 3.5 μM of KaiB:KaiB-6IAF (50:50 mol%). Relative intensity of KaiB-6IAF is calculated by taking the intensity divided by the initial intensity. **(B)** Relative intensity at time = 10 hours, reflecting the maximum quenching is plotted against the concentration of KaiC. A linear regression is fitted for the linear regime ($y = 0.12[KaiC] + 1, R^2 = 0.97$). The temperature was maintained at 30 °C.

Here, to obtain a readout on the state of the clock using fluorescence measurements, 50 mol % of the KaiB molecules are labeled using 6-Iodoacetamidofluorescein (6IAF) to form fluorescently labeled KaiB-6IAF. KaiB-6IAF becomes quenched when it forms a complex with KaiC (KaiBC & KaiABC complexes), reducing fluorescence intensity. When KaiB-6IAF complexes disassociate, it becomes unquenched again and fluorescent intensity is restored. This allows the real time readout of the state of the clock from using fluorescent intensity measurements. This quenching occurs due to the presence of tryptophan residues near the KaiB-binding site on the CI domain of KaiC (126). Tryptophan residues quench the fluorescent intensity of many fluorophores, such as the conjugated fluorescein on KaiB-6IAF (156). KaiB-6IAF and KaiC kinetic quenching studies were performed, shown in **Fig. 3.8A**, which demonstrates the quenching of KaiB-6IAF fluorescence intensity increases with the concentration of the quencher KaiC. Note that KaiBC complex formation can occur without even without the presence of KaiA because KaiC is initially hyperphosphorylated due to storage (-80 °C) and preparation in low temperatures (~4 °C), which are conditions that promote autophosphorylation of KaiC even without the presence of KaiA (132, 157, 158). **Fig. 3.8B** shows that the quenching of KaiB-6IAF by KaiC follows a linear relationship ($y = 0.12[KaiC] + 1, R^2 = 0.97$), until it hits a maximum quenching of ~40%, which represents the point with all avaliable KaiB is bound to KaiC. This matches the values reported for the quenching of fluorescein-peptide-tryptophan quenching, 42% (156). The maximum quenching occurred when KaiB and KaiC monomer concentrations were equal (3.5 μM KaiB and 3.5 μM KaiC), corroborating reports that KaiBC complexes form with a 6:6 monomer ratio (129, 151).

It has been previously shown that fluorescence anisotropy, which measures the change in rotational diffusion of the clock proteins when complexes form, can measure the real time clock state of the circadian clock (90). To ensure the use of fluorescence intensity to measure the quenching of KaiB-6IAF as it binds to KaiC accurately represents the oscillation of the clock, a concurrent measurement of fluorescence anisotropy was taken along with fluorescence intensity in **Fig. 3.9**. Here, when fluorescence anisotropy is at a local maximum, the fluorescence intensity is at a local minimum and vice versa. This shows that fluorescence intensity had an inverse relationship to anisotropy, so that when the maximum proportion of KaiBC complexes is present fluorescence intensity is minimized while fluorescence anisotropy is maximized. This does meet expectations as fluorescence anisotropy increases when the rotational diffusion decreases from complex formation, while fluorescence intensity decreases due to quenching of the KaiB-6IAF in a KaiBC complex. This demonstrates that fluorescence intensity is capable of measuring the clock state accurately. The reason for using fluorescence intensity at all, as opposed to fluorescence anisotropy, lies with the technical limitations of the LSM 700 microscope used to obtain images. The LSM 700 must obtain two images, one with parallel polarization and the other with perpendicular polarization, to be able to obtain the fluorescence anisotropy. This was of a particular concern due to the necessity of limiting the laser exposure to reduce photobleaching of fluorescent molecules during the long experimental imaging time (>4 days). In summary, these results show that this setup would allow reading the state of the encapsulated within giant unilamellar vesicles (GUVs) using fluorescence intensity measurements of the LSM 700.

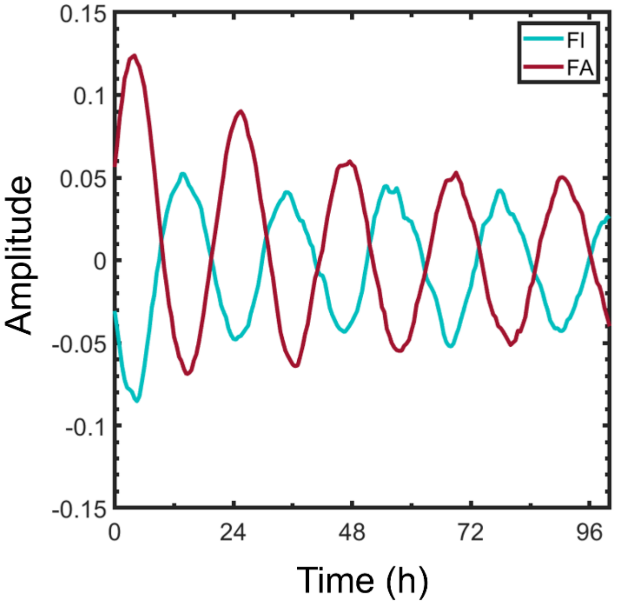

Fig. 3.9. Comparison of real time measurements of clock state using fluorescence intensity versus fluorescence anisotropy. Concurrent measurements of fluorescence intensity (FI) and fluorescence anisotropy (FA) for a 1× clock reaction is shown to be inversely correlated to one another. This shows FI may also be used to read the clock state, without the need for FA measurements. Amplitude shows the relative change in FI/FA over the mean FI/FA. FI and FA measurements are taken with a LSM 700 confocal microscope using a 10× 0.3 NA objective. Note, the fraction of KaiB-labeled (90:10 mol % KaiB:KaiB-6IAF) differs from later results. The temperature was maintained at 30 °C.

3.3.2 Behavior of the reconstituted circadian clock in giant unilamellar vesicles

Using the diffusive loading of OSM-PAPYRUS, the core oscillator of the cyanobacterial circadian is partitioned into vesicles. A 1× standard concentration is defined as 1.2 μM KaiA, 3.5 μM KaiB, and 3.5 μM KaiC according to standard concentrations commonly used for bulk experiments (90, 103, 152). In **Fig. 3.10A**, a 1× clock reaction is shown partitioned into giant vesicles. Here, the membrane is labeled in red, and the green channel represents the intensity of KaiB-6IAF, which can be used to read the clock oscillation over time. Images are captured once every 2 hours, for at least 100 hours. Three vesicles (V1 – V3) were selected for analysis (white dotted box) and in **Fig. 3.10B-D** a timelapse of the images show the intensity at 12-hour intervals over 60 hours for the three vesicles. Below that the heatmap of the timelapse helps accentuate changes in intensity during the time period. The amplitude, defined as the change of intensity in relation to the mean, is shown over a course of 100 hours with one data point every two hours.

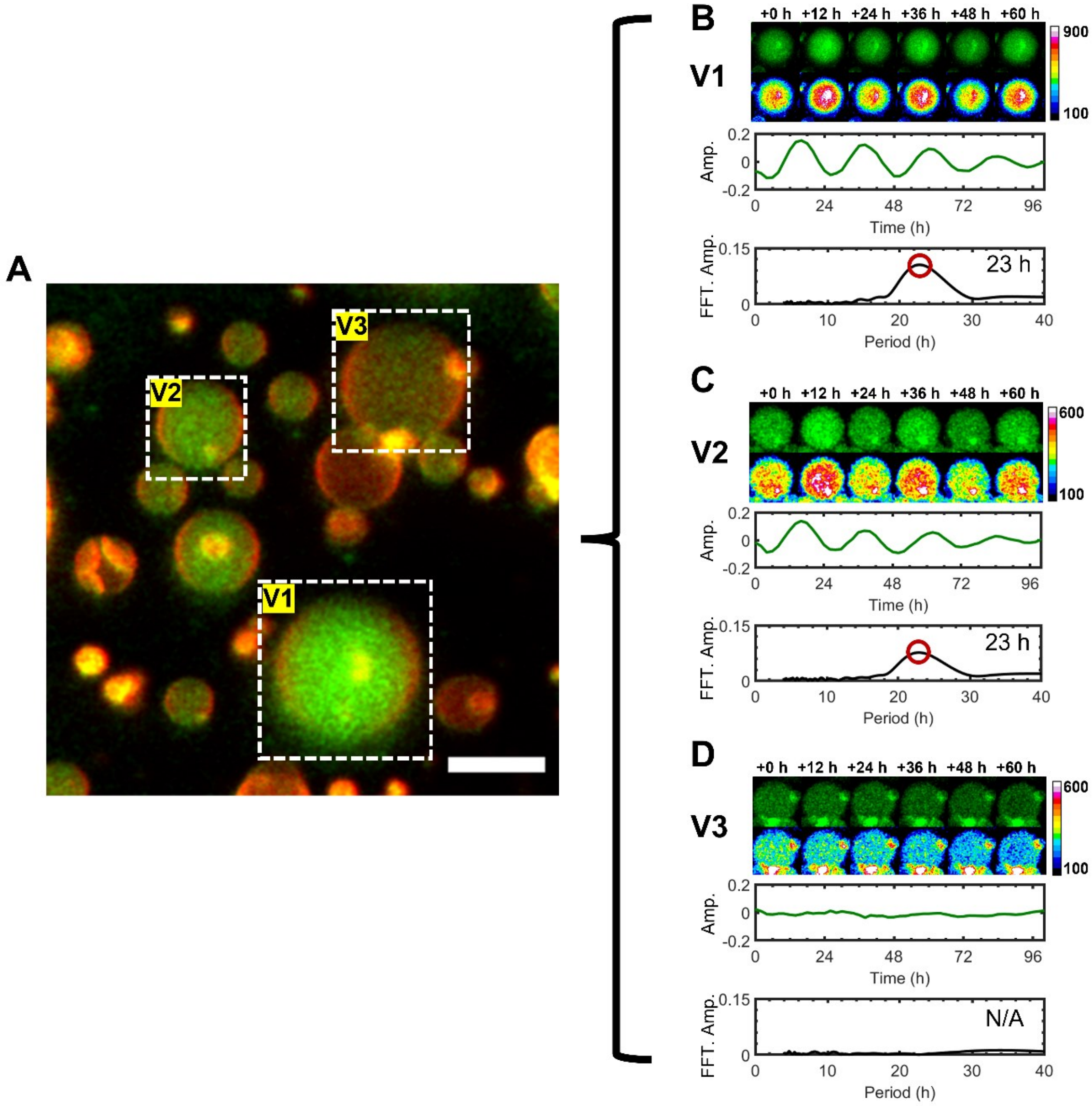

Fig. 3.10. Partitioned clocks in vesicles reconstitute the circadian rhythms, with some that do not tick. (A) Confocal images of vesicles (red) loaded with the 1× clock reaction with KaiB-6IAF fluorescently labeled (green). Three vesicles are selected for analysis and labeled V1 through V3 (white dotted boxes). Scale bars = 10 µm. **(B)**-**(D)** The fluorescence intensity of vesicles labeled V1 through V3 are shown here (green) from confocal images taken every 2 hours. A color mapped image is shown below the confocal images to emphasize the changes in intensity. Then a plot of the normalized amplitude (detrended plot of the intensity divided by the mean intensity) over time is shown. A fast-Fourier transform analysis is performed and the single-sided amplitude spectrum shows the detected period of oscillation. **(B)** V1 and **(C)** V2 showed circadian rhythms, but **(D)** V3 did not show any rhythms at all. The temperature was maintained at 30 °C.

The amplitude represents the proportion of KaiBC complexes that associate and disassociate. Then a fast Fourier transformation analysis is performed (see **3.2 Materials and Methods**) and the corresponding single-sided amplitude spectrum is shown in the bottom panel of **Fig. 3.10B-D**. This spectrum shows the characteristic period of oscillation for the intensity signal at the peak, and the height of the peak provides the characteristic amplitude of the signal. V1 and V2 in **Fig. 3.10** show a clear oscillation in fluorescence intensity with timelapses showing KaiB-6IAF intensities are rhythmically switching from dark to bright and vice versa, every ~12 hours. The intensity over time plot shows a strong signal and the FFT analysis can clearly register the oscillation and determine a near circadian period of ~23 hours. However, for V3 there seems to be no oscillatory behavior at all, but visually it can be seen that it did encapsulate the clock protein. This suggests that diffusive loading with OSM-PAPYRUS is potentially causing the clock to not be able to function in some cases. Overall, this does show the clock can be successfully reconstituted into vesicles using the OSM-PAPYRUS technique, but there are some behavior changes to the clock which will be explored in further detail.

3.3.3 Comparison of clock behavior between bulk and partitioned reactions

Next, in order to gain a sense of how the clock behavior has changed after partitioning into vesicles, bulk 50 μL reactions were prepared (**Fig. 3.11A**) for comparison. To get a broad sense of the behavior of the clock as an entire population, the average intensity of the GUV partitioned population is assessed (**Fig. 3.11B**) and compared to the bulk reactions. Here, the concentration of clock protein is varied from 0.5×, 0.75×, 1.0×, 1.5×, and 2.5× concentrations (denoted by color legend in **Fig. 3.5**) to mimic a global variation of protein expression levels. The temperature for all clock experiments was maintained at 30 °C. A KaiC- negative control is also performed, where KaiC is removed, and other protein concentrations remain at 1×. The lack of KaiC will not allow any oscillations to occur. In **Fig. 3.11A** the relative changes in intensity of the bulk reaction (amplitude) over time is presented along with the single-sided amplitude spectrum (SSAS) from the FFT analysis, showing the amplitude in the top left and period in the top right of the SSAS. Similarly, in **Fig. 3.11B** the amplitude over time is presented with the SSAS and associated amplitude and period data for the population averaged signal for each protein concentration. First the term, robust circadian oscillations, is defined as a sustained oscillations over a course of 100 hours (~4 days) without large dampening of the oscillation. The bulk reactions (**Fig. 3.11A**) show the oscillation remains robust for 0.75× to 2.5× clock concentrations, but 0.5× failed to show a robust oscillation, instead showing a heavily dampened oscillation. The population of GUV partitioned clock in **Fig. 3.11B** maintained oscillations for 0.75× to 2.5× clock concentrations, although compared to the bulk, the amplitude of oscillation is significantly reduced across the board. At 0.5× neither the bulk nor partitioned reactions could show sustained oscillations. The KaiC- negative control did not produce any oscillations as expected for both bulk and partitioned reactions, confirming that the detected oscillations did not occur from factors outside of the intended experimental design that may also have circadian patterns, such as temperature fluctuations from HVAC or weather.

Fig. 3.11C shows the amplitude of the bulk and GUV partitioned reactions as a function of protein concentration. The amplitude of the bulk sustained oscillations ranged from 0.06 to 0.20 and was consistently greater than the amplitude from the GUV partitioned reactions, which ranged from 0.03 to 0.13. The amplitude was positively correlated with protein concentration for both the bulk and partitioned reactions, but the bulk reaction reached an amplitude plateau of ~0.2, at and above 1.5× concentrations. This amplitude plateau corresponds to a peak-to-peak height of the signal to be ~0.4, or a 40% change in intensity. The amplitude plateau corresponds to the expected maximum quenching of ~40% in **Fig. 3.8** when all avaliable KaiB is bound to KaiC, suggesting it at ≥1.5× concentrations all avaliable KaiB becomes bound to KaiC. In **Fig. 3.11A,** there is also a noticeably flattened trough for the 2.5× bulk reaction which further corroborates the complete KaiB association to KaiC.

The period of the bulk and partitioned reactions is shown in **Fig. 3.11D** as a function of protein concentration. In general, the period for both bulk and partitioned reactions remained relatively constant at ~23 hours even with increasing proteins concentrations, until 2.5× concentrations, where the period was slightly shortened at ~22 hours for both the bulk and partitioned reactions. In general, the rate of reaction is dependent on concentration so clock has a strong ability to be resistant to changes in concentrations, likely arising from the negative feedback control of KaiA sequestration (129, 130). Based on this data the slightly shortened period seen for 2.5× concentrations occurs when all avaliable KaiB is bound to KaiC, which in addition to limiting amplitude, also limits the creation of new KaiA sequestration sites as they are on KaiBC complexes. So, this suggests the shortened period results from the increase in KaiA sequestration sites no longer scaling with the increased reaction rate when concentrations higher than 2.5×. However, this still likely only has small impacts to the oscillation when considering the binding stiochiometry for KaiABC complexes is a maximum of 12:6:6 monomers of KaiA:KaiB:KaiC (129, 151). The protein monomer stiochiometry ratio is maintained at 1.2:3.5:3.5 for KaiA:KaiB:KaiC, meaning there are ~5.8× more KaiA sequestration sites than needed to fully sequester KaiA. So, the KaiA can still be completely sequestered, just at a slightly slower rate.

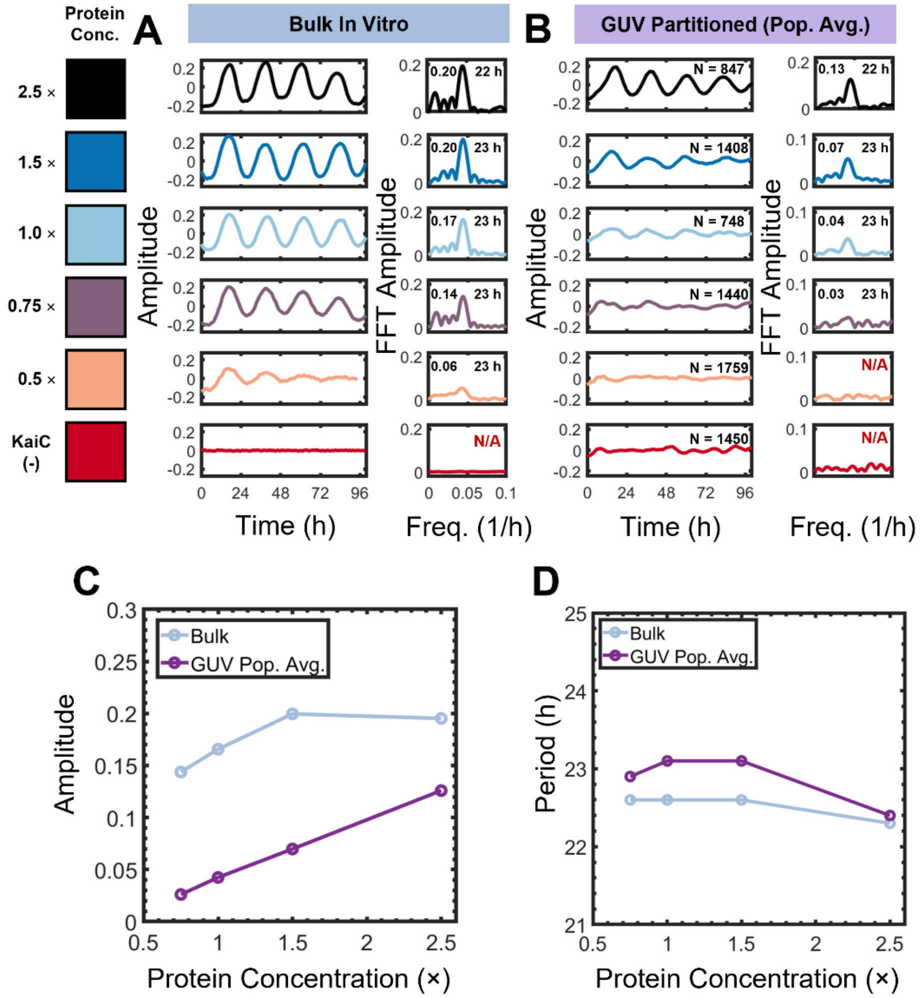

Fig. 3.11 Clock reactions in vesicle populations show diverging behavior from bulk reactions. (A) Bulk in vitro measurements of circadian clock rhythms across a range of clock protein concentrations (0.5× to 2.5×, various colors) evaluated using a 50 μL reaction volumes in a plate reader. The normalized clock amplitude (detrended, normalized by mean intensity) over time is shown in the left panel and the amplitude spectrum from our fast Fourier transform (FFT) analysis is shown in the right panel with the amplitude (top left) and period labeled (top right). **(B)** Population averaged circadian clock rhythms from vesicles across varying clock protein concentrations (0.5× to 2.5×, various colors). The population average normalized clock amplitude (detrended, normalized by mean intensity) over time is shown in the left panel. The total number of vesicles contributing (N = 847 to 1759) is shown in the top right of the left panel and includes data from 3, 4, 6, 8 and 10 μm vesicles. The amplitude spectrum is shown in the right panel with the amplitude (top left) and period labeled (top right). **(C)** The amplitude of the bulk reactions (light blue) and population averaged (Pop. Avg.) reaction from giant unilamellar vesicles (GUVs) (purple) are plotted against the protein loading concentration. **(D)** The period of the bulk reactions (light blue) and population averaged (Pop. Avg.) reaction from giant unilamellar vesicles (GUVs) (purple) are plotted against the protein loading concentration. The temperature was maintained at 30 °C for all.

So why is a minimum concentration for sustained oscillations observed for the clock? The data presented suggests that the clock has a strong concentration compensation system, likely largely due to the KaiA negative feedback loop (129, 130). **Fig. 3.12** summarizes the KaiA driven phosphorylation cycle of KaiC and how the KaiA negative feedback loop is incorporated. KaiAC complexes promote KaiC autophosphorylation proportional to the free KaiA concentration in the reaction. When KaiC is hyperphosphorylated KaiBC complexes can form, and in turn sequester KaiA into KaiABC complexes. But what happens when total protein concentration is reduced? In **Fig. 3.12** the green arrows demonstrate concentration dependent phosphorylation, while the red arrows demonstrate concentration independent dephosphorylation. KaiC dephosphorylation rate is independent of protein concentrations because it is an inherent property of KaiC and such, does not necessitate binding of other proteins. However, phosphorylation is dependent on KaiA – KaiC interactions. Then as global protein expression levels are reduced, KaiA phosphorylation rate will also continue to decrease. However, KaiC dephosphorylation rate will remain constant, and if the KaiA induced phosphorylation rate drops low enough, there will be a point where KaiC dephosphorylation will outpace KaiA induced phosphorylation. The cycle will be stuck in the subjective day, unable to sufficiently reach the hyperphosphorylated state of KaiC (KaiC*).

This is the proposed mechanism for why a minimum concentration of proteins is necessary. It may not be necessary for KaiA induced phosphorylation to drop completely below KaiC dephosphorylation rates to cause non-sustained oscillations, just close enough where when the KaiA negative feedback loop kicks in and quickly subdues further KaiC phosphorylation. Additionally, the clock system does not start at an equilibrium, instead it starts with all KaiC presumed to be hyperphosphorylated due to the cold temperatures during preparation and storage. This means that initially, KaiBC complex formation will readily occur and act as a jump start to the system. But if KaiA induced phosphorylation rates are too low, it can cause significant dampening as the system enters into an equilibrium state.

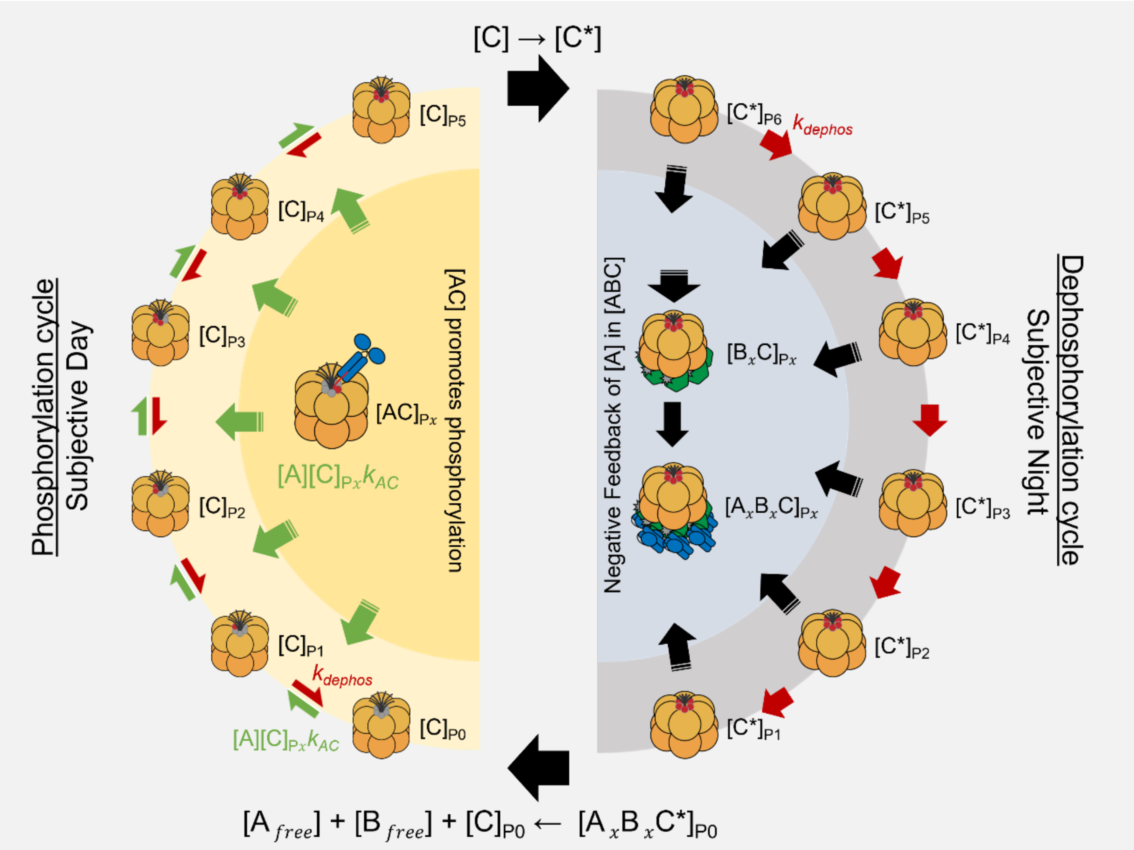

Fig. 3.12. Schematic of the KaiA driven phosphorylation cycle of KaiC. Green arrows show concentration dependent phosphorylation, while red arrows show concentration independent dephosphorylation. Inner half circles show complex formations that drive (stripped arrows out) or are driven by the cycle (stripped arrows in). Brackets indicate concentration of KaiA ([A]), KaiB ([B]), KaiC ([C]). [AC] complexes promote [C] phosphorylation in the subjective day, until hyperphosphorylation, when [C] undergoes conformation change to [C*]. [C*] only undergoes dephosphorylation but allows [BC] and [ABC] complex formation at any point. [ABC] complexes will reduce free [A] acting as the negative feedback loop.

The characteristic amplitude in **Fig. 3.11A&C** can allow the estimation of the proportion of KaiBC complexes that form. The amplitude is proportional to the percentage of KaiB that participates in the association and disassociation of KaiBC/KaiABC complexes. In **Fig. 3.8**, kinetic quenching studies with static KaiB and varying KaiC concentrations show when KaiB is paired with excess quantities of KaiC*, quenching reduces intensity by a maximum of ~40% when all KaiB-6IAF is bound to KaiC*. This allows the calculation of percent KaiB participation in forming KaiBC complexes using **Eq. 13**, where the proportion of KaiB in KaiBC complexes (p_{BC}) can be calculated using the amplitude (A) and the 0.4 represents the maximum quenching when p_{BC} is at 100%.

$$p_{BC} = \frac{2A}{0.4}$$ **Eq. 13**

Table 5 shows the characteristic amplitude of bulk in vitro data and the calculated percent of KaiB participation. As expected, as the concentration of KaiA is reduced while maintaining a fixed stoichiometry, the average number of KaiBC complexes that form falls which is evident by the drop in amplitude. The oscillation however can be maintained for concentration of proteins at 0.75× and above. At the 0.5× protein concentration the number of KaiBC complexes that form drops dramatically, and the oscillation is not sustained. This proposes that at or below 0.5×, the rate phosphorylation of KaiC from formation of KaiAC complexes is equal to or lower than the intrinsic KaiC auto-dephosphorylation rate. This prevents the KaiC from reaching hyperphosphorylated state and leads to heavily dampened and non-sustained oscillation as seen for the 0.5× bulk clock reaction in **Fig. 3.11A**.

Table 5. Analysis of the amplitude of bulk reactions in context of proportion of Kai proteins participating in the oscillation.

Total Protein Concentration	Characteristic Amplitude	Average KaiBC complexes	Sustained Oscillation?
0.5×	0.06	28 %	No
0.75×	0.14	72 %	Yes
1.0×	0.17	83 %	Yes
1.5×	0.20	100 %	Yes
2.5×	0.20	100 %	Yes

The behavior of vesicle partitioned clock reactions in **Fig. 3.11B&C** includes vesicles even if they do no oscillate, like the case seen in **Fig. 3.10D**, so the population averaged signal and amplitude is mixed in with those vesicles. To determine what changes that would have on the population averaged signals, only vesicles that had clock rhythms were included in the population averaging in **Fig. 3.13A&B** using a FFT analysis (see **3.2 Methods and Materials**) to determine which vesicles had robust clock rhythms. Here, the clock rhythm shows a clearer clock rhythm for 0.75× protein concentrations and above. The amplitude increases across the board, as now the vesicles that do not oscillate are excluded. Interestingly, the amplitude still does not reach bulk amplitude levels, suggesting there are still other mechanisms from partitioning that affect the amplitude of oscillating clock reactions in vesicles. The period of oscillation did not show any significant changes when observing the population of oscillating clock vesicles.

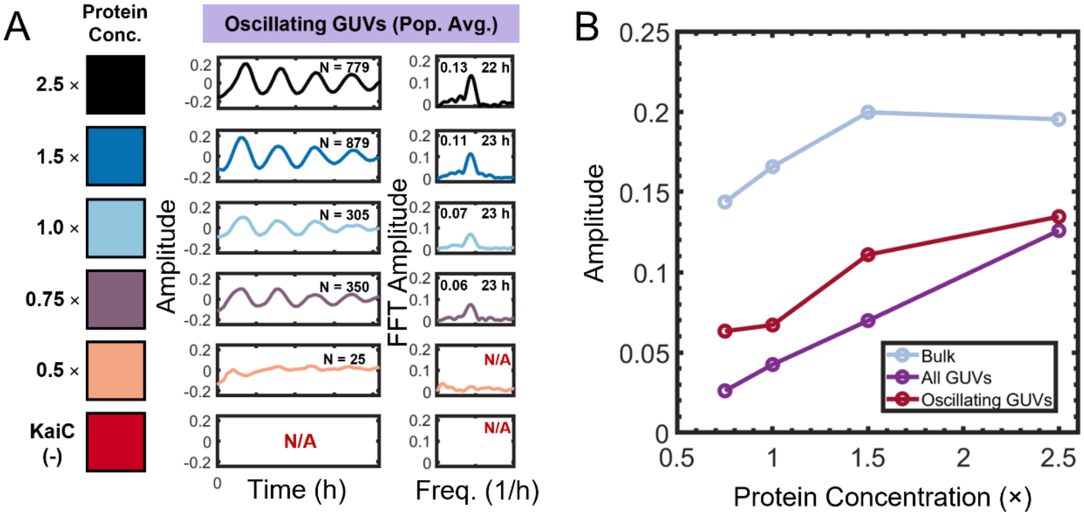

Fig. 3.13. Population averaged partitioned clock reactions from oscillating vesicles. (A) Population average of oscillating vesicles determined using a FFT analysis routine. The number of vesicles ranged from 25 to 879 for various protein loading concentrations. Amplitude and period are denoted in the top left and top right, respectively, of the FFT single-sided amplitude spectrum. **(B)** The amplitude of population averaged oscillating giant unilamellar vesicles (GUVs) (red) are compared to the amplitude of the bulk reactions (light blue) and population averaged reaction from GUVs (purple), as a function of protein loading concentration.

3.3.4 Single vesicle analysis of clock fidelity reveals concentration and size dependency

In order to better understand the differences in behavior observed between the bulk and partitioned clocks, and the effect of varying expression levels, the clock behavior is investigated at the single vesicle level. A FFT analysis was conducted for each individual clock vesicle to determine whether it expressed sustained clock oscillations. The total proportion of clock vesicles in a population that show circadian rhythms is defined as clock fidelity. Due to the relatively large polydisperse size range of vesicles, they were separated into diameter size classes of 3±0.5 μm, 4±0.5 μm, 6±0.5 μm, 8±0.5 μm, and 10±0.5 μm. Vesicles with diameters greater than 10 μm may still be used for analysis, but the number of vesicles in size classes above 10 μm had significantly lower counts. Vesicles in size classes of 2 μm or lower had too much noise to be able to accurately and consistently determine whether the clock rhythm exists. In **Table 6**, the false positive rates of the KaiC- negative control show the FFT analysis routine was robust in not detecting noise as oscillations, with false positive rates of less than 3% for all size range tested. Due to the possibility that random noise from imaging can potentially show behavior that appears like circadian rhythms in rare instances, some false negatives are unavoidable without filtering out legitimate oscillations. False positives were more common with smaller vesicles for a few potential reasons. The first is that they contain a lower signal due to the smaller volumes, and thus fewer fluorescent molecules. The second is that smaller vesicles may be more significantly affected by autofocus variations in z plane, as small shifts could mean moving a much more significant portion of the vesicle out of the optimal focal plane. The third reason could be the alignment algorithm used to correct for position drifts from lateral stage movement inaccuracies may bias alignment of larger vesicles as they represent larger portions of the image to be aligned to corrected. In addition, smaller vesicles again would be more significantly impacted as shifts in the lateral plane would be proportionally larger in small vesicles. In any case the false negative is low enough where its impact is not significant. In future work, the first reason can be counteracted by a higher concentration of fluorescent molecules and the third can be counteracted using an individual tracking routine, although that would likely greatly increase computational time.

Table 6. False negative rates from FFT analysis of KaiC- negative control

Vesicle Diameter (μm)	Sample Size (#)	False negatives (#)	False Negative (%)
3	531	18	3%
4	398	13	3%
6	155	1	<1%
8	69	1	1%

Fig. 3.14A shows the clock fidelity of the vesicles as a function of loading concentration, with each line (various colors) representing vesicle diameter size groups from 3 μm to 10 μm. Here there is a clear trend of clock fidelity monotonically increasing with loading concentration across all vesicle sizes. In **Chapter 2.3.2**, the protein encapsulation using OSM-PAPYRUS showed cell-like variation in encapsulated protein concentrations, so in context of these results it appears that greater loading concentrations can buffer against the effect of cellular variation. Recall, that the 1× concentration is the typical concentration used for in vitro investigations of the core oscillator of the cyanobacterial circadian clock. Within this minimal cell vesicle model, at the same 1× concentration the cell-sized 3 μm vesicles reveals that only ~30% of the clocks were functional. A supermajority of 70% of the population could not reproduce the clock oscillation, a much lower success rate than expected for key cellular systems. The native cyanobacteria contain significantly greater than 1× clock protein concentrations, expressing the clock proteins at approximately 2.5× concentrations (103, 135). In **Fig. 3.14A**, at the 2.5× or cellular concentration of clock proteins, the clock fidelity is significantly increased so that ~70% of the clock vesicles oscillate. Although this is

not quite at the near 100% levels of functionality expected in biological cells, this brings the fidelity significantly closer. Additional mechanisms in the cyanobacteria that may further regulate and support clock fidelity further will be discussed later in the chapter.

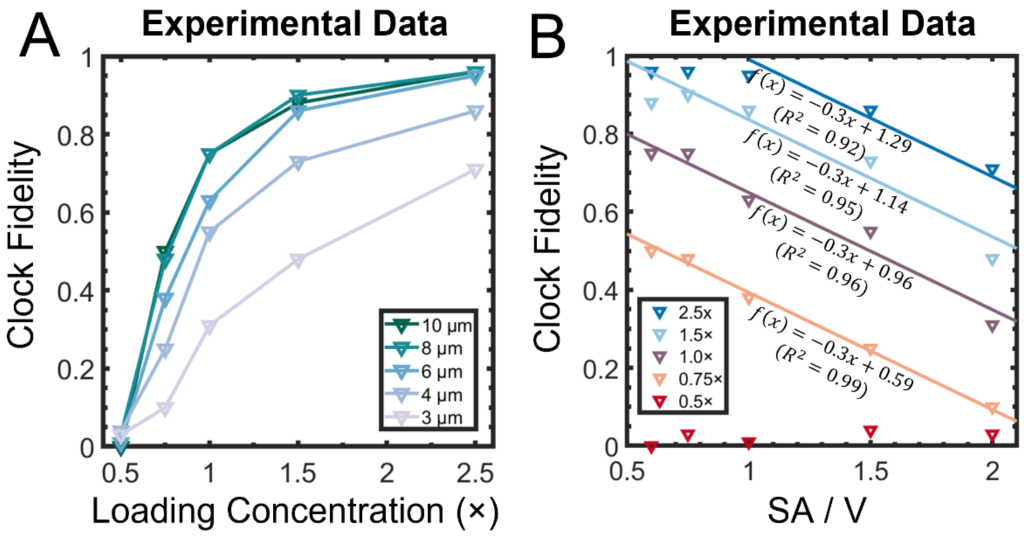

Fig. 3.14. Single vesicle analysis of clock fidelity shows concentration, size, and surface area over volume dependency. (A) Single vesicle analysis shows the clock fidelity as a function of protein loading concentration (0.5× to 2.5×) across varying clock vesicle sizes (Ø: 3 µm to 10 µm). Colors represent vesicle size. **(B)** Single vesicle analysis showing clock fidelity as a function of the surface area to volume ratio (SA/V) across varying loading concentrations. Highlights the linear relationships (colored lines) between clock fidelity and the SA/V ratio, which suggests membrane related behaviors are present. Equation for linear regression and R^2 values are included below each fit. Colors represent protein loading concentration.

Clock fidelity also showed a positive correlation with larger vesicle sizes as well as concentration in **Fig. 3.14A**. When the clock fidelity is plotted as a function of the surface area to volume ratio (SA/V) in **Fig. 3.14B**, a linear relationship between greater clock fidelity and a lower SA/V ratio is observed. This suggests the size dependence is likely due to a membrane related phenomenon, such as membrane binding of one or more protein species. In the native cyanobacteria, the KaiB protein has been shown to localize to the poles of cyanobacteria (136). If membrane binding is occuring, then the number of proteins bound should be a function of the surface area. Since the volume increases faster than surface area as vesicle size increases, smaller volumes would mean a greater proportion of clock proteins will be bound to the membrane. This can reduce free protein concentrations that are avaliable for the clock to function efficiently. **Fig. 3.14B** shows that as the SA/V ratio increases (smaller sized vesicles) the clock fidelity drops linearly, likely indicating that protein binding to the membrane is the likely hypothesis to the size modulation of clock fidelity.

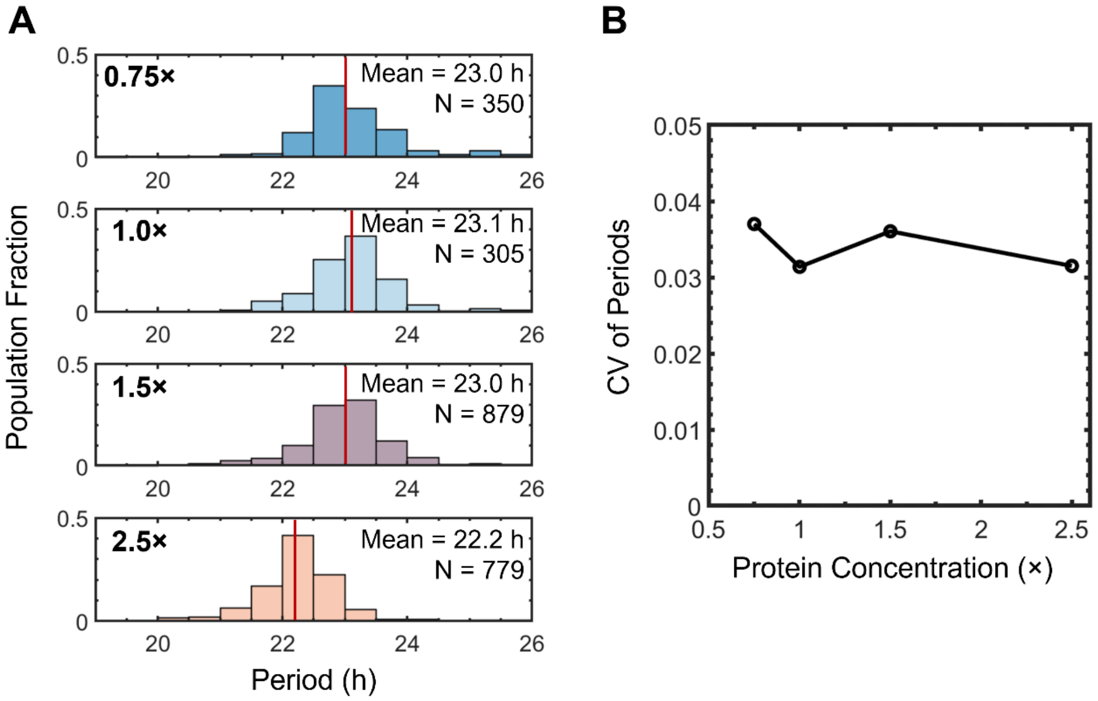

Fig. 3.15. Clock produces highly consistent periods across expression levels and under intercellular variation. (A) Period histograms of oscillating vesicles aggregating vesicles from all analyzed diameter size groups (3 μm, 4 μm, 6 μm, 8 μm, & 10 μm, all ±0.5 μm) across various protein loading concentrations (0.75×, 1.0×, 1.5× & 2.5×). The red line shows the mean period for each distribution. **(B)** Coefficient of variation (CV) of period distribution is plotted again the protein loading concentration.

Fig. 3.15A shows a histogram aggregating the period of oscillation from all individual vesicles analyzed from each protein loading concentrations. **Fig. 3.15B** plots the CV of the period distributions as a function of protein loading concentration. The mean period of oscillation remained extremely consistent from 0.75× to 1.5× even under confinement in the limited volume inside the vesicles and combined with cell-like variation of protein species (see **2.3.2**). An increase in the period is only observed when the protein concentration is increased to 2.5×. Recall in **Fig. 3.11** the amplitude of the circadian rhythm reached a maximum of ~0.2 at 1.5×, and **Table 5** shows the calculation of the peak proportion of KaiB in a KaiBC complex to be at 100% at 1.5× concentrations and above. So, the only time when period shortens is when concentration increases after the point all KaiB complexes are formed. This fits with the hypothesis that the increase in period seen here is because the KaiA-induced KaiC phosphorylation rate continues to increase with concentration with no limit, while the opposing increase in KaiA sequestration sites on KaiBC stop increasing once KaiBC formation is maximized at and above 1.5× concentrations and cannot compensate for the increased phosphorylation speed. The reaction can still run because there are still more than enough KaiA sequestration sites, as KaiA binds with a 12:6:6 KaiA:KaiB:KaiC monomer ratio, but the sequestration rate can no longer keep up with the phosphorylation rate. Ultimately even at 2.5× concentrations, the shortening in the mean period is less than 1 hour. The CV of the period in **Fig. 3.15B** also remains very consistent, which was initially surprising given the cell-like variation of protein concentrations and confinement inside vesicles. It appears the core oscillator can only produce near circadian oscillations or fail to oscillate completely. This suggest the core oscillator is a highly specific system that is "programmed" to specifically tick a circadian pace, and perhaps this is one reason why the clock can remain so well synchronized across population of cyanobacteria over week to month long timeframes (90, 134, 137–139). This may make the clock seem extremely rigid and unable to adapt to changes in environment such as the length of the day, however, only the core oscillator of the clock is evaluated here. It can be considered almost as the quartz crystal of a clock, which provides a precise frequency, but the operator can adjust the time through other means. In the cyanobacteria circadian clock, there are other mechanisms such as transcriptional translational feedback (TTFL) (123, 124), and complementary proteins including CikA and SasA (120–122). These other components of the full clock can play the role of fine tuning, supporting the clock fidelity, or even altering the clock timing based on environmental cues.

In summary, the partitioning of the clock reaction into cell mimetic vesicles has significant impact on the behavior of the clock and show how cellular properties such as intercellular variation and membrane interactions can significant change how a cellular system behaves. This highlights the large gap between in vitro studies and in vivo behaviors, here the cell mimetic vesicle model can bridge some of those gaps and provide insight into the behaviors of the core oscillator of the clock in a system to approaches closer to the cell environment. Two hypotheses were proposed from the data in **Fig. 3.15**, first, higher protein concentrations are necessary to buffer against the effect of intercellular variation, and second, membrane binding reduces free KaiB concentration causing size dependency.

3.3.5 Modeling the clock vesicle behaviors with the clock fidelity model.

To validate the hypotheses that intercellular variation and membrane binding are responsible for causing the clock fidelity trends seen in **Fig. 3.14** and to explain the behavior of the clock in vesicles, a minimal model that incorporates these hypotheses will be tested. The limitation of the clock has been well studied in bulk in vitro experiments from experiments performed here and in literature (103, 134, 137, 152). In **Fig. 3.11A** bulk in vitro experiments had shown that there is a minimal total concentration of clock protein necessary ensure the clock can be driven forward. From there, the minimal concentration was determined to be >0.5× for sustained oscillations. If the total concentration of the proteins falls below the minimal levels, **Fig. 3.12** shows that the KaiA driven phosphorylation could become slower than the intrinsic KaiC auto-dephosphorylation and prevent the cycle from being driven forward. In literature, in vitro experiments have shown that protein stoichiometry is also a key condition for sustained oscillations of the clock (103, 134, 137, 152). The data from these papers were collected and compared with one another to determine a set of limiting conditions that can determine what stoichiometric conditions will support sustained clock oscillations. KaiA is reported to support sustained oscillations when KaiA ranges from ~0.6 to 3.6 μM, when KaiB and KaiC are kept constant at 3.5 μM (1×), from bulk experiments measuring the KaiC phosphorylation levels (103, 152), KaiBC association with anisotropy (134), and with computation modeling (137). While KaiB is reports sustained oscillations are supported when KaiB concentration ranges from ~1.75 μM to >18 μM, while KaiA is kept constant at 1.2 μM (1×) and KaiC is kept constant at 3.5 μM (1×), from bulk experiments measuring the KaiC phosphorylation (103, 152) and KaiB-KaiC association (134). No maximum KaiB concentration was found in these reports. The aforenoted literature reports showed a consensus for the stated protein conditions that supported sustained oscillations.

A minimal model is built that enforces these well-established limiting conditions from literature reports and bulk data shown previously in **Fig. 3.11A**. Using the data from literature reports, a limiting ratio of KaiA to KaiC that supports sustained oscillations is set to be ≥0.17, and a maximum ratio of KaiA to KaiC was set to be ≤1.03. A limiting ratio of KaiB to KaiC was set to be ≥0.5, with no maximum ratio of KaiB to KaiC. Then based on previously discussed bulk experiments (**Fig. 3.11A**), a limiting concentration of >0.6 μM KaiA, >1.75 μM KaiB, and >1.75 μM KaiC was set. These limiting conditions are summarized in **Table 7**.

Table 7. Limiting ratio and concentration of clock proteins required for sustained oscillations used for the clock fidelity model.

KaiA:KaiC Limiting Ratio	KaiB:KaiC Limiting Ratio	KaiA Limiting Concentration	KaiB Limiting Concentration	KaiC Limiting Concentration
≥0.17 & ≤1.03	≥0.5	>0.6 μM	>1.75 μM	>1.75 μM

3.3.5.1 Introducing cell-like variation to clock fidelity model

Previously, in **Chapter 2.3.3**, it was shown that distribution of encapsulated proteins concentrations did not vary with size (**Fig. 2.13**) and the encapsulated proteins followed a gamma distribution for the population (**Fig. 2.14**). It was also shown by **Fig. 2.15** that the mean of encapsulated protein concentrations is expected to be equal to the loading concentration and the variation remains constant at a CV of ~0.3. Knowing these expected parameters for the encapsulation statistics, 5000 vesicles are simulated, each containing some concentration of KaiA, KaiB, and KaiC independently and randomly assigned by sampling from a corresponding gamma distribution (**Fig. 3.16**). The parameters (k, θ) of the gamma distribution can be determined with a known CV and mean concentrations using $k = \frac{1}{CV^2}$ from **Eq. 9** and $\theta = \mu CV^2$ from **Eq. 10**. The limiting conditions are then applied from **Table 7** and a vesicle will be considered oscillating only if all the conditions are met.

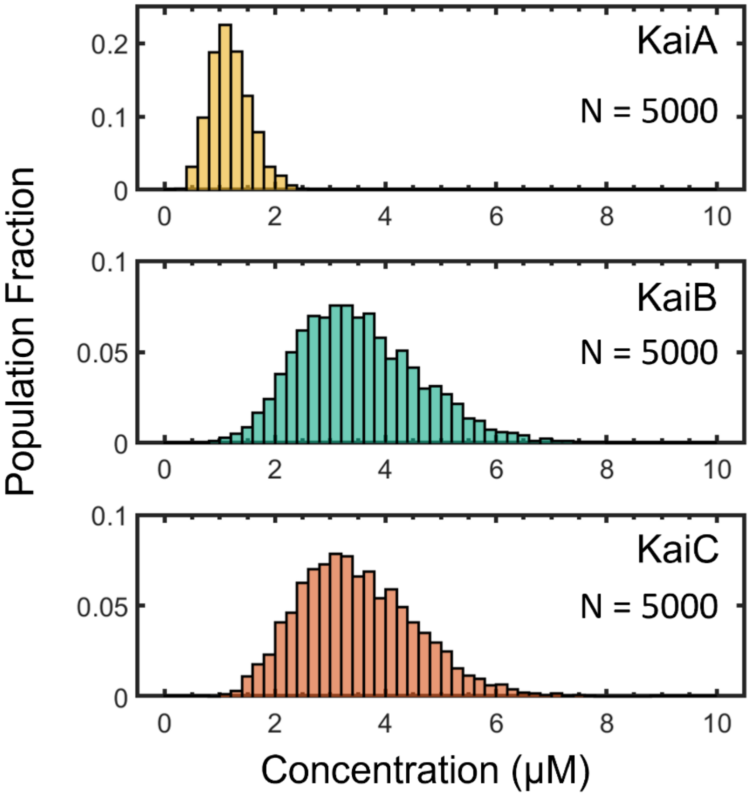

Fig. 3.16. Clock fidelity model distributions KaiA, KaiB, and KaiC proteins following a gamma distribution. N = 5000 vesicles are encapsulated with KaiA, KaiB and KaiC. The gamma distribution parameters (k, θ) are determined using a CV of 0.31 and mean equal to the loading concentration. Here the distribution for the 1× protein concentration is shown. Parameters are as follows for KaiA (k = 10.41, θ = 0.12), KaiB (k = 10.41, θ = 0.34), and KaiC (k = 10.41, θ = 0.34) gamma distributions.

Fig. 3.17 shows the clock fidelity as a function of protein loading concentration for the model, which only incorporates the variation of protein concentrations. The general trend of increasing clock fidelity when loading concentration increases can be seen, however, the trend with vesicle size is not represented, and all sizes show the same clock fidelity. This suggests the cell-like variation can hamper clock fidelity in a population, but it can be buffered by using higher loading concentrations to achieve greater clock fidelity. However, this still doesn't explain where the size differences in fidelity arise from. In **Fig. 3.14B** it was shown that clock fidelity was also linearly correlated to the SA/V ratio, when the amount of avaliable surface area was relatively high compared to the volume it contains, the clock fidelity dropped. This strongly suggests that a process such as membrane binding reduces free protein concentrations within the vesicle lumen, indicated by the linear correlation to the SA/V ratio.

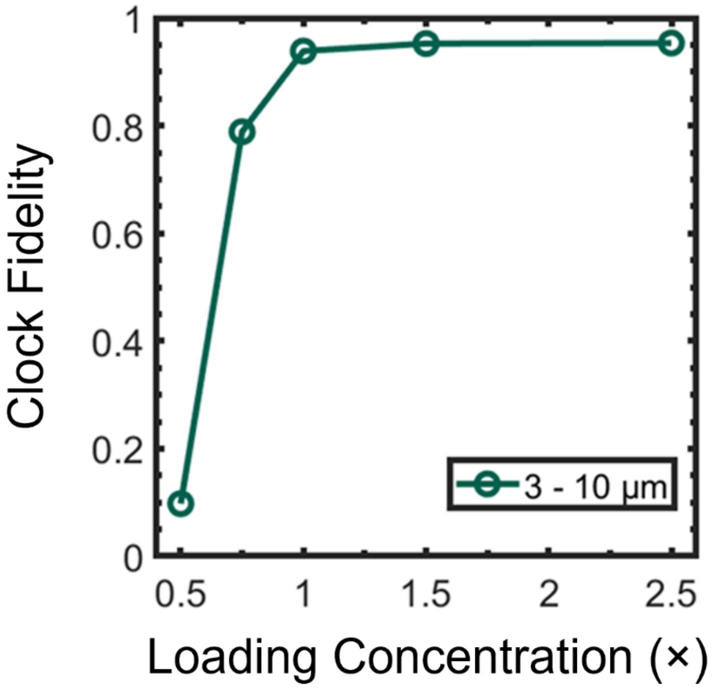

Fig. 3.17. Clock fidelity model incorporating only intercellular variation. Simulated clock fidelity (function clocks/total clocks) as a function of loading concentration for vesicles sized 3 to 10 μm in diameter (green). There are no differences in simulated clock fidelity between vesicle sizes. Only the effect of intercellular variation is applied to the model and checked against limiting conditions.

3.3.5.2 Membrane binding observations and introduction to clock fidelity model

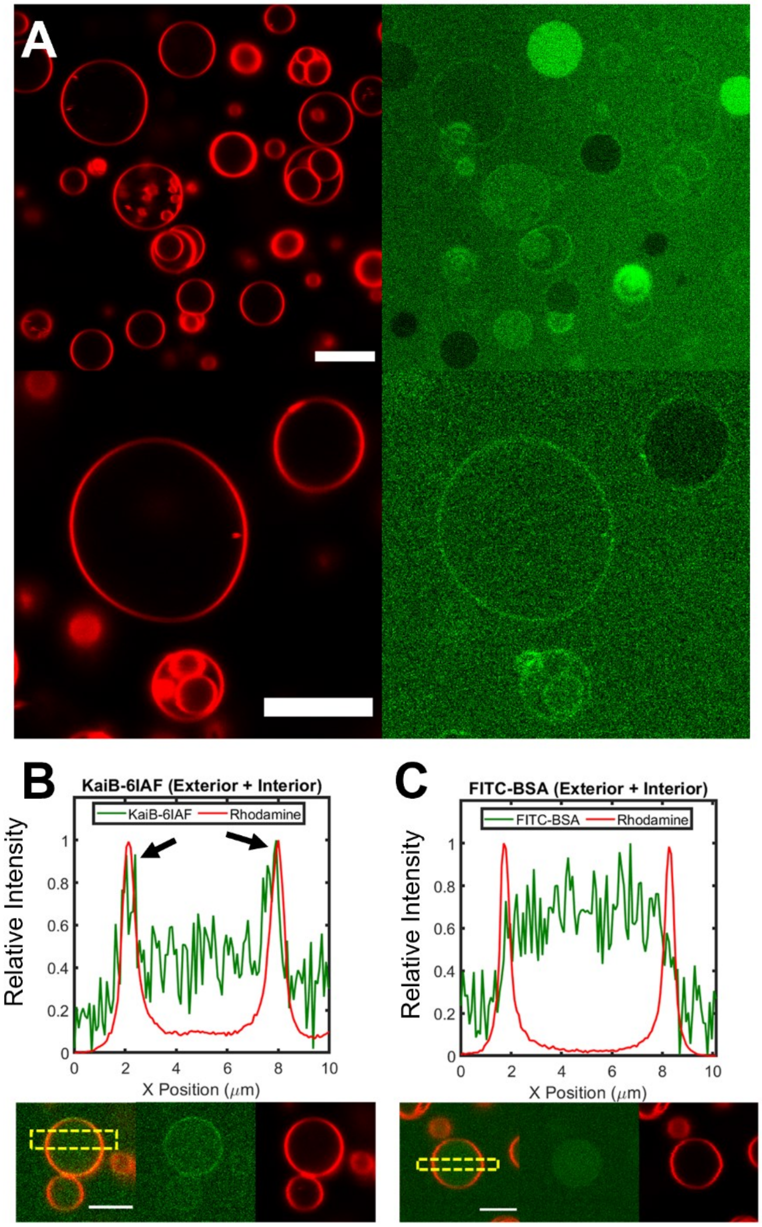

Fig. 3.18. KaiB membrane binding can be seen in confocal images. All confocal images taken using a 63× 1.4 NA oil objective. **(A)** Confocal images of vesicles (red, left) encapsulated with only 1.75 μM KaiB-6IAF (green, right) show evidence of membrane binding forming a localized bright ring around the membrane. **(B)** A line profile for the intensity of KaiB-6IAF (green) and the rhodamine labeled membrane (red) of a selected vesicle encapsulated with KaiB-6IAF highlights the spike in intensity of the KaiB-6IAF at the membrane (black arrows). **(C)** A line profile for the intensity of FITC-BSA (green) and rhodamine labeled membrane (red) of a selected vesicle encapsulated with FITC-BSA does not show any membrane binding. All scale bars are 5 μm.

Membrane binding of Kai proteins have been demonstrated in literature for live cyanobacteria (136) and membrane fraction of whole cell extracts (111), showing KaiB and KaiC may localize or colocalize to the membrane. Confocal images of vesicles encapsulated with only 1.75 µM KaiB-6IAF in **Fig. 3.18A** show evidence of KaiB membrane binding. A bright ring can be seen in the KaiB-6IAF channel (green) in the region where the membrane (red) is located, suggesting KaiB-6IAF is localizing to the membrane. **Fig. 3.18B** further demonstrates the membrane binding with a line profile showing a spike in the KaiB-6IAF intensity (green) at the membrane location (red) shown by the black arrows. In **Fig. 3.18C** a similar line profile is performed for a vesicle encapsulating FITC-BSA, which is not known to associate to phospholipid membranes, shows no similar FITC-BSA intensity (green) spike at the membrane location (red). This shows the ring formed by the KaiB-6IAF is specific to the KaiB protein and rules out bleed-through from the rhodamine channel. Both FITC-BSA and KaiB-6IAF are fluorescently conjugated with fluorescein.

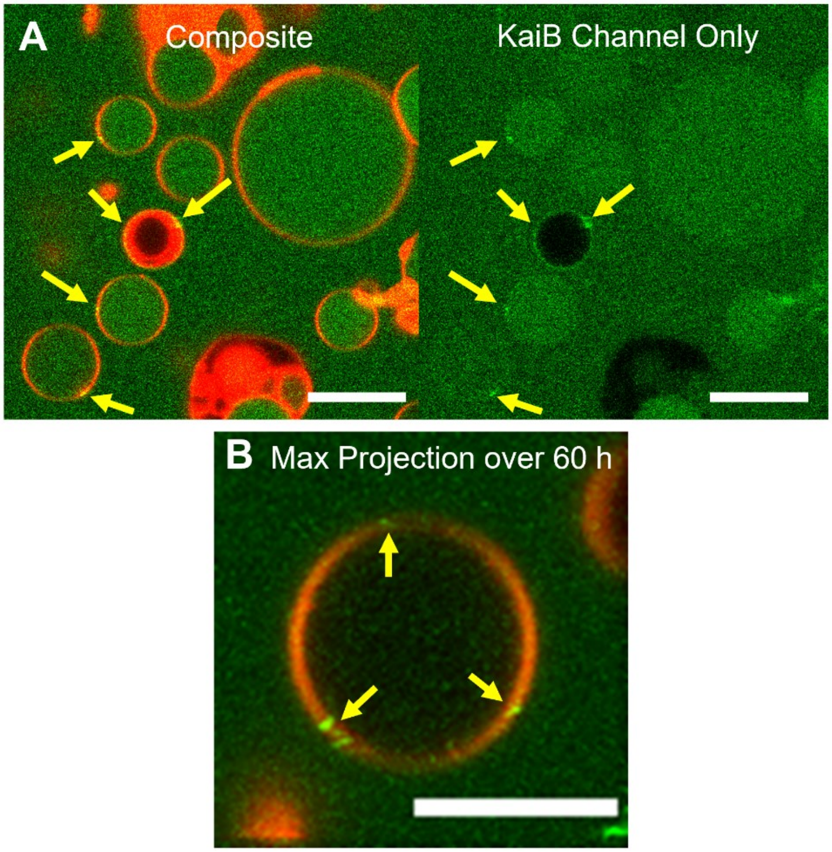

Fig. 3.19. Puncta forms when the KaiABC clock is encapsulated. (A) Composite image (left) of vesicle membranes (red) and KaiB-6IAF (green), and KaiB-6IAF only channel (right). Yellow arrows point to the formation of puncta on the vesicle membrane. Scale bar: 10 µm. **(B)** A max intensity projection of a time series of 60 h shows the puncta remains localized on the membrane. However, the puncta (yellow arrows) may move in and out of the axial field of focus. Scale bar: 5 µm.

Interestingly, when the clock is encapsulated (KaiA, KaiB and KaiC) in **Fig. 3.19A**, puncta are seen to occur on the vesicle membrane instead of being evenly distributed around the membrane. **Fig. 3.19B** shows a maximum intensity projection of a timeseries over 60 hours, which shows the puncta remains localized to the membrane. Unfortunately, the puncta do not remain in place because it can laterally diffuse within the membrane with lipids. And because a thin slicing thickness is obtained from the 60× 1.4NA objective, the puncta can diffuse out of the axial field of focus, and it cannot be determined whether the puncta remain on the membrane and diffuses around or if it disappears and reforms according to the circadian rhythm. The images confirm the puncta are, at least in part, composed of KaiB-6IAF, but because only KaiB-6IAF is labeled, it does not reveal if the other clock proteins colocalized with KaiB. KaiB by itself appears to be uniformly distributed in the membrane but appears to prefer to form puncta instead when it is with KaiA and KaiC, suggesting that colocalization of KaiB with KaiA and/or KaiC is occuring and causes local aggregation of membrane bound protein into puncta.

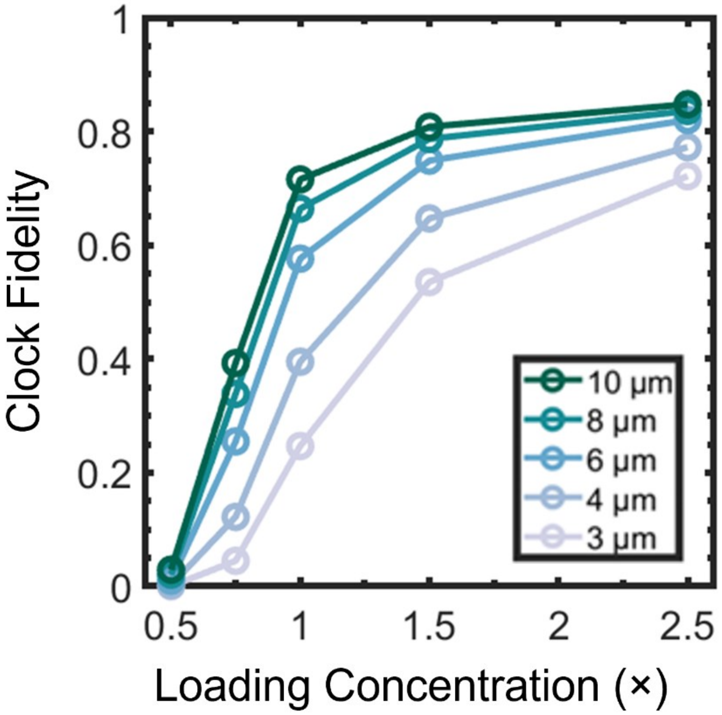

Fig. 3.20. Clock fidelity model incorporating cell-like variation and membrane binding. Trend of clock fidelity when both cell-like variation and membrane binding (b = 650 KaiB molecule per μm^2 membrane area) as a function of loading concentration. Various diameter sizes classes (width: ±0.5 μm) from 3 μm to 10 μm (multiple colors) are shown.

Now that evidence of KaiB binding (and potentially the other Kai proteins) is shown, let's see what happens when the membrane binding is incorporated into the clock model. Here, it is assumed that KaiB will bind a constant number of molecules per μm^2 of membrane area. To model KaiB membrane localization we use an estimate of 650 KaiB monomers bound per μm^2 of surface area of the vesicle and consider bound monomers to not participate in the reaction, thus reducing free KaiB concentration. In the cell this number ranges from ~447 to 715 of KaiB monomers bound per μm^2 of surface area assuming two concentric membranes (111, 136, 150), so the estimate used in the model is similar to cellular levels. It has been suggested that the Kai proteins localize to the thylakoid membrane (136) where the light reactions of oxygenic photosynthesis occur (159).

In **Fig. 3.20** the clock fidelity model is shown with both cell-like variation and membrane binding. The clock fidelity model is now closely following the trends for both loading concentration and vesicle size seen in the experimental data (**Fig. 3.14A**). As was observed in the experimental data, when diameters greater than 8 μm will only have a minor impact on clock fidelity. This is because the differences between the SA/V ratios become smaller as size increases and becomes less impactful in affecting the proportion of protein bound. This model validates the hypotheses that cell-like variation is likely driving the trends in clock fidelity with concentration and that the membrane binding drives the clock fidelity trend with vesicle sizes.

3.3.5.3 Final clock fidelity model: Addition of protein co-encapsulation factors

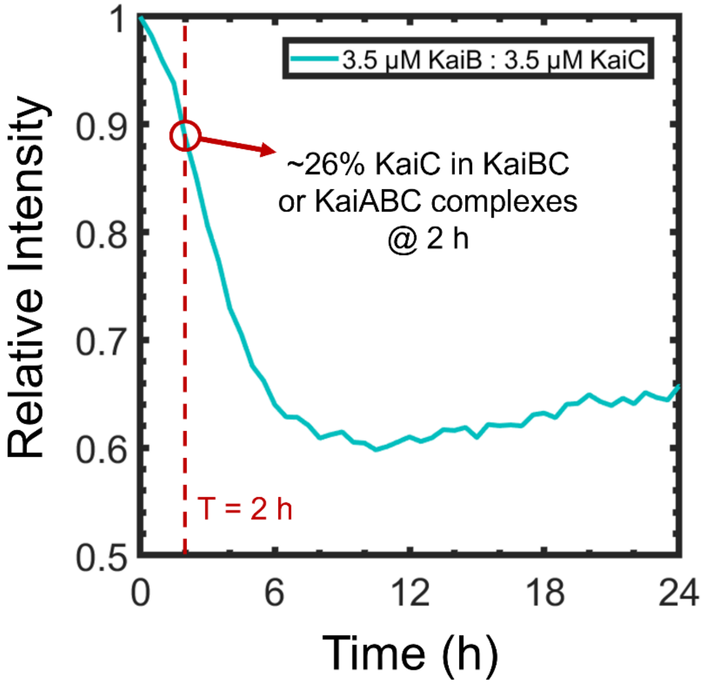

Fig. 3.21. KaiB and KaiC kinetic binding studies show the estimated fraction of complexes formed during vesicle assembly and loading. The binding of KaiB (3.5 µM) and KaiC (3.5 µM) shown by the relative intensity (intensity/initial intensity) is plotted over time since the protein reaction is made. A red dotted line denotes the 2 hours it takes for the assembly and loading of proteins, where approximately 26% of KaiC are in KaiBC complexes.

There is still another factor to account for in the model because the preparation and loading of vesicles for OSM-PAPYRUS lasts about 2 hours, and the clock proteins are expected to continue to oscillate during this time, then at least some of the proteins are expected to form KaiBC or KaiABC complexes together and become co-encapsulated. This co-encapsulation process should effectively reduce the relative variation of protein concentrations encapsulated. To determine what level of co-encapsulation is occuring and whether how the clock fidelity model is affected, a kinetic KaiB:KaiC binding assay is performed at a 1:1 ratio, shown in **Fig. 3.21**, where it is estimated that ~26% of KaiC are in a KaiBC or KaiABC complex during the 2 hours it takes to assemble and load the vesicles. Because loading occurs throughout the 2-hour timespan, a value of 13% of total KaiC is used as the average number of complexes co-encapsulated through the assembly and loading. It is assumed that these complexes will have both KaiB and KaiA bound in a KaiABC complex with a KaiA:KaiB:KaiC monomer binding ratio of 2:1:1 (from 12:6:6) (129, 151). To incorporate this into the clock fidelity model, a new protein species, KaiABC is introduced with a mean concentration representing 13% of the KaiC that formed complexes. The associated KaiA and KaiB in the complex is subtracted from the mean of free KaiA and free KaiB according to the stated binding ratios, prior to forming the gamma distributions. So now four gamma distributions will be created, KaiA, KaiB, KaiC, and KaiABC. After vesicles are distributed with all four protein species, the KaiABC complex is broken down and added back into the KaiA, KaiB, and KaiC according to the aforementioned binding ratios. **Fig. 3.22A** shows the finalized clock fidelity model that incorporates the cell-like variation, membrane binding, and the expected co-encapsulation. The addition of co-encapsulate makes the model very closely reproduce the observed experimental data (**Fig. 3.22B**).

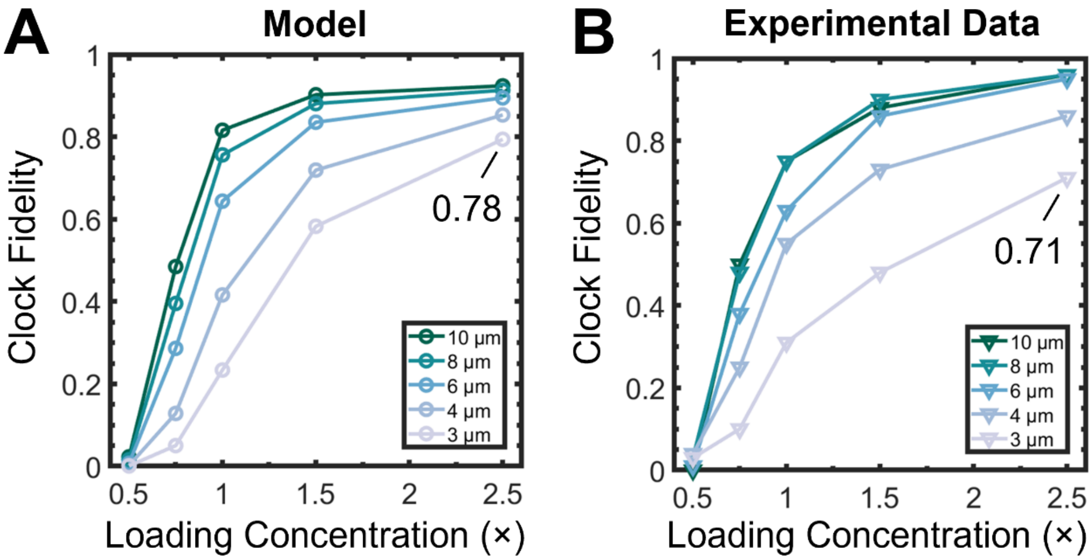

Fig. 3.22. Finalized clock fidelity model incorporating cell-like variation, membrane binding, and co-encapsulation/co-expression. Clock fidelity at cellular conditions (3 μm Ø, 2.5×) are indicated. **(A)** Clock fidelity for the final model is plotted against loading concentration for vesicle sizes from 3 to 10 μm (various colors). The final model very closely reproduces observed experimental data. **(B)** Clock fidelity for experimental data is shown here for reference.

3.3.6 Insights into clock fidelity in vivo: Extending the clock fidelity model

3.3.6.1 Clock fidelity when extending to higher clock protein concentrations

In the native cyanobacteria the clocks are expected to function at nearly perfect fidelity (124, 160, 161) otherwise it will be highly disadvantaged in its survival if it loses the ability to predict the day-night cycle. But clock fidelity at cellular conditions (3 µm Ø, 2.5×) in the experimental data only reached a clock fidelity of ~0.71 and similarly in the clock model, a clock fidelity of ~0.78. Would further increasing the concentration in the model show near 100% fidelity? **Fig. 3.23** shows the model prediction even when loading concentration is increased to 5× still falls short of 100% fidelity, reaching ~0.94. Further increases in concentration seems to hit a limit in the maximum clock fidelity, because due to the cell-like variation in protein concentrations, there are always some cases where the stiochiometry of proteins will be outside the conditions necessary to oscillate.

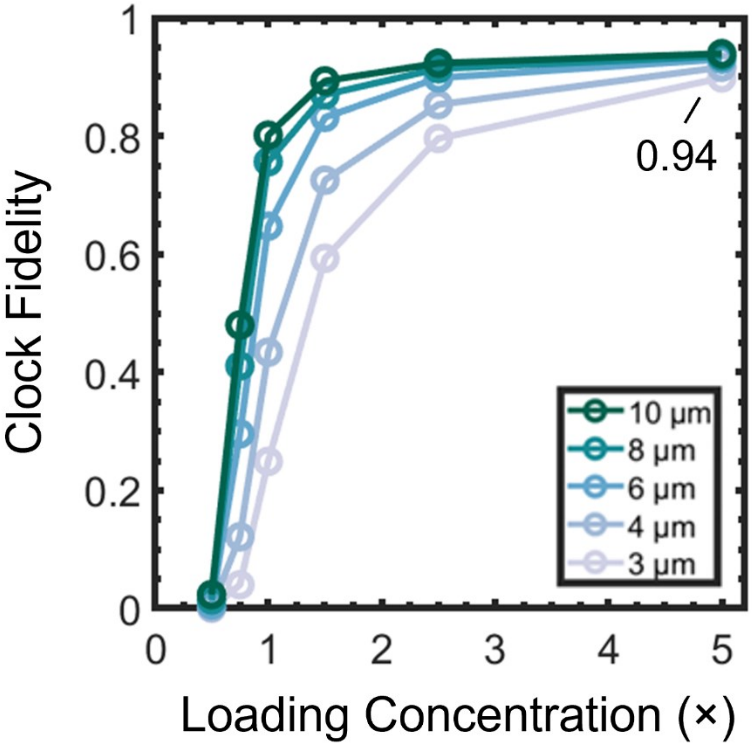

Fig. 3.23. Model: Higher concentration does not meet in vivo levels of clock fidelity. The clock fidelity model is extended to a hypothetical 5× protein concentration. Further increases in concentration do not allow the model to show near 100% fidelity. Clock fidelity of at cellular conditions (3 µm Ø, 2.5×) is indicated.

3.3.6.2 Clock fidelity as a function of varying coefficients of variation

Using the model, different parameters can be tested in ways that can be analogous to known systems in the cyanobacteria. First let us observe what happens if the variation is varied, from no variation at all (CV = 0), to greater variations than is expected in the cell (CV = 1.0) in **Fig. 3.24**. When no variation exists (CV = 0%) then the system will either always function (fidelity = 100%) or never function (fidelity = 0%) as long if it meets some concentration threshold for a given vesicle size. When the CV is low, at values of 0 % to 10 %, vesicles at the cellular condition (3 µm Ø, 2.5× concentration) are expected to oscillate with a near 100% clock fidelity. When CV is increased further to 50% to 100%, the clock fidelity is further negatively impacted, dropping to 0.63 and 0.29 respectively. Overall, this shows greater CVs monotonically hampers clock fidelity, and confirms increases in concentration is one tool a cell could use to counteract the effects of variation. But while higher concentration can improve fidelity, it cannot completely counteract the effect of variation. So, what other tools does the cyanobacteria have that may counter the unavoidable variation of clock proteins?

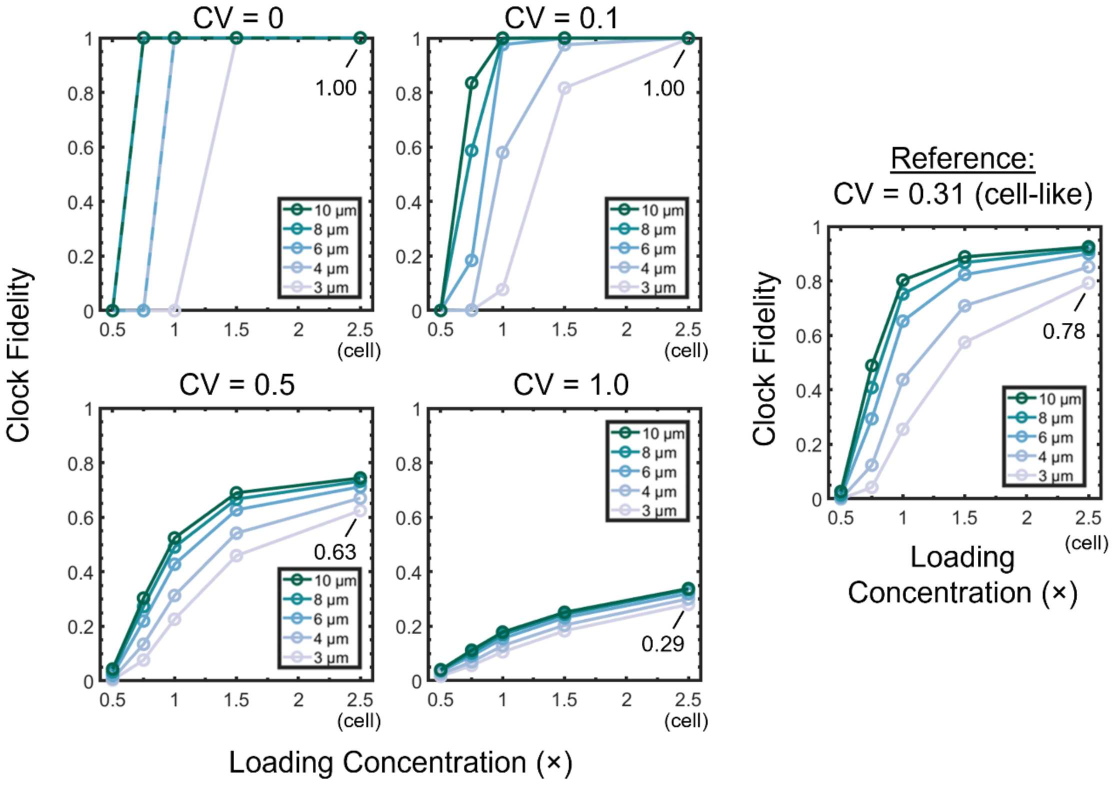

Fig. 3.24. Model: Greater coefficient of variation hampers circadian clock fidelity. The coefficient of variation (CV) is varied in the model to explore how clock fidelity is affected. Greater CV reduce clock fidelity. Clock fidelity (3 µm Ø, 2.5×) at cellular conditions are indicated. A reference fidelity plot (rightmost) shows the model representing experimental system.

3.3.6.3 Co-expression factors can improve clock fidelity

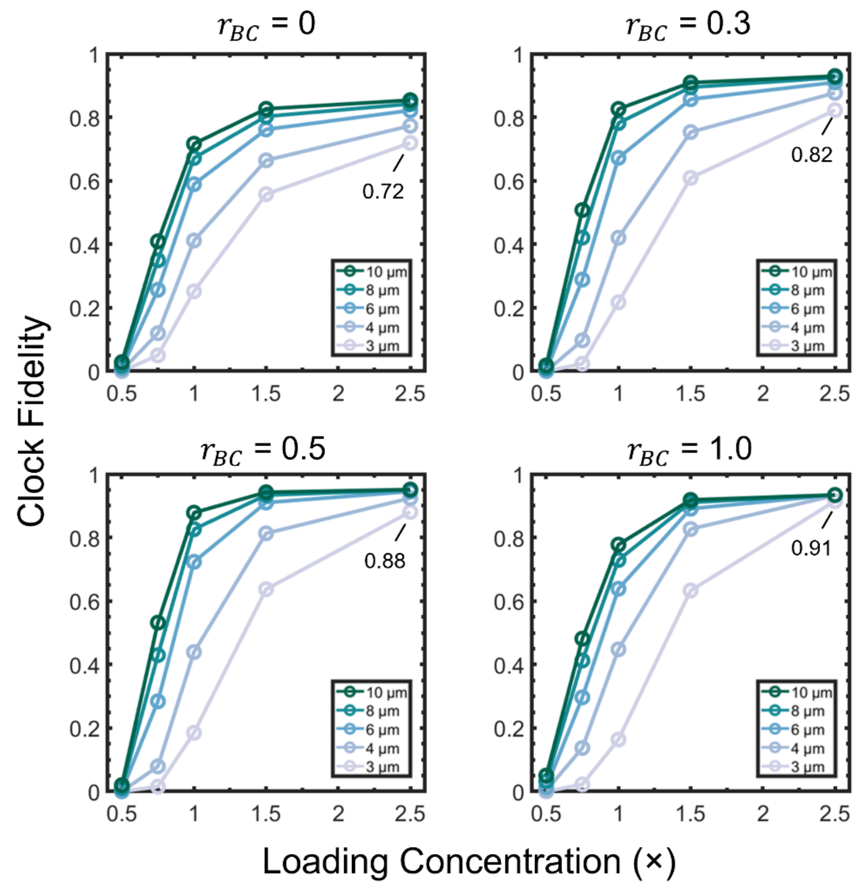

Fig. 3.25. Model: Co-expression factors (r_{BC}) can improve clock fidelity to a degree. In the model a co-expression factor ($\boldsymbol{r_{BC}}$) is incorporated for KaiB and KaiC, so that a $\boldsymbol{r_{BC}}$ of 1 means KaiB and KaiC are perfectly correlated. Co-expression is an analogous representation of the shared promoters of KaiB and KaiC in the cyanobacteria. Clock fidelity (3 μm diameter, 2.5×) at cellular conditions are indicated.

The *kaiBC* promoter is known to be shared by KaiB and KaiC, and it controls the transcription of both genes (104, 117, 162). The promoter for KaiA is separate and is regulated independently (117, 118). If a KaiB & KaiC co-expression factor (r_{BC}) is introduced to the system, would the clock fidelity improve? The co-encapsulation factor introduced earlier is analogous to the co-expression factor. Because only KaiB and KaiC share a common promoter, the co-encapsulation factor is applied for KaiB and KaiC only, so only a KaiBC species is introduced in place of the KaiABC species, with a binding ratio of 1:1 for KaiB to KaiC. The co-expression factor (r_{BC}) is a scalar that determines what level the expression of KaiB and KaiC is correlated with one another, a r_{BC} of 1 would mean there is perfect correlation between the concentration of KaiB and KaiC. In the perfect correlation case, if

KaiB concentration is 3.5 μM then KaiC concentration is also 3.5 μM. In **Fig. 3.25**, the clock model shows as the r_{BC} increases, the clock fidelity also increases, showing that co-expression can reduce variation between protein species and have a greater chance for the clock to be functional. However, because KaiA does not share a common promoter, the variation of KaiA in respect to KaiB and KaiC will mean the clock fidelity will still only show clock fidelity that do not reach ~100% levels.

3.3.6.4 Role of SasA and CikA from the full circadian clock

Other elements from the full circadian clock, such as the input-output sensor histidine kinase, *Synechococcus* adaptive sensor A (SasA) (121), and the circadian input kinase A (CikA) (122) can interact with the Kai clock proteins, and have been shown to competitively bind to KaiC (129, 134, 163). Due to this competitively binding, the presence of SasA and CikA can effectively ease the conditions required for clock rhythms. Literature reports show that the presence of 1.0 μM SasA allows clock rhythms to occur even if KaiB drops below a concentration of 1.8 μM, and shows the clock now fails when KaiB reaches 0.9 μM (134). A similar finding has been reported with the presence of 0.9 μM of CikA, which shows the clock remains functional up to a KaiA concentration of 0.3 μM (163). Other Kai protein concentrations are kept constant at their respective 1× concentrations for both reports.

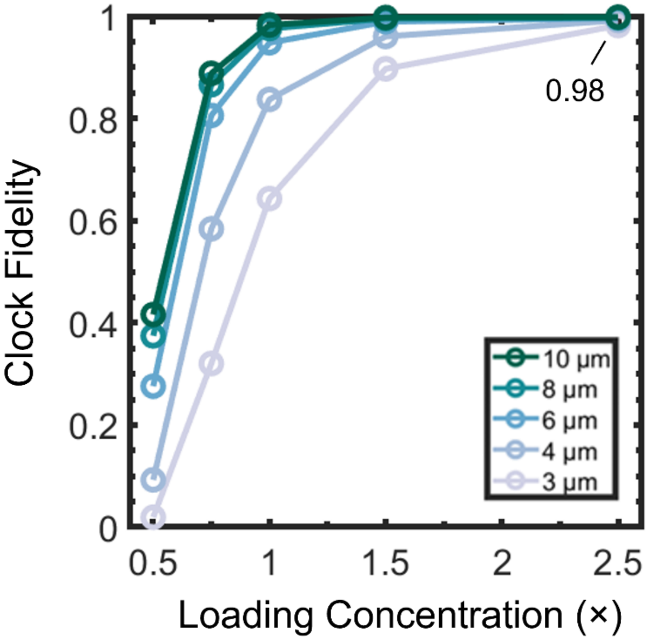

Fig. 3.26. Introduction of SasA and CikA competitive binding into model. The effects of SasA and CikA are introduced to the model by easing the limiting conditions according to data from literature reports. This greatly improves fidelity especially at cellular conditions (3 μm diameter, 2.5× concentration).

The model in **Fig. 3.26** incorporates the effect of SasA and CikA by easing the limiting conditions used to determine whether a clock can show a sustained oscillation, based on the values obtained from literature noted above. The new limiting conditions used for this model are detailed in **Table 8**. With the cooperative effects of SasA and CikA, the clock model now shows that the expected clock fidelity increases significantly. At the cellular condition (3 μm Ø, 2.5×), the expected clock fidelity now reaches 98%, very close to the a near 100% fidelity seen in cells. This highlights how the behavior of other clock components, such as SasA and CikA, can play an important role in regulating the clock when intercellular variation is present. Concentration here remains an important parameter in insuring high clock fidelity even with the cooperative effects of SasA and CikA. There are likely other additional mechanisms that also ensure the clock fidelity in the cell reaches near 100%, such as the transcription-transcriptional feedback loop (TTFL) (104, 123).

Table 8. Limiting conditions when SasA and CikA competitive binding is introduced.

KaiA:KaiC Limiting Ratio	KaiB:KaiC Limiting Ratio	KaiA Limiting Concentration	KaiB Limiting Concentration	KaiC Limiting Concentration
≥0.09 & ≤1.03	≥0.25	>0.3 μM	>0.9 μM	>1.75 μM

3.3.6.5 Period and amplitude simulation

The experimental clock fidelity can be explained very well by the clock model to be primary a function of cell-like variation of protein concentrations and membrane binding. Can the model be extended to other elements such as the period of oscillation? Bulk experiments from a literature report have shown that how the period changes with varying ratio of KaiA and KaiB with a fixed KaiC concentration (134). This allows the determination of how the variation of protein concentration in our simulated vesicles can affect the period. The mean expected period from each protein concentration is obtained from previously shown experimental data (**Fig. 3.11**), and the expected shifts in period according to protein stiochiometry (see **3.2 Materials and Methods**) are applied. The resulting periods generated from the model are shown in **Fig. 3.29A** and compared to experimental periods in **Fig. 3.29B**. The output period is remarkably similar to the experimental data, which further corroborates that the experimental data are driven by intercellular variation and membrane binding. This finding also suggests that the behavior within the clock vesicles in fact do reflect expected behavior of the clock in a bulk in vitro environment, only that the protein stoichiometry and concentrations are varied in the vesicle model due to induced cell-like variation and membrane association of proteins. So, the impact of smaller copy numbers inside the vesicles is not likely to be significant in affecting the circadian oscillation of the core oscillator. This matchs with the hypothesis that size dependent behavior of clock fidelity is not due to changes in copy number but instead membrane binding. Calculations performed on the expected degree of stochastic variation in reaction time, which can be estimated to be on the order of $1/\sqrt{N}$, show even at 3 μm diameter vesicle sizes and 0.5× protein concentrations, the CV should be 1% or less. One key takeaway is that the use of the vesicle to run the reaction allows the confirmation on what elements within the bulk experiments can accurately represent expected behavior of the clock an in vivo enivronment, alleviating concerns on what behaviors would change due to confinement in a limited volume with cell-like copy numbers.

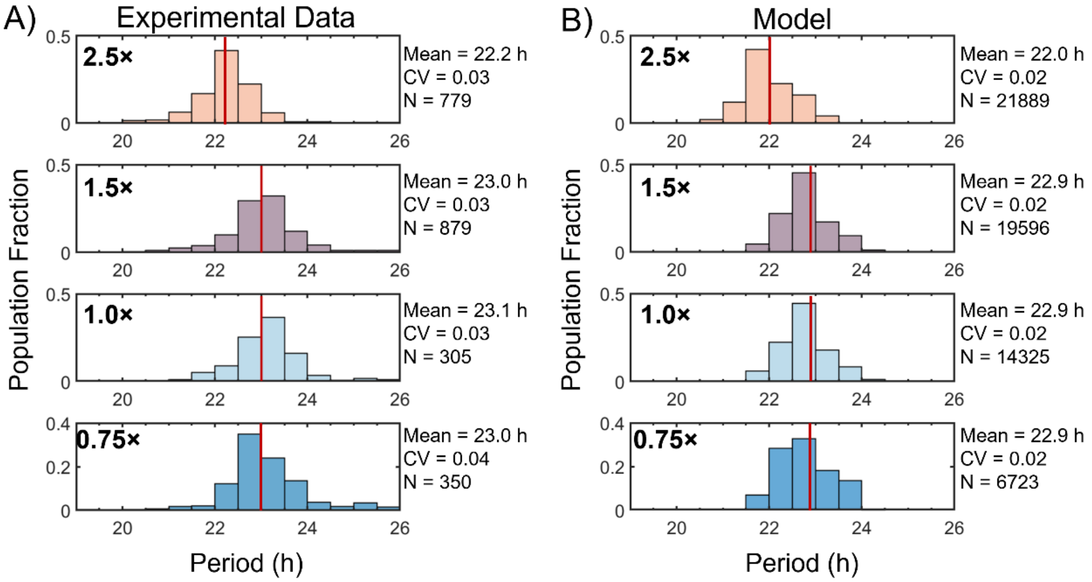

Fig. 3.27. Simulated periods from model compared with experimental data. (A) Period determined from clock model, using known changes in period according to protein stiochiometry. **(B)** Period distributions from experimental data shown for reference. Red lines show the mean period.

Amplitude can be estimated using expected changes in amplitude from protein concentration from literature data (134) (see **3.2 Materials and Methods**). The amplitude from experimental data and model predictions is shown in **Fig. 3.28A&B**. With both the simulated amplitude and period, a simulated trace can be reproduced using a sine wave with the appropriate parameters calculated from the amplitude and period. The experimental traces in **Fig. 3.29A** are compared with the model traces in **Fig. 3.29B**. Here trace is defined as the signal from a vesicle. The mean for all experimental traces (black) and all model traces (red) are shown along with 30 randomly selected traces (gray lines). The model traces closely resemble the experimental traces in both phase cohesion, period, and variations in amplitude.

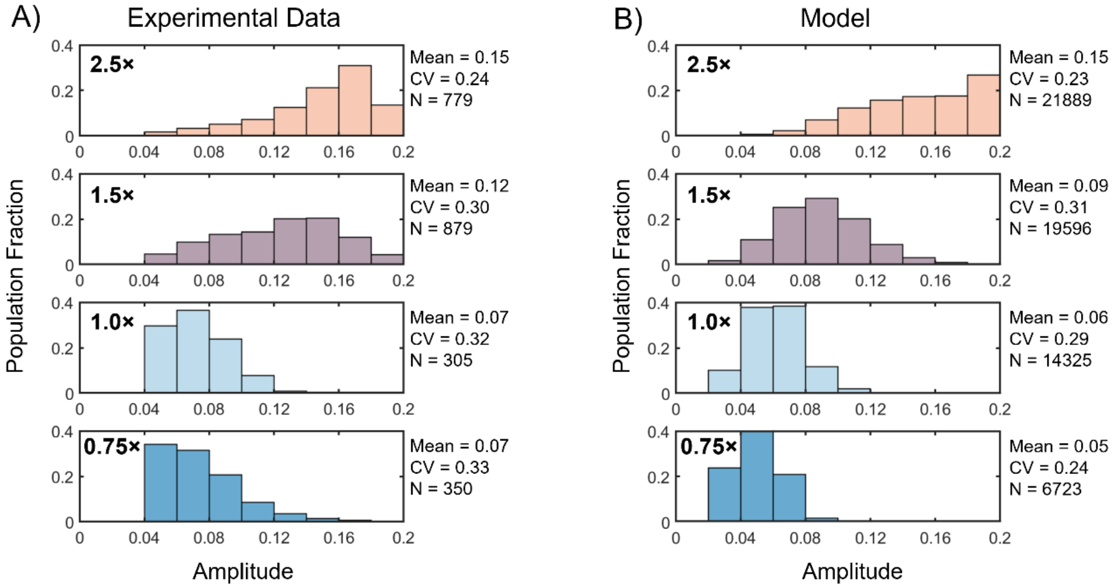

Fig. 3.28. Simulated amplitudes from model compared with experimental data. (A) Amplitude determined from clock model, using known changes in amplitude according to protein concentration. **(B)** Amplitude distributions from experimental data shown for reference.

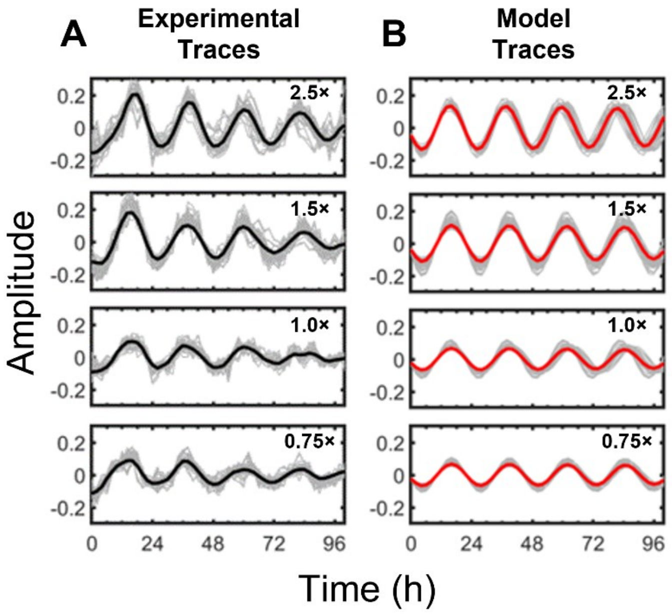

Fig. 3.29. Model produced traces compared to experimental traces. **(A)** The mean experimental traces (black line) for 0.5× to 2.5× protein concentrations, with 30 random traces (gray lines). **(B)** The mean trace produced by the model (red line) for 0.5× to 2.5× protein concentrations, with 30 random traces (gray lines).

3.3.7 Do membrane oscillations suggest rhythmic binding?

An interesting observation was found when observing the intensity of the rhodamine labeled membrane is measured over time in **Fig. 3.30A**. It shows indications of rhythmic oscillations occuring in the intensity of the rhodamine of individual vesicles. For 0.5×, 1.0×, and 1.5× protein concentrations the oscillations are very clear, and the period suggests a near 24-hour circadian rhythm. For 0.75× concentrations, it appears two initial peaks may be there, and for 2.5× concentrations, it is unclear whether oscillations are visible. Membrane oscillations are significantly lower in amplitude (≤0.02) compared with clock oscillations (≤0.2). The FFT analysis to determine the presence of oscillating rhythms was applied, with the requirement for a minimum peak height removed due to the low amplitudes, and the signals for vesicle membranes that had some level of rhythmic signals is shown in **Fig. 3.30B**. Here, the initial two peaks for 0.75× are more visible and for 2.5× the latter two peaks can be seen. It is not clear exactly why these two concentrations show unclear indications of membrane oscillations, while the other concentration shows clear indications, without any clear trends with changing concentration. One possibility is because the signal amplitude is so low, it is possible that small focusing errors on the axial plane can obfuscate the signals. This could indicated explain why for 0.75× and 2.5× concentrations, only two peaks that can be observed at the expected locations and with near ~24-hour peak-to-peak distances between them. At the other points of focusing errors may cause larger changes in membrane intensity that obfuscate the small amplitude membrane oscillation signals. What is quite remarkable is that the 0.5× concentration, which failed to show any significant oscillation in the KaiB-6IAF channel, shows the clearest membrane oscillation. Perhaps oscillations in the membrane may persist even in low concentrations due to a concentration gradient on the membrane. This could suggest one reason why Kai proteins have the capability to associate to the membrane. Especially as membrane binding appears to be a negative component in ensuring clock oscillations in the vesicle model.

One concern for the observation of this data could be that it is due to bleed-through of the KaiB-6IAF into the rhodamine channel. Specifically, this scenario refers to KaiB-6IAF (488 nm) being excited by the rhodamine excitation laser (561 nm) and collected by the rhodamine channel. However, the clear membrane oscillation of the 0.5× concentration but notably lack of KaiB-6IAF oscillation in the vesicle lumen at that concentration, suggest that bleed-through is unlikely. Otherwise, it would be expected to see a larger amplitude membrane oscillation with increasing concentration, but this does not seem to be case. So, what is the origin then for the membrane oscillations? The hypothesis here is that the membrane oscillations are due to quenching of the rhodamine labeled lipids by tryptophan residues when KaiC binds to the membrane or when it binds with membrane bound KaiB. Tryptophan is known to also quench rhodamine along with other fluorophores (156), and in **Ch. 3.3.5.2** there are clear indications that KaiB binding behaviors changes when KaiC is present, preferring to form puncta instead of uniform distribution around the membrane. Along with other indications of membrane binding discussed earlier (**Ch. 3.3.5.2**), and that the cyanobacteria clock proteins can rhythmically bind to the membrane in vivo (111, 136), the data here strongly suggests that rhythmic membrane binding is occuring. This also suggests that the binding mechanism of the Kai clock proteins appears to be general and can bind to synthetic phospholipid bilayers on the vesicles. Further repeats will be necessary to confirm this behavior.

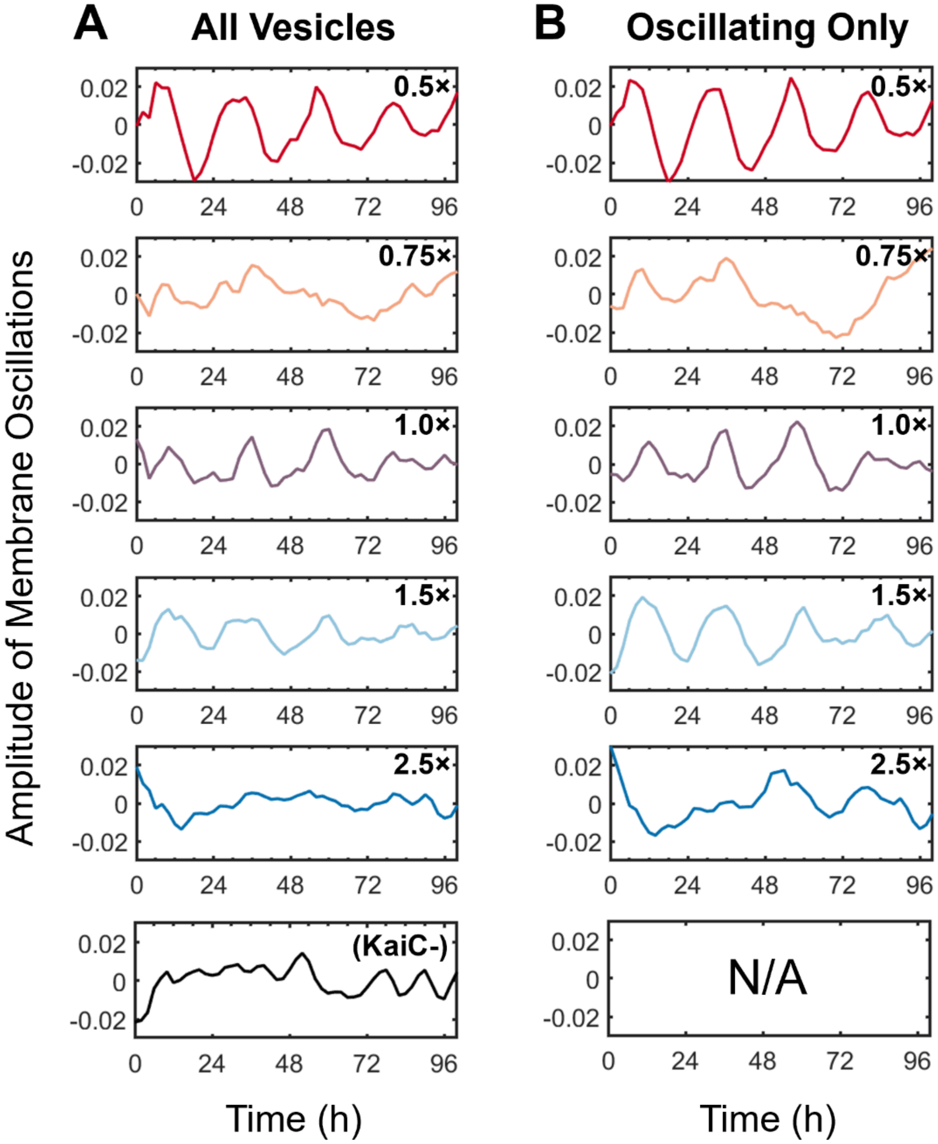

Fig. 3.30. Membrane oscillations may suggest rhythmic binding. (A) The average membrane signal of all vesicles from 0.5× to 2.5× protein concentrations are shown. The amplitude represents the change in intensity of the rhodamine-labeled lipids. **(B)** The average membrane signal of vesicles that was determined to contain oscillating signals by the FFT analysis. The only modification to FFT analysis is to remove the minimum peak height condition.

3.3.8 Resetting the clock vesicle rhythms in situ with low temperature induction

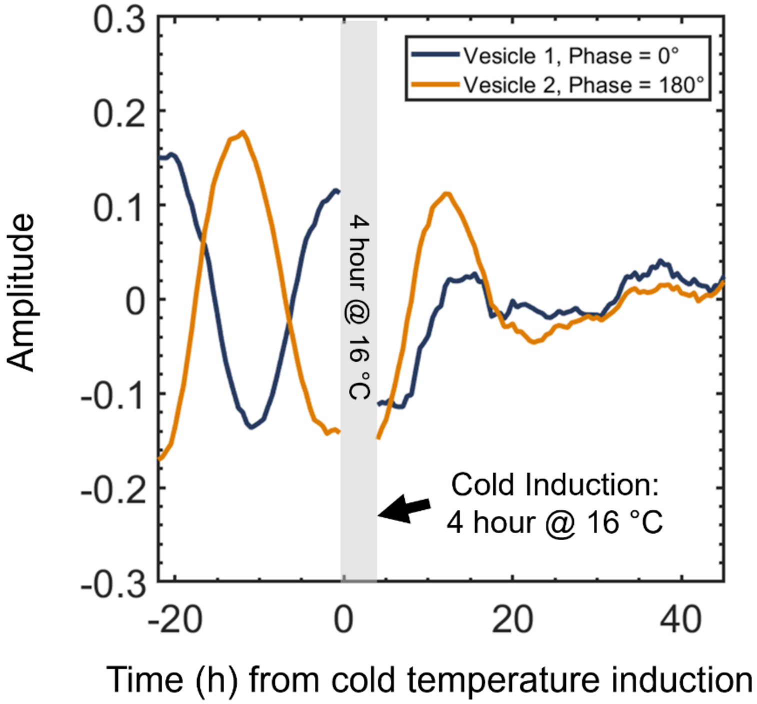

Fig. 3.31. Two out of phase vesicles are reset in situ with a cold temperature induction. Two clock signals in vesicles from two reactions started ~12 hours apart are initially approximately 180 degrees out of phase. Then a temperature of 16 °C is induced for four hours in situ. Then the same two vesicles are observed to have restarted their oscillations and have a similar phase. Temperature is set at 30 °C outside of the cold pulse.

One notable behavior of the cyanobacterial clock is when temperatures are decreased to 16 °C, KaiC can auto-phosphorylation without KaiA (132, 157, 158) and temperature pulses can be used to entrain the clock. In **Fig. 3.31**, two initially ~180° out of phase vesicles can be seen oscillating, before a pulse of cold temperature is induced for 4 hours at 16 °C in situ. One vesicle was reset at the peak of the oscillation (subjective day) and the other at the trough of the oscillation (subjective night). After the pulse of cold temperature, the clock reactions are now more closely synchronized, starting near the trough of the oscillation. There is still some degree of phase offset between the two signals, but this could be due to the length of the cold pulse not being long enough to fully reset the oscillations. The oscillation that was reset during the peak appears to show a more dampened signal compared to the signal rest during the trough. This shows similar results to reported desynchronization of the clock in cyanobacteria after low temperature pulses (158). However, the vesicle that was reset at the peak already had a lower amplitude prior to the reset due to it being half a cycle ahead. It is uncertain if the effect was due to the cold temperature induction or simply because it was at a later stage in the cycle.

3.3.9 Slow KaiBC disassociation without KaiA

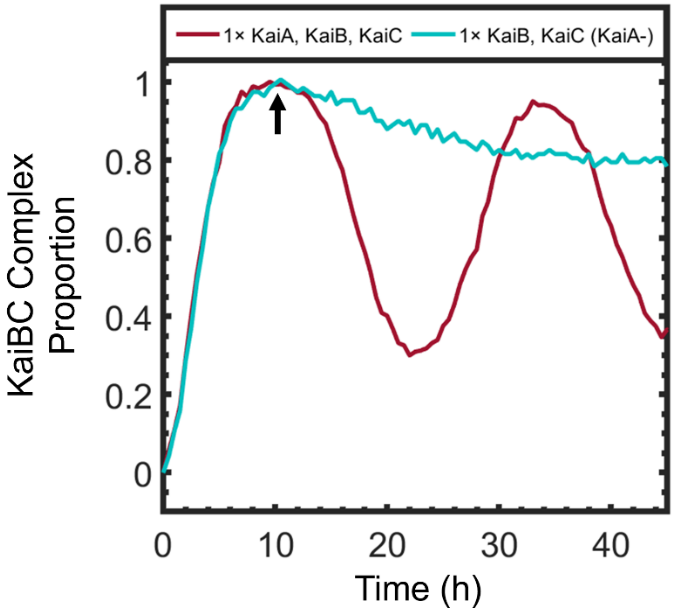

Fig. 3.32. KaiBC complex disassociation is very slow without KaiA. Bulk clock reactions in the plate reader show when KaiA is removed (teal line, KaiA-), KaiBC dissociation is very slow in comparison to when KaiA is present (dark red line). Black arrow shows when clock behavior diverges. KaiBC complex proportion refers to the number of maximum KaiBC complexes, or in other words the proportion of KaiB and KaiC that are located in a KaiBC complex.

During bulk in vitro experiments with the circadian clock oscillator, one notable finding was that the disassociation of KaiBC was significantly slower when KaiABC was not present. **Fig. 3.32** shows this behavior comparing the proportion of KaiBC complexes over time with one reaction with KaiA, KaiB, and KaiC at 1× concentrations (dark red line, KaiA+) and one reaction with KaiB and KaiC at 1× concentrations and omitting KaiA (teal line, KaiA-). As the number of KaiBC proportion comes to a maximum at the subjective night, the two reactions are identical, however after that point (denoted by black arrow) the disassociation of KaiBC diverges between the two reactions. The KaiA+ reaction disassociates over the course of the next 12 hours before beginning the association again, while the KaiA- reaction shows only ~10% of KaiBC complexes disassociates. This strongly suggests that KaiA may have a role in supporting the dissociation of KaiBC, or that KaiABC formation allows the complex to break apart when KaiC is fully dephosphorylated. At this time, literatures reports have not discussed this potential role of KaiA in the clock oscillation. Experiments studying KaiC phosphorylation may not be able to determine that this is occuring, as fluorescence intensity and anisotropy measurements, like done here, instead look at the changes in complex formation. The necessity of KaiA to facilitate the breakdown of KaiBC back into free KaiB and KaiC may be another way the clock can so excellently maintain its timing.

3.4 Conclusions

The study of the core oscillator of the cyanobacteria circadian clock in cell-mimetic giant vesicles demonstrates how cell-like variation and membrane binding can significantly hamper the fidelity of the clock. This was a finding that could not be fully appreciated using bulk experimental methods. In bulk experiments, concentration did not appear to have a significant role in affecting the clock behavior, and as long if the concentration was above 0.5× protein concentraitons and the stiochiometry is maintained the clock will oscillate (103, 111, 134). When intercellular variation in introduced in the vesicle minimal-cell model, this now is no longer the case, and the clock fidelity will now change significantly with both protein concentration and vesicle size. At 1× concentrations that are typically standard for bulk experiments (90, 103, 152), the clocks in vesicle only showed that ~30 % to 70% of the clock were functional depending on vesicle size. When considering the vesicles with diameters of 3 ± 0.5 μm, the closest to cellular volumes, the clock fidelity was only at 30%. When protein concentration increases to cellular concentrations, approximated by the 2.5× protein concentration, the clock fidelity jumps to ~70%, demonstrating how high expression levels in the cell is extremely important in counteracting the effects of intercellular variation, an unavoidable phenomenon in cells.

The clock fidelity was found to decrease with smaller vesicle sizes, and it was observed that the clock fidelity had had a linear relationship with the surface area to volume ratio (SA/V). This suggested that the size-based effects were due to membrane binding of the Kai protein, as larger SA/V ratios, which lead to lower clock fidelity, would sequester a larger proportion of proteins into the membrane, while larger sizes with smaller SA/V ratios, would see a less significant effect. This was exactly what was observed in the experimental results. Additionally, evidence of membrane binding of KaiB was found in confocal microscope images, showing a brighter ring of KaiB at the membrane when only KaiB was encapsulated. Interestingly, when the core oscillator, with KaiA, KaiB and KaiC, was encapsulated, instead of a ring of KaiB, formation of puncta can be seen localized on the membrane of the vesicles, and a ring of KaiB was no longer present. This suggests that the inclusion of KaiA or KaiC may localize with KaiB on the membrane and cause puncta to appear in place of the uniform ring of KaiB. In literature reports, puncta are also seen localized in the membrane of cyanobacteria cells and rhythmic localization was reported (136). In the vesicle, membrane oscillations were observed, that appear to suggest that KaiC may be rhythmically binding and unbinding in the vesicle membranes as well. This suggests that the membrane binding of the Kai proteins appear to be non-specific and can bind to the synthetic phospholipid bilayers on the vesicles shown here.

A model was also introduced to help validate the findings that intercellular variation and membrane binding was the primary cause of the experimental clock fidelity. The model, which used bulk data shown here and from literature reports, showed that the vesicle minimal cell model can be well characterized when the encapsulation statistics are well known, such as in this case where the encapsulation was well characterized in **Chapter 2**. Here, the model managed to produce clock fidelity data that matched remarkably well with the experimental data, following the trends of both concentration and vesicle size with a high degree of reproduction. Even when incorporating the co-encapsulation of proteins that initially formed complexes during loading, the model showed clock fidelity is even more closely follows experimental data. The clock fidelity shown by the experimental data and model suggested that with intercellular variation, the clock fidelity does not reach the near 100% fidelity expected in the native cyanobacteria, even when cellular concentrations were used. To explore a few potential mechanisms the clock may have access to in vivo, the model was extended to a few hypothetical scenarios. First it was shown that continued increases in concentration above cellular concentrations lead to diminishing returns and could not reach near 100% fidelity alone. If the variation was decreased low enough (CV ≤ 1), the fidelity could reach near 100% but simply lowering variation may not be possible due to the ubiquitous cellular variation present in cells. In the cyanobacteria, KaiB and KaiC share a common kaiBC promoter, and so there are expected to be some level of co-expression for these proteins. When this was evaluated using the clock fidelity model, it showed co-expression can increase clock fidelity, but it was not enough to push it close to 100% fidelity levels. But when competitive binding proteins, SasA and CikA, were introduced to the model, it showed this can allow clock fidelity to hit 98%, very close to what is expected in the cell. Transcriptional-translational feedback (TTFL) systems in the cyanobacteria (123, 124, 164, 165) likely play an important role in ensuring the clock fidelity reaches near 100% levels. This is constrast with views in literature which suggest the TTFL system is less important because the post translational core oscillator (PTO) is sufficient to keep in in vitro (112), which was found in vesicle models to not be completely true when considering intercellular variation.

The simulation of period and amplitude was also introduced to the model using bulk experimental data and data from literature, which managed to closely reproduce the expected period variation and amplitude. This has implications in that the behavior of the clock in vesicles appears to be deterministic and the behavior in the clock vesicle are well described by bulk experiments, providing the variations in concentration and protein stiochiometry can be described. This further shows that, at these concentrations and sizes, the effect of stochastic interactions is minimal. Instead, it is the variation and membrane binding that are responsible for the differences in the clock vesicles and bulk experiments. In vivo experiments had suggested that stochastic interactions were responsible for increasing variation in the periods of the core oscillator (135), however, findings here suggest that other mechanisms such as the inclusion of the SasA and CikA proteins, interactions of other cellular systems, or even what effect of a clock lost to noise may have on the expression of fluorescent reporter probes. The core oscillator could only produce oscillations with a limited variation of periods near ~24 hours or instead fail to oscillate, matching limitations seen from in vitro experiments.

In summary, while the core oscillator of clock can be perfectly fine on its own in a bulk in vitro enivronment, study of the clock in vesicles show how effects of intercellular variations and membrane binding can significantly impact the functionality of this cellular system and highlights the importance of other complementary systems that support it. The TTFL system of the clock has been referred to as less important because the core oscillator is found to be sufficient in bulk in vitro studies, but the results here show that the TTFL and other systems are extremely important for the clock to remain highly reliable. This study demonstrates the potential of using OSM-PAPYRUS as a biophysical platform to study the effects of intercellular variation, membrane interactions, and confinement into cellular volume of cellular systems. In contrast to in vivo studies, the vesicle platform allows nearly complete control of what cellular components are involved in the system without the need to worry about potential interactions of other cellular components or keeping the cell alive. Ultimately, it allows a simpler and more controlled approach for systems that can be used in a cell-free setting.

Future work that may build directly on this platform developed here, could branch into experiments with the full circadian clock system which also has potential in tying in gene expression systems that are controlled by the clock, bringing advancements to the development of a minimal synthetic cell. Other cellular systems could be of interest to study using OSM-PAPYRUS to induce intercellular variation in protein or other macromolecules that have relatively high concentration in the micromolar range.

3.5 Bibliography

34. T. Litschel, B. Ramm, R. Maas, M. Heymann, P. Schwille, Beating Vesicles: Encapsulated Protein Oscillations Cause Dynamic Membrane Deformations. *Angew. Chemie - Int. Ed.* **57**, 16286–16290 (2018).

90. J. Heisler, A. Chavan, Y.-G. Chang, A. LiWang, Real-Time In Vitro Fluorescence Anisotropy of the Cyanobacterial Circadian Clock. *Methods Protoc.* **2**, 42 (2019).

91. S. D. Chandradoss, *et al.*, Surface passivation for single-molecule protein studies. *J. Vis. Exp.*, 1–8 (2014).

92. J. Jonkman, C. M. Brown, G. D. Wright, K. I. Anderson, A. J. North, Tutorial: guidance for quantitative confocal microscopy. *Nat. Protoc.* **15**, 1585–1611 (2020).

93. A. Ferrand, K. D. Schleicher, N. Ehrenfeuchter, W. Heusermann, O. Biehlmaier, Using the NoiSee workflow to measure signal-to-noise ratios of confocal microscopes. *Sci. Rep.* **9**, 1–12 (2019).

94. C. L. Smith, Basic confocal microscopy. *Curr. Protoc. Neurosci.* (2011) https:/doi.org/10.1002/0471142301.ns0202s56.

95. J. B. Pawley, Handbook of biological confocal microscopy: Third edition. *Handb. Biol. Confocal Microsc. Third Ed.* **3rd**, 442–452 (2006).

96. D. Regan, J. Williams, P. Borri, W. Langbein, Lipid Bilayer Thickness Measured by Quantitative DIC Reveals Phase Transitions and Effects of Substrate Hydrophilicity. *Langmuir* **35**, 13805–13814 (2019).

97. J. Pan, S. Tristram-Nagle, N. Kučerka, J. F. Nagle, Temperature dependence of structure, bending rigidity, and bilayer interactions of dioleoylphosphatidylcholine bilayers. *Biophys. J.* **94**, 117–124 (2008).

98. J. Gallová, D. Uhríková, A. Islamov, A. Kuklin, P. Balgavý, Effect of cholesterol on the bilayer thickness in unilamellar extruded DLPC and DOPC liposomes: SANS contrast variation study. *Gen. Physiol. Biophys.* **23**, 113–128 (2004).

99. D. Huh, J. Paulsson, Random partitioning of molecules at cell division. *Proc. Natl. Acad. Sci. U. S. A.* **108**, 15004–15009 (2011).

100. M. Soltani, C. A. Vargas-Garcia, D. Antunes, A. Singh, Intercellular Variability in Protein Levels from Stochastic Expression and Noisy Cell Cycle Processes. *PLoS Comput. Biol.* **12**, 1–23 (2016).

101. A. Eldar, M. B. Elowitz, Functional roles for noise in genetic circuits. *Nature* **467**, 167–173 (2010).

102. A. Bar-Even, *et al.*, Noise in protein expression scales with natural protein abundance. *Nat. Genet.* **38**, 636–643 (2006).

103. H. Kageyama, *et al.*, Cyanobacterial Circadian Pacemaker: Kai Protein Complex Dynamics in the KaiC Phosphorylation Cycle In Vitro. *Mol. Cell* **23**, 161–171 (2006).

104. M. Ishiura, *et al.*, Expression of a gene cluster kaiABC as a circadian feedback process in cyanobacteria. *Science.* **281**, 1519–1523 (1998).

105. Y. Ouyang, C. R. Andersson, T. Kondo, S. S. Golden, C. H. Johnson, Resonating circadian clocks enhance fitness in cyanobacteria. *Proc. Natl. Acad. Sci. U. S. A.* **95**, 8660–8664 (1998).

106. D. Gonze, M. R. Roussel, A. Goldbeter, A model for the enhancement of fitness in cyanobacteria based on resonance of a circadian oscillator with the external light-dark cycle. *J. Theor. Biol.* **214**, 577–597 (2002).

107. C. P. Kyriacou, M. H. Hastings, Circadian clocks: genes, sleep, and cognition. *Trends Cogn. Sci.* **14**, 259–267 (2010).

108. E. S. Musiek, D. M. Holtzman, Mechanisms linking circadian clocks, sleep, and neurodegeneration. *Science.* **354**, 1004–1008 (2016).

109. P. Franken, D. J. Dijk, Circadian clock genes and sleep homeostasis. *Eur. J. Neurosci.* **29**, 1820–1829 (2009).

110. P. C. Zee, P. Manthena, The brain's master circadian clock: Implications and opportunities for therapy of sleep disorders. *Sleep Med. Rev.* **11**, 59–70 (2007).

111. Y. Kitayama, H. Iwasaki, T. Nishiwaki, T. Kondo, KaiB functions as an attenuator of KaiC phosphorylation in the cyanobacterial circadian clock system. *EMBO J.* **22**, 2127–2134 (2003).

112. R. K. Shultzaberger, J. S. Boyd, S. Diamond, R. J. Greenspan, S. S. Golden, Giving Time Purpose: The Synechococcus elongatus Clock in a Broader Network Context. *Annu. Rev. Genet.* **49**, 485–505 (2015).

113. C. H. Johnson, M. Egli, Metabolic compensation and circadian resilience in prokaryotic cyanobacteria. *Annu. Rev. Biochem.* **83**, 221–247 (2014).

114. S. E. Cohen, S. S. Golden, Circadian Rhythms in Cyanobacteria. *Microbiol. Mol. Biol. Rev.* **79**, 373–385 (2015).

115. T. Kondo, *et al.*, Circadian rhythms in prokaryotes: Luciferase as a reporter of circadian gene expression in cyanobacteria. *Proc. Natl. Acad. Sci. U. S. A.* **90**, 5672–5676 (1993).

116. T. Kondo, M. Ishiura, The circadian clock of cyanobacteria. *BioEssays* **22**, 10–15 (2000).

117. V. Dvornyk, O. Vinogradova, E. Nevo, Origin and evolution of circadian clock genes in prokaryotes. *Proc. Natl. Acad. Sci. U. S. A.* **100**, 2495–2500 (2003).

118. Y. Xu, T. Mori, C. H. Johnson, Cyanobacterial circadian clockwork: Roles of KaiA, KaiB and the KaiBC promoter in regulating KaiC. *EMBO J.* **22**, 2117–2126 (2003).

119. T. Wishiwaki, *et al.*, Role of KaiC phosphorylation in the circadian clock system of Synechococcus elongatus PCC 7942. *Proc. Natl. Acad. Sci. U. S. A.* **101**, 13927–13932 (2004).

120. H. Kageyama, T. Kondo, H. Iwasaki, Circadian formation of clock protein complexes

by KaiA, KaiB, KaiC, and SasA in cyanobacteria. *J. Biol. Chem.* **278**, 2388–2395 (2003).

121. H. Iwasaki, *et al.*, A KaiC-interacting sensory histidine kinase, SasA, necessary to sustain robust circadian oscillation in cyanobacteria. *Cell* **101**, 223–233 (2000).

122. O. Schmitz, M. Katayama, S. B. Williams, T. Kondo, S. S. Golden, CikA, a bacteriophytochrome that resets the cyanobacterial circadian clock. *Science.* **289**, 765–768 (2000).

123. D. Zwicker, D. K. Lubensky, P. R. Ten Wolde, Robust circadian clocks from coupled protein-modification and transcription-translation cycles. *Proc. Natl. Acad. Sci. U. S. A.* **107**, 22540–22545 (2010).

124. S. W. Teng, S. Mukherji, J. R. Moffitt, S. De Buyl, E. K. O'Shea, Robust circadian oscillations in growing cyanobacteria require transcriptional feedback. *Science.* **340**, 737–740 (2013).

125. K. Oyama, C. Azai, K. Nakamura, S. Tanaka, K. Terauchi, Conversion between two conformational states of KaiC is induced by ATP hydrolysis as a trigger for cyanobacterial circadian oscillation. *Sci. Rep.* **6**, 1–11 (2016).

126. A. Mukaiyama, *et al.*, Conformational rearrangements of the C1 ring in KaiC measure the timing of assembly with KaiB. *Sci. Rep.* **8**, 1–10 (2018).

127. Y.-I. Kim, G. Dong, C. W. Carruthers, S. S. Golden, A. LiWang, The day/night switch in KaiC, a central oscillator component of the circadian clock of cyanobacteria. *Proc. Natl. Acad. Sci.* **105**, 12825–12830 (2008).

128. R. Pattanayek, *et al.*, Analysis of KaiA-KaiC protein interactions in the cyano-bacterial circadian clock using hybrid structural methods. *EMBO J.* **25**, 2017–2028 (2006).

129. R. Tseng, *et al.*, Cooperative KaiA-KaiB-KaiC interactions affect KaiB/SasA competition in the circadian clock of cyanobacteria. *J. Mol. Biol.* **426**, 389–402 (2014).

130. C. Brettschneider, *et al.*, A sequestration feedback determines dynamics and temperature entrainment of the KaiABC circadian clock. *Mol. Syst. Biol.* **6**, 389 (2010).

131. X. Qin, *et al.*, Intermolecular associations determine the dynamics of the circadian KaiABC oscillator. *Proc. Natl. Acad. Sci.* **107**, 14805–14810 (2010).

132. T. Mori, *et al.*, Elucidating the ticking of an in vitro circadian clockwork. *PLoS Biol.* **5**, 841–853 (2007).

133. T. Nishiwaki, *et al.*, A sequential program of dual phosphorylation of KaiC as a basis for circadian rhythm in cyanobacteria. *EMBO J.* **26**, 4029–4037 (2007).

134. A. G. Chavan, *et al.*, Reconstitution of an intact clock reveals mechanisms of circadian timekeeping. *Science* **374**, 170 (2021).

135. J. Chew, E. Leypunskiy, J. Lin, A. Murugan, M. J. Rust, High protein copy number is required to suppress stochasticity in the cyanobacterial circadian clock. *Nat. Commun.* **9**, 1–10 (2018).

136. S. E. Cohen, *et al.*, Dynamic localization of the cyanobacterial circadian clock proteins. *Curr. Biol.* **24**, 1836–1844 (2014).

137. T. Mori, *et al.*, Revealing circadian mechanisms of integration and resilience by visualizing clock proteins working in real time. *Nat. Commun.* **9** (2018).

138. J. A. Swan, *et al.*, Coupling of distant ATPase domains in the circadian clock protein KaiC. *Nat. Struct. Mol. Biol.* **29**, 759–766 (2022).

139. H. Ito, *et al.*, Autonomous synchronization of the circadian KaiC phosphorylation rhythm. *Nat. Struct. Mol. Biol.* **14**, 1084–1088 (2007).

140. N. Maheshri, E. K. O'Shea, Living with noisy genes: How cells function reliably with inherent variability in gene expression. *Annu. Rev. Biophys. Biomol. Struct.* **36**, 413–434 (2007).

141. X. yu Zheng, E. K. O'Shea, Cyanobacteria Maintain Constant Protein Concentration despite Genome Copy-Number Variation. *Cell Rep.* **19**, 497–504 (2017).

142. J. Sheng, R. Vannela, B. E. Rittmann, Evaluation of methods to extract and quantify lipids from Synechocystis PCC 6803. *Bioresour. Technol.* **102**, 1697–1703 (2011).

143. P. Moreau, *et al.*, Lipid trafficking in plant cells. *Prog. Lipid Res.* **37**, 371–391 (1998).

144. J. Joyard, *et al.*, The biochemical machinery of plastid envelope membranes. *Plant Physiol.* **118**, 715–723 (1998).

145. S. Rexroth, *et al.*, The plasma membrane of the cyanobacterium gloeobacter violaceus contains segregated bioenergetic domains. *Plant Cell* **23**, 2379–2390 (2011).

146. W. Hewelt-Belka, Á. Kot-Wasik, P. Tamagnini, P. Oliveira, Untargeted lipidomics analysis of the cyanobacterium synechocystis sp. Pcc 6803: Lipid composition variation in response to alternative cultivation setups and to gene deletion. *Int. J. Mol. Sci.* **21**, 1–21 (2020).

147. Z. Gombos, H. Wada, Z. Varkonyi, D. A. Los, N. Murata, Characterization of the Fad 12 mutant of Synechocystis that is defective in Δ12 acyl-lipid desaturase activity. *Biochim. Biophys. Acta - Lipids Lipid Metab.* **1299**, 117–123 (1996).

148. K. S. Ramamurthi, S. Lecuyer, H. A. Stone, R. Losick, Geometric cue for protein localization in a bacterium. *Science.* **323**, 1354–1357 (2009).

149. D. Garenne, V. Noireaux, Analysis of Cytoplasmic and Membrane Molecular Crowding in Genetically Programmed Synthetic Cells. *Biomacromolecules* **21**, 2808–2817 (2020).

150. M. Sarcina, M. J. Tobin, C. W. Mullineaux, Diffusion of phycobilisomes on the thylakoid membranes of the cyanobacterium Synechococcus 7942: Effects of phycobilisome size, temperature, and membrane lipid composition. *J. Biol. Chem.* **276**, 46830–46834 (2001).

151. J. Snijder, *et al.*, Structures of the cyanobacterial circadian oscillator frozen in a fully assembled state. *Science.* **355**, 1181–1184 (2017).

152. M. Nakajima, H. Ito, T. Kondo, In vitro regulation of circadian phosphorylation rhythm of cyanobacterial clock protein KaiC by KaiA and KaiB. *FEBS Lett.* **584**, 898–902 (2010).

153. F. Moronta-Barrios, J. Espinosa, A. Contreras, Negative control of cell size in the cyanobacterium Synechococcus elongatus PCC 7942 by the essential response regulator RpaB. *FEBS Lett.* **587**, 504–509 (2013).

154. J. S. Van Zon, D. K. Lubensky, P. R. H. Altena, P. Rein, An allosteric model of circadian KaiC phosphorylation. *Proc. Natl. Acad. Sci.* **104**, 7420–7425 (2007).

155. Y. G. Chang, *et al.*, A protein fold switch joins the circadian oscillator to clock output in cyanobacteria. *Science.* **349**, 324–328 (2015).

156. N. Marmé, J. P. Knemeyer, M. Sauer, J. Wolfrum, Inter- and Intramolecular Fluorescence Quenching of Organic Dyes by Tryptophan. *Bioconjug. Chem.* **14**, 1133–1139 (2003).

157. Y. Murayama, *et al.*, Low temperature nullifies the circadian clock in cyanobacteria through Hopf bifurcation. *Proc. Natl. Acad. Sci. U. S. A.* **114**, 5641–5646 (2017).

158. S. Gan, E. K. O'Shea, An Unstable Singularity Underlies Stochastic Phasing of the Circadian Clock in Individual Cyanobacterial Cells. *Mol. Cell* **67**, 659-672.e12 (2017).

159. M. Liberton, J. R. Austin, R. Howard Berg, H. B. Pakrasi, Insights into the complex 3-D architecture of thylakoid membranes in the unicellular cyanobacterium Cyanothece sp. ATCC 51142. *Plant Signal. Behav.* **6**, 566–569 (2011).

160. I. Mihalcescu, W. Hsing, S. Leibler, Resilient circadian oscillator revealed in individual cyanobacteria. *Nature* **430**, 81–85 (2004).

161. M. Amdaoud, M. Vallade, C. Weiss-Schaber, I. Mihalcescu, Cyanobacterial clock, a stable phase oscillator with negligible intercellular coupling. *Proc. Natl. Acad. Sci. U. S. A.* **104**, 7051–7056 (2007).

162. M. Nakajima, *et al.*, Reconstitution of Circadian Oscillation of Cyanobacterial KaiC Phosphorylation in Vitro. *Science.* **308**, 414–416 (2005).

163. M. Kaur, A. Ng, P. Kim, C. Diekman, Y. I. Kim, CikA Modulates the Effect of KaiA on the Period of the Circadian Oscillation in KaiC Phosphorylation. *J. Biol. Rhythms*, 218–223 (2019).

164. J. Tomita, M. Nakajima, T. Kondo, H. Iwasaki, No transcription-translation feedback in circadian rhythm of KaiC phosphorylation. *Science.* **307**, 251–254 (2005).

165. C. H. Johnson, P. L. Stewart, M. Egli, The Cyanobacterial Circadian System: From Biophysics to Bioevolution. *Annu. Rev. Biophys.* **40**, 143–167 (2011).

Appendix

A.1 Table of One-Way Analysis of Variance Testing Statistics

Group 1	Group 2	dF	F	α	p	Significance	Comments
Fraction of Empty Vesicles	[FITC-BSA] Loading Concentration	3, 8	0.46	0.05	0.72	NS ($p > \alpha$)	Fraction of empty vesicles is not significantly affected by FITC-BSA loading concentration
Coefficient of Variation	[FITC-BSA] Loading Concentration	3, 8	1.24	0.05	0.36	NS ($p > \alpha$)	The coefficient of variation (CV) is not significantly affected by FITC-BSA loading concentration

A.2 Table of Kruskal Wallis One Way Analysis of Variance Testing Statistics

Group 1	Group 2	dF	X^2	α	p	Significance	Comments
Vesicle Diameter	Encapsulated [FITC-BSA]	6, 617	2.01	0.05	0.92	NS ($p > \alpha$)	Encapsulated concentrations are not significantly affected by vesicle diameter.

A.3 Code for GUV Segmentation – Relative Encapsulation

```
%% Segmentation for Relative Encapsulation
% with background correction option
close all
clear all

%% Parameters
BGcorr = 1; % 1(on) or 0(off) for background correction by surface fit

%% Directory
files1 = dir('*.czi');
a=pwd;
mkdir('Segmented_mat')
mkdir('Background Correction')
threshotsu=[];
ntiles = length(files1);

for k=1:ntiles %ntiles
    filename = files1(k).name;
    data= bfopen(filename);                                     %loads
file
    omeMeta1 = data{1,4};                                       %loads
metadata
    Xscale = double(omeMeta1.getPixelsPhysicalSizeX(0).value()); %scale
in x-dim 10x0.3=0.397 63X1.4=0.0852;
    Xdim=omeMeta1.getPixelsSizeX(0).getValue();                 %image
size X, in pixels
    Ydim=omeMeta1.getPixelsSizeY(0).getValue();                 %image
size Y, in pixels
    %% Split red and green channels
    red_data = data{1,1}(1:2:length(data{1,1}(:,1)),1);
    green_data = data{1,1}(2:2:length(data{1,1}(:,1)),1);
%     red_mat = cat(3,red_data{:});
%     green_mat = cat(3,green_data{:});

    %% Segmentation
    for s=1:length(red_data)
        zmean = red_data{s};
        I2 = zmean;  %medfilt2(zmean,[2 2]);%Filter image to reduce
noise (off by default)
        I2 = imsharpen(I2,'Radius',5,'Amount',3);

%         I2 = imclearborder(I2); %This occurs later
        I2 = imfill(I2,'holes');
%         I2 = imadjust(I2,[0 0.4],[]);
        thresh = multithresh(I2,4); %*0.3; %Adjust thresholding
        threshotsu{k} = double(thresh(1))/255;
        I3 = imbinarize(I2,(threshotsu{k}));%Threshold
        %I4 = imerode(I3,strel('disk',3));  %Erode to remove
unconnected noise pixels and nanotubes
        %I4 = imdilate(I4,strel('disk',3)); %dilate to restore boundary
pixels that have been eroded
        I5 = -bwdist(~I3);
        I5(~I5) = -Inf;
```

```
        I6 = imhmin(I5,1); %Set the 2nd value to tune the watershed
segmentation sensitivity.
        L0 = watershed(I6);
        %FITC = imgaussfilt(FITC,[2 2]);

        %% Region properties

        bgshape = regionprops('table',L0,zmean,'Area');
        bgobj = find(bgshape.Area == max(bgshape.Area)); %Object with
largest area is the background

        LBG = uint16(L0 == bgobj); %Set background
        L0a = imclearborder(L0); %Remove background connected objects
        L0b = L0a~=0; %create binary image
        L1 = bwlabel(L0b); %relabel binary image to prevent NaNs

        shapes =
regionprops('table',L1,zmean,'Area','EulerNumber','FilledArea',...
            'Eccentricity','EquivDiameter','Centroid','BoundingBox',...
            'MeanIntensity','PixelValues', 'PixelList', 'Image',
'Perimeter','PixelIdxList');

        bgshape1 =
regionprops('table',LBG,green_data{s},'MeanIntensity',...
            'PixelValues','PixelIdxList');

        %% BG Correction
        % Only runs if BGcorr is set to 1
        if BGcorr == 1
            BG = zeros(size(L1));
            E2 = cell2mat(bgshape1.PixelIdxList);
            BG(E2)=cell2mat(bgshape1.PixelValues);
            BG(BG==0) = NaN;
    %         BGfilt = imgaussfilt(BG,20);
            [xData, yData, zData] =
prepareSurfaceData(1:Xdim,1:Ydim,BG);
            ft = fittype( 'poly22' );
            [fitresult, gof] = fit( [xData, yData], zData, ft,
'Normalize', 'off' );
            cf=coeffvalues(fitresult);
            x1=1:Xdim;
            y1=1:Ydim;
            [x1,y1]=meshgrid(x1,y1);
            %z2{k,1}=d+a.*x1+b.*y1;
            z2 = cf(1) + cf(2)*x1 + cf(3)*y1 + cf(4)*x1.^2 +
cf(5)*x1.*y1 + cf(6)*y1.^2;
            o1 = max(z2,[],'all'); %Maximum height on fitted
            z3=o1./z2; %determine correction factor.
    %         z4=double(z.*z3);
            green_corr = double(green_data{s}).*z3; %correcting the
original data;

            BG_gauss = imgaussfilt(green_data{s},5);

            h = figure; set(h,'Visible','off')
```

```
            subplot(2,2,1); h = surf(z2); set(h,'LineStyle','none');
            title('Surface Fit'); colorbar;
            subplot(2,2,2); h = surf(z3); set(h,'LineStyle','none');
            title('Correction Factor'); colorbar;
            subplot(2,2,3); h = surf(BG_gauss);
            set(h,'LineStyle','none');
            title('Original Intensity');
            zlim([min(BG_gauss,[],'all')*0.9
            max(BG_gauss,[],'all')*1.1]); colorbar;
            subplot(2,2,4); h = surf(imgaussfilt(green_corr,5));
            set(h,'LineStyle','none');
            title('Corrected Intensity');
            zlim([min(BG_gauss,[],'all')*0.9
            max(BG_gauss,[],'all')*1.1]); colorbar;


saveas(h,strcat('BG_Correction_',num2str(k),'_Z',num2str(s),'.png'))

movefile(strcat('BG_Correction_',num2str(k),'_Z',num2str(s),'.png'),str
cat(pwd,'/Background Correction'))
            close
        else
            green_corr = green_data{s};
        end
        %% BG Corrected Seg
        gshapes =
regionprops('table',L1,green_corr,'Area','EulerNumber','FilledArea',...
        'Eccentricity','EquivDiameter','Centroid','BoundingBox',...
        'MeanIntensity','PixelValues', 'PixelList', 'Image',
        'Perimeter','PixelIdxList');

        bgshapes2 =
regionprops('table',LBG,green_corr,'MeanIntensity','PixelIdxList','Pixe
lValues');

        bgint = bgshapes2.MeanIntensity;

        %% Measure core of the vesicles
        J1 = zeros(size(L1));
        A = gshapes.PixelList;
        B = num2cell(gshapes.Centroid,2);
        C = cellfun(@minus,A,B,'UniformOutput',false);
        C1 = ones(size(C))*2;
        C2 = cellfun(@power,C,num2cell(C1),'UniformOutput',false);
        C3 = cellfun(@transpose,C2,'UniformOutput',false);
        C3 = cellfun(@sum,C3,'UniformOutput',false);
        C3 = cellfun(@transpose,C3,'UniformOutput',false);
        D = gshapes.EquivDiameter * (1/3);
        D1 = cellfun(@le,C3,num2cell(D),'UniformOutput',false);
        D2 = gshapes.PixelValues;
        D3 = cellfun(@(D2,D1)D2(D1==1),D2,D1,'UniformOutput',false);
        %Only keep pixel values close to centroid
        D4 = cellfun(@(x)sum(x)/length(x),D3);
        gshapes.PixelValuesCore = D3;
        gshapes.MeanIntensityCore = D4;
```

```
        %% Save Files
        outputFileNameMAT1 = strcat(filename(1:end-
            4),'_Z',num2str(s),'.mat');

      save(outputFileNameMAT1,'shapes','gshapes','bgint','bgshapes2'...
            ,'zmean','Xscale','L1','LBG'); %,'cc2'
        movefile(outputFileNameMAT1,strcat(a,'\Segmented_mat'));

    end
end %end of iteration through k files
```

A.4 Code for GUV Selection – Relative Encapsulation

```
%Last edited 11.9.21 Select based on all vesicles
%63X Objective: Relative Encapsulation (Thin slices)
%Input:     .mat files with regionprops information for vesicles in
individual tile scans
%Process:   Identifies unilamellar vesicles and labels tif files
%Output:    .mat files with regionprops information on vesicles
classifed as unilamellar

close all, clear all
mat_dir = 'Selected_mat_all';
hist_dir = 'Selected_histogram_all';
mkdir(mat_dir),
mkdir(hist_dir)
a=pwd;
cd Segmented_mat
files2 = dir('*.mat'); %-6 um offset: 10+ um vesicles
% files2{2} = dir('*Z2.mat'); %-4 um offset: 6-10 um vesicles
% files2{3} = dir('*Z3.mat'); %-2 um offset: 2-6 um vesicles

edges = 0:0.02:10;
centers = (edges(1:end-1)+edges(2:end))/2;


%% Initialize/Reinitalize shape variables for this set
samples = {};
L1_all = {};
i_all = [];
i_cv_all = {};
shapesall = {};
gshapesall = {};
zmaxall = {};
bgint_all = [];


%% Collects all data for current Z position
for j=1:length(files2)
    i_cv = []; %i_cv needs to be reinitalized for each iteration
    samples{j} = files2(j).name(1:end-4);
    data = open(files2(j).name);
%     L1 = zeros(size(data.L));
    L1_all{j}=data.L1;
    i_px = transpose(data.shapes.PixelValues);
    for k = 1:length(i_px)
        i_cv(k) = std(double(i_px{k}))/mean(double(i_px{k}));
    end
    Xscale = data.Xscale;
    shapesall{j}=data.shapes;
    gshapesall{j} = data.gshapes;
    zmaxall{j}=data.zmean;
    bgint_all(j) = data.bgint;
    i_all = [i_all,i_cv];
    i_cv_all{j} = i_cv;
end
```

```
%% Peak fitting

cd(a)
ydata = histcounts(i_all,edges,'Normalization','probability');
[pks,locs, w, p] =
findpeaks(ydata,centers,'MinPeakDistance',0.9,'MinPeakHeight',0.1*max(y
data));
if ~ isempty(locs)
%     lb = locs(1)+(3*w(1)); %Original %locs-(w);
    lb = 0.73; %0.75; %Selected lower bound (check montages to adjust)

%     lb = centers(find(centers<locs(1) & ydata<0.1*pks(1),1,'last'));
    %     if isempty(lb)
%         lb = centers(1);
%     end
%     ub = locs+(3*w); %0.6; %Adjusting this will make it more or less
selective

   %Plot histogram
    h=figure; hold on; axis square; set(h, 'Visible', 'on');
    h=histogram(i_all,edges,'Normalization','probability',
'FaceColor','w');

findpeaks(ydata,centers,'MinPeakDistance',0.9,'MinPeakHeight',0.1*max(y
data),'Annotate', 'Extents');
    plot([lb lb],[0 1],'b'); % plot([ub ub],[0 1],'b');
    legend(strjoin({'peak loc =',num2str(locs)}), strjoin({'width
=',num2str(round(w*100)/100)}),...
         strjoin({'lower bound',num2str(round(lb*100)/100)}));
%,strjoin({'upper bound',num2str(round(ub*100)/100)})
    legend('Location','NorthEast');
    axis([0 max(i_all) 0 0.5]),title('All
images'),xlabel('Intensity'),ylabel('Frequency');
    saveas(gcf,fullfile(a,hist_dir,strcat('hist_Z','.png')));
%     movefile(strcat('hist_Z','.png'),strcat(a,hist_dir));
end

if isempty(locs)
    h=figure; hold on; axis square; set(h, 'Visible', 'on');
    h=histogram(i_all,edges,'Normalization','probability',
'FaceColor','w');
    legend('Location','NorthEast');
    axis([0 0.5 0
0.2]),title('No_Peak'),xlabel('Intensity'),ylabel('Frequency');
    saveas(gcf,fullfile(a,hist_dir,strcat('hist_','No_Peak','.png')));
%     movefile(strcat('hist_','No_Peak','.png'),strcat(a,hist_dir));
end

%% Choose only vesicles
for k=1:length(files2)
    if ~ isempty(locs)
        %choose only vesicles
        ves_sel = i_cv_all{k} >= lb; %(i_cv_all{k} <= ub) & i_cv_all{k}
>= lb);
```

```
        diameter_UV = shapesall{k}.EquivDiameter(ves_sel);
        MeanIntensity_UV = shapesall{k}.MeanIntensity(ves_sel);
        EncapInt_UV = gshapesall{k}.MeanIntensity(ves_sel); %added
        EncapCore_UV = gshapesall{k}.MeanIntensityCore(ves_sel);
        V = cell2mat(shapesall{k}.PixelIdxList(ves_sel));

        redpixels_UV = shapesall{k}.PixelValues(ves_sel); %3/17 Al
        greenpixels_UV = gshapesall{k}.PixelValues(ves_sel); %3/17 AL

        %identify non-vesicles
        NV = cell2mat(shapesall{k}.PixelIdxList(i_cv_all{k} < lb));
%         NB = cell2mat(shapesall{k}.PixelIdxList(i_cv_all{k} < lb));
        %relabel label matrix
        L1_all{k}(NV)=8;
        L1_all{k}(V)=3;
%         L1_all{k}(NB)=7;

        %Identify Background Intensity
        bgint = bgint_all(k);
    end
    shapes = shapesall{k};
    gshapes = gshapesall{k};
    zmax = zmaxall{k};
    L1 = L1_all{k};
    cv = i_cv_all{k};


save(fullfile(a,mat_dir,strcat(samples{k},'_selected.mat')),'zmax','L1'
,'shapes','Xscale','diameter_UV','MeanIntensity_UV','EncapInt_UV'...

,'EncapCore_UV','redpixels_UV','greenpixels_UV','bgint','ves_sel','cv')
;
%     movefile(strcat(samples{k},'_selected.mat'),strcat(a,mat_dir));
end

% cd ../
```

A.5 Code for clock vesicle processing (FFT + Detrending)

```
%% Clock_Ves_Process
% Combined clock vesicle processing code whole data sets

% Note: Data structure must be inputted with a field called 'raw', and
% inside, raw data from vesicle sizes labeled as d4 for 4 um diameter
...
% vesicles, d6 for 6 um vesicles etc.

%% Select Input Data Structure Name
clock2_5 = clock2_5; %Input data, press shift enter after changing
(setup this way for easy changing). Both values should be equal.

%% Options for detrend and normalization
dtype = 'rawbg';  % Select data type: 'raw' or 'rawbg'. 'rawbg' is
background subtracted intensities.
emp = 0;          % Default = 20. Percentage of empty vesicles (static)
eval_len = 51;    % Default = 51. Set the length of data to evaluate.
det_type = 2;     % 1 = linear detrending, 2 = exponential detrending
det_term = 2;     % Terms for exponential detrending or linear detrending
(n-th deg polynomial)

%% Options for FFT
eval_len_fft = 50;           % Use
minfreq      = 16;           % Minimum period to be considered possible
oscillation
maxfreq      = 30;           % Maximum period to be considered possible
oscillation
minpeakh     = 0.04;         % 0.03 Encap Standard; % 0.04 Encap BG;
%0.011 %Old; %0.03/4 (Red Chan?)
plotlag      = 0;            % length(encap_data(:,1)); %0; %How many
FFT spectras to plot.
plotfig      = 0;            % Plot scatterplot figure: 1=Yes, 0=No
snr_val      = 1.3;          %1.3 = default for bg sub %1.2 = default
(no bg sub)


%% Runs processing for all sizes in dataset
fn = {'d2'};%fieldnames(clock2_5.(dtype));
out = strcat(dtype(4:end),'dnorm'); %sets output name as dnorm or
bdnorm based on given data type (dtype)
fft_out = strcat('fft',dtype(4:end)); %sets output FFT name as fft or
fftbg based on given data type (dtype)

%initalize variables
clock2_5.(fft_out).all.amp =        [];
clock2_5.(fft_out).all.period =     [];
clock2_5.(fft_out).all.osc_frac =   [];
clock2_5.(fft_out).all.osc =        [];
clock2_5.(fft_out).all.ampmean =    [];
clock2_5.(fft_out).all.periodmean = [];
clock2_5.(fft_out).all.amp_sd =     [];
clock2_5.(fft_out).all.period_sd =  [];
clock2_5.(out).all =                [];
```

```
for i = 1:numel(fn)
    %% Remove empty vesicles by specified amount
    wdata = clock2_5.(dtype).(fn{i}); %working dataset
    wdata = wdata(:,1:eval_len);

    rem_emp = prctile(mean(wdata,2),emp);
    wdata(mean(wdata,2)<rem_emp,:) = [];

    %Remove any negative values (may occur for bg sub data)
    neg_filt = wdata <= 0;
    neg_filt = any(neg_filt,2); %
    wdata(neg_filt,:) = [];

    %% Detrend and normalize data
    wdata_norm = []; %clear any previous list
    for j = 1:length(wdata(:,1))
        if det_type == 1
            wdata_norm(j,:) =
detrend(wdata(j,:)/mean(wdata(j,:)),det_term);
        end
        if det_type == 2
            wdata_norm(j,:) =
expdet2(wdata(j,:)/mean(wdata(j,:)),det_term);
        end
    end

    clock2_5.(out).(fn{i}) = wdata_norm;

    %% FFT Analysis
    encap_data = wdata_norm(:,1:eval_len_fft); %This is the deterended
data

    peak_diff   = [];
    peak_max    = [];
    noise       = [];
    fft_max     = [];
    fft_peaks   = {};
    fft_locs    = {};
    signal_count = 0;

    imfreq = 2; %2 (default) %How many hours per timepoint
    tx = 0:imfreq:(eval_len_fft-1)*imfreq; %Time axis

    for k = 1:length(encap_data(:,1)) %Loop over each vesicle signal
        %% FFT settings
        zpad = 1000;                    % Amount of zero padding
        Fs = 1/imfreq;          %0.5;   % Sampling frequency
        T = 1/Fs;                       % Sampling period
        L = length(encap_data(k,:));    % Length of signal
        L2 = L+zpad;                    % Length of signal + zeropad
        t = (0:L-1)*T;                  % Time vector
        %% FFT analysis routine
        % Compute Fourier transform of the signal
```

```
        Y = fft([encap_data(k,:),zeros(1,zpad)]);
        % Comupte Two sided spectrum
        P2 = abs(Y/L);
        P1 = P2(1:L2/2+1);
        P1(2:end-1) = 2*P1(2:end-1);
        % Define frequency domain
        f = Fs*(0:(L2/2))/L2;
    %     f2 = Fs*(0:(L2/2))/L2;
        f_t = 1./f;                      %Convert frequency domain into
time domain (in hours)

        %% Find max peak height if there was no min height (For
troubleshooting only)
        [pks0,per0] = findpeaks(flip(P1(2:end)),flip(f_t(2:end)));
        fft_peaks{k} = pks0(per0<=maxfreq & per0>=minfreq);
        fft_locs{k} = per0(per0<=maxfreq & per0>=minfreq);
        if ~isempty(pks0(per0<=maxfreq & per0>=minfreq))
            fft_max(k) = max(pks0(per0<=maxfreq & per0>=minfreq));
        else
            fft_max(k) = NaN;
        end


        %% Find max peak from Fourier transform of signal within
minpeakh and freq ranges
        [pks,per] =
findpeaks(flip(P1(2:end)),flip(f_t(2:end)),'MinPeakHeight',minpeakh);
            % Flip required so X is increasing (b/c time domain is
used).
            % 2:end, is used so the zero frequency is not included (1/0
= inf = error).
        pks1 = pks(per<=maxfreq & per>=minfreq);
        per1 = per(per<=maxfreq & per>=minfreq);
        pk_max = max(pks1);
        per_max = per1(pks1 == max(pks1));

         %% Noise check: Check for peaks in low frequency regime that
correspond to high noise signal
        if ~isempty(pk_max)
            signal_count = signal_count + 1;
            pks_noise = pks0(per0<=maxfreq & per0<per_max);
            per_noise = per0(per0<=maxfreq & per0<per_max);
        else
            pks_noise = [];
            per_noise = [];
        end

        if ~isempty(per_noise) && any(pks_noise * snr_val > pk_max)
            noise(k) = 1;
        else
            noise(k) = 0;
        end


        %% Record frequency of peak and peak height
```

```
        if ~isempty(per_max) && noise(k) == 0
            peak_diff(k) = per_max;
            peak_max(k) = pk_max;
        else
            peak_diff(k) = NaN;
            peak_max(k) = NaN;
        end
    end

    %% Compile FFT peaks/locs list into single cell
    fft_peaks_com{1} = transpose(fft_peaks);
    fft_per_com{1} = transpose(fft_locs);

    %% How many oscillating
    osc = peak_diff >= 0;
    osc_frac = sum(osc)/length(osc);

    fft_dat =
struct('period',peak_diff,'amp',peak_max,'osc',osc,'osc_frac',osc_frac.
..

,'noise',noise,'fftmax',fft_max,'fftpeaks',fft_peaks_com,'fftperiod',ff
t_per_com,'minpeak',minpeakh...
    ,'signal_count',signal_count ...

,'noise2signal',sum(noise)/sum(signal_count),'SNR_req',snr_val,'Empty_p
',emp/100 ...
    ,'Freq',1./f,'Amp',P1); %,'sub_list',temp_encapsublist

    %Output data for size
    clock2_5.(fft_out).(fn{i}) = fft_dat;

    %% Output aggregate data for all sizes
    clock2_5.(fft_out).all.amp =
vertcat(clock2_5.(fft_out).all.amp,rmmissing(transpose(clock2_5.(fft_ou
t).(fn{i}).amp)));
    clock2_5.(fft_out).all.period =
vertcat(clock2_5.(fft_out).all.period,rmmissing(transpose(clock2_5.(fft
_out).(fn{i}).period)));
    clock2_5.(fft_out).all.osc_frac =
vertcat(clock2_5.(fft_out).all.osc_frac,rmmissing(transpose(clock2_5.(f
ft_out).(fn{i}).osc_frac)));
    clock2_5.(fft_out).all.osc =
vertcat(clock2_5.(fft_out).all.osc,rmmissing(transpose(clock2_5.(fft_ou
t).(fn{i}).osc)));

    %Mean/SD data for each size
    clock2_5.(fft_out).all.ampmean =
vertcat(clock2_5.(fft_out).all.ampmean,mean(rmmissing(transpose(clock2_
5.(fft_out).(fn{i}).amp))));
    clock2_5.(fft_out).all.periodmean =
vertcat(clock2_5.(fft_out).all.periodmean,mean(rmmissing(transpose(cloc
k2_5.(fft_out).(fn{i}).period))));
```

```
    clock2_5.(fft_out).all.amp_sd = 
vertcat(clock2_5.(fft_out).all.amp_sd,std(rmmissing(transpose(clock2_5.
(fft_out).(fn{i}).amp))));
    clock2_5.(fft_out).all.period_sd = 
vertcat(clock2_5.(fft_out).all.period_sd,std(rmmissing(transpose(clock2
_5.(fft_out).(fn{i}).period))));

    %Normalized Data collected
    clock2_5.(out).all = 
vertcat(clock2_5.(out).all,(clock2_5.(out).(fn{i})));

    %% Output aggregate for oscillating only
%     red2_5.(fft_out).popavg.amp

end
```

A.6 Clock Fidelity Model

```
%% V1.0: KaiABC simulation with binding correlation and period
estimation
% Simulates clock fidelity based off bulk experimental data &
parameters.
% V1.0: Finalized Version: - Streamlined code

%% Begin Input Parameters %%

%% Input Parameters: Encapsulation (Gamma distribution)

% Default: 0.13 (exp) %Correlation ratio for KaiA/KaiB binding to KaiC
%(monomer ratio)
corr_ABC    = 0.13;

% Default: 0.31 (exp) %Average CV value from experiments
CV_avg      = 0.31;

% KaiA : KaiB : KaiC stiochiometry @ 1X
conc_stoch = [1.2,3.5,3.5];

%List of Concentrations (!! changing this requires manual editing of
code !!)
conc_rel    = [0.5; 0.75; 1.0; 1.5; 2.5];

% Ratio of KaiA:KaiB:KaiC binding during loading
ratio_ABC = [2,1,1];

%% Input Parameters: Clock reaction simulation
sim_osc_all = [];           % Set Output Variable Name

diam = [3,4,6,8,10];        % Choose vesicle diameters (calculations
are performed for each)
radi = diam/2;              % Calculate Radius
n    = 5000;                % # of simulated vesicles (default = 5000)

crit_conc_rel = 0.5;        % Optimal: 0.5 %x critical concentration
(relative) (from bulk) for KaiA & KaiB & KaiC
crit_ratio    = 0.5;        % Optimal: 0.5 %Critical ratio relative
max_ratio     = 3.0;        % Optimal: 3.0 %Max relative ratios
b             = 650;        % Optimal: 650 %KaiB Molecules bound per
µm^2 surface area

title1   = strcat('b = ', num2str(b));
plotfigs = 1;            % Plot simulation fidelity data?
plotexp  = 0;            % Plot experimental data underlay?

vol_um3 = (4/3)*pi*(radi).^3; % Calculate volume of vesicle (µm^3)
vol_L   = vol_um3 * 1e-15;    % Volume in L
SA      = 4*pi*(radi).^2;     % Surface area in µm^2

%Unused input parameters (keep at designated values)
```

```
kaic_cobind = 0;            % KaiC to KaiB cobinding in the membrane
ratio. NOTE: Unused keep at 0
kaib_factor = 1.0;          % Multiple KaiB concentration by factor.
NOTE: Unused keep at 1.0


%% Inital Calculations and Parameter Loading - Based on input
parameters %%


%% Critical Concentration calculation
% Calculates critical concentration in µM
min_kaiA = 1.2*crit_conc_rel;    % KaiA limiting concentration µM
min_kaiB = 3.5*crit_conc_rel;    % KaiB limiting concentration µM
min_kaiC = 3.5*crit_conc_rel;    % KaiC limiting concentration µM

%% Critical Ratio calculation
% Limiting ratios
min_R_kaiAC = crit_ratio*(1.2/3.5); % Limiting KaiA:KaiC ratio
min_R_kaiBC = crit_ratio;           % Limiting KaiB:KaiC ratio

% Maximum ratios
max_R_kaiAC = max_ratio*(1.2/3.5);  % Max KaiA:KaiC ratio: 1.03

%% Other calculations
% Number molecules associated with membrane
N_memKaiB_all = SA*b;
N_memKaiC_all = N_memKaiB_all * kaic_cobind * 6; %Note the *6 here is
because KaiC hexamer unit (6) could bind to one KaiB monomer

%% Period Simulation Setup using period offset lookup tables
%Loads period lookup tables:
load('Period Simulation\Period_lookup_tables.mat')

%Loads experimental period data for comparison:
load('Period Simulation\Exp_periods.mat')

% Loads number of oscilating vesicles by size:
load('Period Simulation\N_oscillating_vesbysize.mat')

%Mean experimental period (from 0.5x to 2.5x)
mean_period = [23.26,22.8,22.8,22.8,22.0];

%% Amplitude Simulation Setup - Based on bulk data and KaiB
concentration
load('Amplitude Simulation\Amp_lookup.mat')

amp_bulk_calcurve = @(x) 0.02102*x + 0.08998; %x is KaiC concentration
% amp_bulk_calcurve = @(x) -0.0046*x.^2 + 0.0576*x + 0.023;

offset = 0.09; %Offset between bulk and mean GUV amplitudes

%% Initalize variables
sim_period_all = [];
sim_period_SD = [];
```

```
sim_osc_all = [];
adj_amp_mean = [];
adj_amp_SD = [];
sim_osc_all = [];


%% Begin Simulation Calculations %%


%% Simulate encapsulated protein concentrations using gamma
distribution

conc_relstring = 'c'+strrep(string(num2str(conc_rel,'%.2f')),'.','_');
%Concentration converted into strings

KaiC1x = conc_stioch(3);
KaiB1x = conc_stioch(2)*1.0;
KaiA1x = conc_stioch(1)*1.0;

% Initatize variables
ABC_mean  = []; C_mean  = []; B_mean  = []; A_mean  = [];
ABC_gam   = []; C_gam   = []; B_gam   = []; A_gam   = [];
ABC_k     = []; C_k     = []; B_k     = []; A_k     = [];
ABC_theta = []; C_theta = []; B_theta = []; A_theta = [];

A_mean_list = [];

% Loop to run all selected concentrations
for i = 1:length(conc_rel)
    % Note: Mean KaiA & KaiB concentrations is reduced because of
binding to KaiC
    % Equation for mean from gamma parameters: mean = k (shape) * theta
(scale)

    %% KaiABC Encapsulation
    ABC_mean(i)  = KaiC1x*conc_rel(i)*corr_ABC; % Mean # of KaiABC
formed
    ABC_k(i)     = 1/CV_avg^2;
    ABC_theta(i)= ABC_mean(i)*CV_avg^2;
    ABC_gam{i}   = gamrnd(ABC_k(i),ABC_theta(i),5000,1);

    %% KaiC Encapsulation
    C_mean(i)    = KaiC1x*conc_rel(i)-(ABC_mean(i)*ratio_ABC(3)); %Mean
reduced due to forming KaiABC (by correlation factor)
    C_k(i)       = 1/CV_avg^2;
    C_theta(i)   = C_mean(i)*CV_avg^2;
    C_gam{i}     = gamrnd(C_k(i),C_theta(i),5000,1);
    C_gam{i}     = C_gam{i} + ABC_gam{i}*ratio_ABC(3);

    %% KaiB Encapsulation
    B_mean(i)    = KaiB1x*conc_rel(i)-(ABC_mean(i)*ratio_ABC(2)); %Mean
reduced due to forming KaiABC (by correlation factor)
    B_k(i)       = 1/CV_avg^2;
    B_theta(i)   = B_mean(i)*CV_avg^2;
    B_gam{i}     = gamrnd(B_k(i),B_theta(i),5000,1);
```

```
    B_gam{i}    = B_gam{i} + ABC_gam{i}*ratio_ABC(2);

    %% KaiA Encapsulation
    A_mean(i)    = KaiA1x*conc_rel(i)-(ABC_mean(i)*ratio_ABC(1)); %Mean
reduced due to forming KaiABC (by correlation factor)
    A_k(i) = 1/CV_avg^2;
    A_theta(i) = A_mean(i)*CV_avg^2;
    A_mean_list(i) = A_mean(i);

    % Check if subtraction reduces mean KaiA below 0
    if A_mean(i) > 0
        A_gam{i} = gamrnd(A_k(i),A_theta(i),5000,1);
        A_gam{i} = A_gam{i} + ABC_gam{i}*ratio_ABC(1);
    else
        A_mean(i)     = 0;
        A_gam{i}      = zeros(5000,1); %If all KaiA is bound to KaiABC
complexes there is no KaiA encapsulation
        limA_mean     = KaiA1x*conc_rel(i);
        % Special KaiABC distribution if KaiA is limited (so no extra
KaiA appears)
        A_gam{i}      = A_gam{i} + ABC_gam{i} * limA_mean/ABC_mean(i);
    end

end

KaiC = table(C_gam{:},'VariableNames',conc_relstring);
KaiB = table(B_gam{:},'VariableNames',conc_relstring);
KaiA = table(A_gam{:},'VariableNames',conc_relstring);

% Validation generated means
C_gam_mean = cellfun(@mean,C_gam);
B_gam_mean = cellfun(@mean,B_gam);
A_gam_mean = cellfun(@mean,A_gam);

%% Simulate Clock Vesicle Fidelity (How many oscillate)

%% Combined encapsulation in vesicles.

for conc = 1:length(conc_rel)
    % Put concentrations together into a simulated vesicle per horz
line
    conc_KaiABC_sim{conc} =
horzcat(KaiA{:,conc},KaiB{:,conc},KaiC{:,conc}); %%

    %% Load data and determine whether sim vesicles oscillate.
    % Note: Column 1 = KaiA Conc., Column 2 = KaiB Conc., Column 3 =
KaiC Conc.(µM)

    i_KaiA{conc} = conc_KaiABC_sim{conc}(:,1);
    i_KaiB{conc} = conc_KaiABC_sim{conc}(:,2);
    i_KaiC{conc} = conc_KaiABC_sim{conc}(:,3);

    %% Remove membrane associated proteins from free protein
concentration
    % Number of molecules total
```

```
    N_KaiB{conc} = i_KaiB{conc} * 10^(-6) * vol_L * (6.022*10^23);
    N_KaiC{conc} = i_KaiC{conc} * 10^(-6) * vol_L * (6.022*10^23);

    % Free Protein Concentration in Vesicles(uM)(aka: not associated
with membrane)

    KaiA_free{conc} = i_KaiA{conc};
    KaiB_free{conc} = i_KaiB{conc} .* (1 - (N_memKaiB_all ./
N_KaiB{conc}));
    KaiC_free{conc} = i_KaiC{conc}  .* (1 - (N_memKaiC_all ./
N_KaiC{conc}));

    %% Check and replace negative values

    KaiB_free{conc}(KaiB_free{conc}<0) = 0;

    %% Calculate KaiA:KaiC and KaiB:KaiC ratios

    KaiAC_ratio{conc} = (KaiA_free{conc} ./ KaiC_free{conc});
    KaiBC_ratio{conc} = (KaiB_free{conc} ./ KaiC_free{conc});

    %% Check if conditions are met, and determining oscillating (osc)
vesicles

    checkC_kaiA{conc} = KaiA_free{conc} >= min_kaiA;
    checkC_kaiB{conc} = KaiB_free{conc} >= min_kaiB;
    checkC_kaiC{conc} = KaiC_free{conc}   >= min_kaiC;
    checkR_kaiAC{conc} = KaiAC_ratio{conc} >= min_R_kaiAC;
    checkR_kaiBC{conc} = KaiBC_ratio{conc} >= min_R_kaiBC;
    checkR_maxkaiAC{conc} = KaiAC_ratio{conc} <= max_R_kaiAC;
    osc{conc} = checkC_kaiA{conc} & checkC_kaiB{conc} &
checkC_kaiC{conc} & checkR_kaiAC{conc} & checkR_kaiBC{conc} &
checkR_maxkaiAC{conc};


    %% Period Simulation using period offset lookup tables

    period_conc{conc} =
interp1(period_KaiAC.ratio,period_KaiAC.p_offset,KaiAC_ratio{conc},'lin
ear')...
                    +
interp1(period_KaiBC.ratio,period_KaiBC.p_offset,KaiBC_ratio{conc},
'linear')+ mean_period(conc); %last number is mean period

    %Remove all periods for non-oscillating vesicles and replace with a
NaN
    % Columns = size, Rows = individual vesicles
    period_conc{conc}(osc{conc} == 0) = NaN;

    % Note that (rows = concentration , columns = size)
    period_mean{conc} = mean(period_conc{conc},'omitnan');
    period_SD{conc} =   std(period_conc{conc},'omitnan');
    sim_period_all = vertcat(sim_period_all, period_mean{conc});
    sim_period_SD = vertcat(sim_period_SD, period_SD{conc});
```

```
    %% Amplitude Simulation - Based on bulk data and KaiB concentration

    % Note that (rows = concentration , columns = size)
    KaiC_free_osc{conc} = KaiC_free{conc};
    KaiC_free_osc{conc}(osc{conc}==0) = NaN;

    inital_amp{conc,1} = amp_bulk_calcurve(KaiC_free_osc{conc})-offset;
    amp_nonan{conc,1} = inital_amp{conc}(~isnan(inital_amp{conc}));
    amp_norm{conc,1} = amp_nonan{conc}/mean(amp_nonan{conc});

    %% Nakajima data matrix
    % These amp_matrix values are loaded in amplitude simulation setup

    adj_amp{conc} = inital_amp{conc} .*
interp2(amp_matrix_KaiAC,amp_matrix_KaiBC,amp_matrix,KaiAC_ratio{conc},
KaiBC_ratio{conc},'linear');

    adj_amp_nonan{conc,1} = adj_amp{conc}(~isnan(adj_amp{conc}));

    adj_amp_norm{conc,1} =
adj_amp_nonan{conc}/mean(adj_amp_nonan{conc});

    adj_amp_mean = vertcat(adj_amp_mean,
mean(adj_amp{conc},'omitnan'));

    adj_amp_SD = vertcat(adj_amp_SD, std(adj_amp{conc},'omitnan'));

    %% Fraction oscillating 2
    % Fraction oscillating (rows = concentration , columns = size)
    sim_osc_all = vertcat(sim_osc_all,sum(osc{conc})/n);

end

%% Experimental Amplitude
% Note that (rows = concentration , columns = size)
               %3 um    4 um    6 um    8 um    10 um
exp_amp_mean = [NaN     NaN     NaN     NaN     NaN;    %0.5x
                0.11    0.09    0.08    0.08    0.08;   %0.75x
                0.08    0.07    0.07    0.08    0.08;   %1.0x
                0.12    0.12    0.13    0.15    0.14;   %1.5x
                0.16    0.15    0.15    0.15    0.15];  %2.5x


%% Figure Plotting

% Concentration values
sim_conc = conc_rel; %[0.5;0.75;1.0;1.5;2.5] %;2.0  %Relative values
(0.5x, 0.75x, etc...)
sim_size = diam;

% Rows = Concentration, Columns = Size
%          3 um     4 um    6 um    8 um    10 um
exp_all = [0.03     0.04    0.01    0.03    0.00        % 0.5x
           0.10     0.25    0.38    0.48    0.50        % 0.75x
```

```
                0.31      0.55     0.63     0.75     0.75         % 1.0x
            0.48      0.73     0.86     0.90     0.88         % 1.5x
            0.71      0.86     0.95     0.96     0.96];       % 2.5x


% Plot Figure with simulation results
if plotfigs == 1
    h1 = figure; % set(h1,'DefaultAxesColorOrder',parul(6))
    if plotexp == 1
        hold on; plot(sim_conc,exp_all,'^--
','LineWidth',3,'MarkerSize',6)

colororder(flip(['#00634F';'#178D97';'#64A7CE';'#A1BAD9';'#D0D1E6']));

%         hold on;
plot(sim_conc_cell,exp_cell,'^k','LineWidth',3,'MarkerSize',6)
%         set(gca,'ColorOrderIndex',1)
    end
      hold on; plot(sim_conc, sim_osc_all,'o-
      ','LineWidth',3,'MarkerSize',10)
%     set(gca,'ColorOrderIndex',1)

    colororder(flip(['#00634F';'#178D97';'#64A7CE';'#A1BAD9';'#D0D1E6';'
    #00634F';'#178D97';'#64A7CE';'#A1BAD9';'#D0D1E6']));
%     hold on;
plot(sim_conc,sim_osc_all,'o','LineWidth',3,'MarkerSize',10)
    set(gca,'fontsize',18,'LineWidth',3); grid off; box on; axis square
    xticks([0.5:0.5:2.5])
    %xticklabels({0.5, 1.0, 1.5, 2.0, 2.5})
    % legend('Exp: 10 µm','Exp: 8 µm','Exp: 6 µm','Exp: 4 µm','Exp: 3
µm'...
    %     ,'Model: 10 µm', 'Model: 8 µm', 'Model: 6 µm', 'Model: 4 µm',
'Model: 3 µm','Location','northwest','FontSize',8)
    % legend('Model: 10 µm', 'Model: 8 µm', 'Model: 6 µm', 'Model: 4
µm', 'Model: 3 µm','Model: 2 µm','Location','northwest','FontSize',12)
    title(strcat('C:',num2str(crit_conc_rel),',
    R:',num2str(crit_ratio),', b=', num2str(b),', Corr-
    BC:',num2str(corr_ABC),'/AC:',num2str(corr_ABC,2)));
    xlim([0.4 2.6])
    set(gca,'XMinorTick','on','YMinorTick','on')
    hA = gca; hA.XAxis.MinorTickValues = 0:0.25:3;
    % title(title1)
    %color_grays =
[[37,37,37],[99,99,99],[150,150,150],[189,189,189],[217,217,217]];
end
```